Journal of Geophysical Research: Planets

RESEARCH ARTICLE
10.1029/2018JE005774

Key Points:
- During the Mars Exploration Rover *Spirit* mission, the Microscopic Imager returned 5,923 full-frame images
- These images have guided interpretations of the geologic history of Gusev crater on Mars
- A table summarizing the MI images chronologically is appended, including target/feature names and sequence identifiers for Pancam images that provide context

Supporting Information:
- Supporting Information S1
- Movie S1

Correspondence to:
K. E. Herkenhoff,
kherkenhoff@usgs.gov

Citation:
Herkenhoff, K. E., Squyres, S. W., Arvidson, R. E., Cole, S. B., Sullivan, R., Yingst, A., et al. (2019). Overview of *Spirit* microscopic imager results. *Journal of Geophysical Research: Planets*, *124*, 528–584. https://doi.org/10.1029/2018JE005774

Received 27 JUL 2018
Accepted 20 NOV 2018
Accepted article online 24 NOV 2018
Published online 21 FEB 2019

Author Contributions:
Conceptualization: Ken E. Herkenhoff, Steve W. Squyres, Raymond E. Arvidson, Ella M. Lee
Data curation: Ken E. Herkenhoff, Janet Richie, Bob Sucharski, Bonnie Redding, Annette Sunda
Formal analysis: Ken E. Herkenhoff, Raymond E. Arvidson, Shoshanna B. Cole, Rob Sullivan, Aileen Yingst, Nathalie Cabrol, Alicia Vaughan
Funding acquisition: Ken E. Herkenhoff, Steve W. Squyres
Investigation: Ken E. Herkenhoff
Methodology: Ken E. Herkenhoff, Ella M. Lee, Janet Richie, Bob Sucharski, Randy Kirk, Bonnie Redding
Resources: Ken E. Herkenhoff
(continued)

Overview of *Spirit* Microscopic Imager Results

Ken E. Herkenhoff[1], Steve W. Squyres[2], Raymond E. Arvidson[3], Shoshanna B. Cole[2], Rob Sullivan[4], Aileen Yingst[5], Nathalie Cabrol[6], Ella M. Lee[1,7], Janet Richie[1], Bob Sucharski[1,7], James F. Bell III[8], Fred Calef[9], Mary Chapman[1,7], Lauren Edgar[1], Brenda Franklin[9,7], Paul Geissler[1], Joel Hurowitz[10], Elsa Jensen[11], Jeffrey R. Johnson[12], Randy Kirk[1,7], Peter Lanagan[13], Craig Leff[9], Justin Maki[9], Kevin Mullins[1,7], Bonnie Redding[1], Melissa Rice[14], Michael Sims[15], Larry Soderblom[1,7], Nicole Spanovich[9], Richard Springer[9], Annette Sunda[1], and Alicia Vaughan[1]

[1]Astrogeology Science Center, U. S. Geological Survey, Flagstaff, AZ, USA, [2]Department of Astronomy, Cornell University, Ithaca, NY, USA, [3]Department of Earth and Planetary Sciences, Washington University in Saint Louis, St. Louis, MO, USA, [4]CCAPS, Cornell University, Ithaca, NY, USA, [5]Planetary Science Institute, Tucson, AZ, USA, [6]NASA Ames Research Center/SETI Institute, Moffett Field, CA, USA, [7]Retired, [8]Department of Geological Sciences, Arizona State University, Tempe, AZ, USA, [9]Jet Propulsion Laboratory, California Institute of Technology, Pasadena, CA, USA, [10]Department of Geosciences, State University of New York, Stony Brook, NY, USA, [11]Malin Space Science Systems, San Diego, CA, USA, [12]The Johns Hopkins University Applied Physics Laboratory, Laurel, MD, USA, [13]Lunar and Planetary Laboratory, University of Arizona, Tucson, AZ, USA, [14]Geology Department, Western Washington University, Bellingham, WA, USA, [15]Mars Institute, Moffett Field, CA, USA

Abstract This paper provides an overview of Mars Exploration Rover *Spirit* Microscopic Imager (MI) operations and the calibration, processing, and analysis of MI data. The focus of this overview is on the last five Earth years (2005–2010) of *Spirit*'s mission in Gusev crater, supplementing the previous overview of the first 450 sols of the *Spirit* MI investigation. Updates to radiometric calibration using in-flight data and improvements in high-level processing are summarized. Released data products are described, and a table of MI observations, including target/feature names and associated data sets, is appended. The MI observed natural and disturbed exposures of rocks and soils as well as magnets and other rover hardware. These hand-lens-scale observations have provided key constraints on interpretations of the formation and geologic history of features, rocks, and soils examined by *Spirit*. MI images complement observations by other *Spirit* instruments, and together show that impact and volcanic processes have dominated the origin and evolution of the rocks in Gusev crater, with aqueous activity indicated by the presence of silica-rich rocks and sulfate-rich soils. The textures of some of the silica-rich rocks are similar to terrestrial hot spring deposits, and observations of subsurface cemented layers indicate recent aqueous mobilization of sulfates in places. Wind action has recently modified soils and abraded many of the rocks imaged by the MI, as observed at other Mars landing sites.

Plain Language Summary The Microscopic Imager (MI) on NASA's *Spirit* rover returned the highest-resolution images of the Martian surface available at the time of the 2004–2010 mission. Designed to survive 90 Mars days (sols) and search for evidence of water in the past, *Spirit* returned data for 2210 sols, far exceeding all expectations. This paper summarizes the scientific insights gleaned from the thousands of MI images acquired during the last 5 years of the mission, supplementing the summary of the first 450 sols of the *Spirit* MI investigation published previously (Herkenhoff et al., 2006). Along with data from the other instruments on *Spirit*, MI images guided the scientific interpretation of the geologic history of the rocks and soils observed in Gusev crater on Mars. We conclude that the geologic history of the area explored by *Spirit* has been dominated by impacts and volcanism, and that water, perhaps very hot water, was involved in the evolution of some of the rocks and soils. More recently, winds have moved soil particles and abraded rocks, as observed elsewhere on Mars. These results have improved our understanding of Mars' history and informed planning of future missions to Mars.

1. Introduction

The Microscopic Imager (MI) is part of the Athena science payload on the Mars Exploration Rovers (MERs) *Spirit* and *Opportunity* (Crisp et al., 2003; Squyres et al., 2003). Designed to provide views like those obtained using a geologist's hand lens, it is a fixed-focus Charged-Coupled Device (CCD) camera mounted on the rover's Instrument Deployment Device (IDD) (Herkenhoff et al., 2003). The other instruments mounted on

Supervision: Ken E. Herkenhoff
Validation: Ken E. Herkenhoff, Janet Richie, Bob Sucharski, Bonnie Redding, Annette Sunda
Writing - original draft: Ken E. Herkenhoff, Shoshanna B. Cole, Rob Sullivan, Aileen Yingst
Writing – review & editing: Ken E. Herkenhoff, Janet Richie

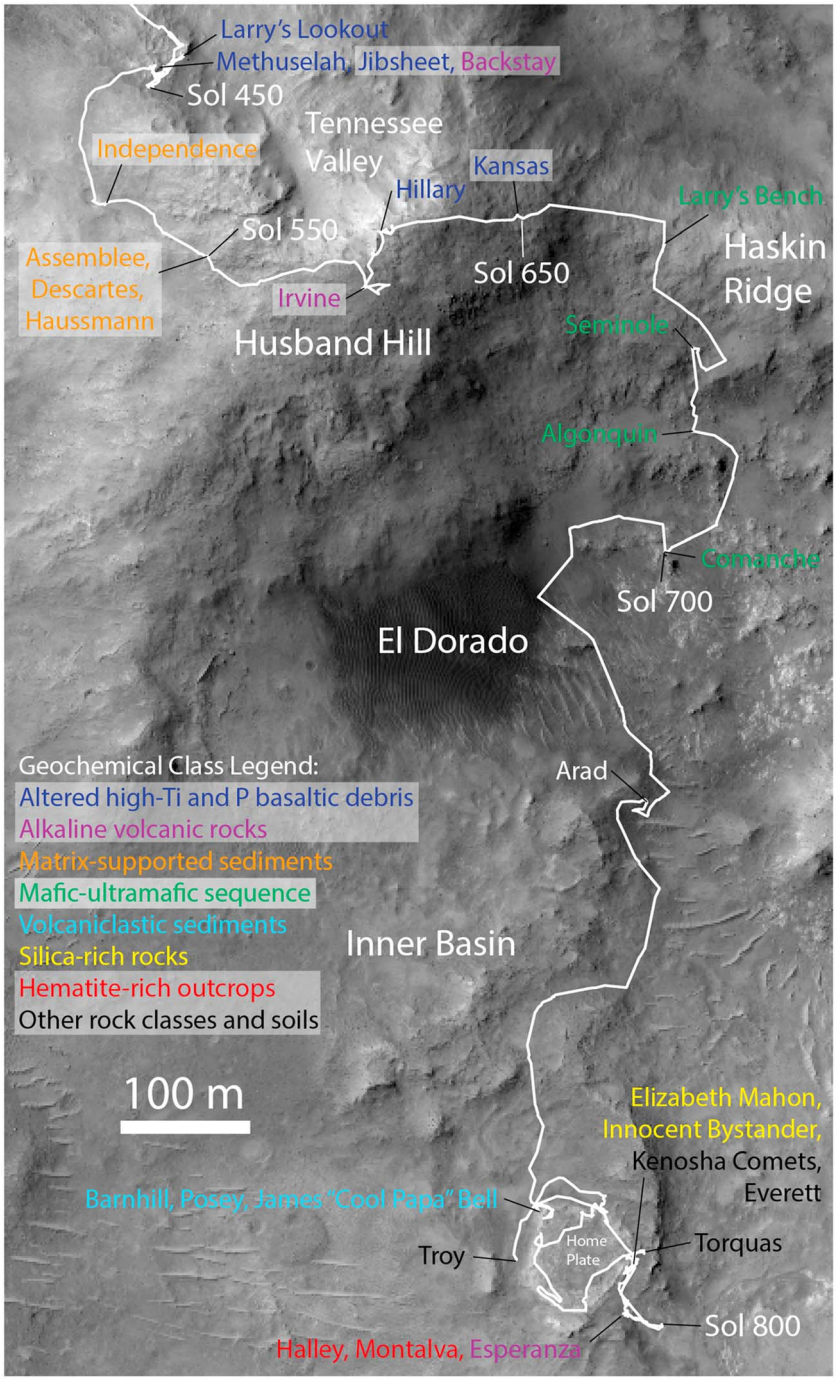

Figure 1. *Spirit* traverses and key targets from Husband Hill into the Inner Basin during last 5 years of mission, overlain on Mars Reconnaissance Orbiter High-Resolution Imaging Science Experiment image PSP_001513_1655, acquired on 22 November 2006 (*Spirit* Sol 1026) with illumination from upper left. Feature names are color coded according to geochemical classification (see legend).

the IDD are the Alpha Particle X-Ray Spectrometer (APXS; Gellert et al., 2006), the Mössbauer Spectrometer (MB; Klingelhöfer et al., 2003), and the Rock Abrasion Tool (RAT; Gorevan et al., 2003). The MI's spectral bandpass is similar to that of the human eye (400 to 700 nm), and in-focus images have a scale of 31 μm/pixel over a 32-mm square field of view. After *Spirit* landed in Gusev crater in January 2004 (Squyres et al., 2004), the MI provided the highest-resolution views of the Martian surface available at the time, resolving objects as small as 0.1 mm across (Herkenhoff, Kirk, et al., 2004).

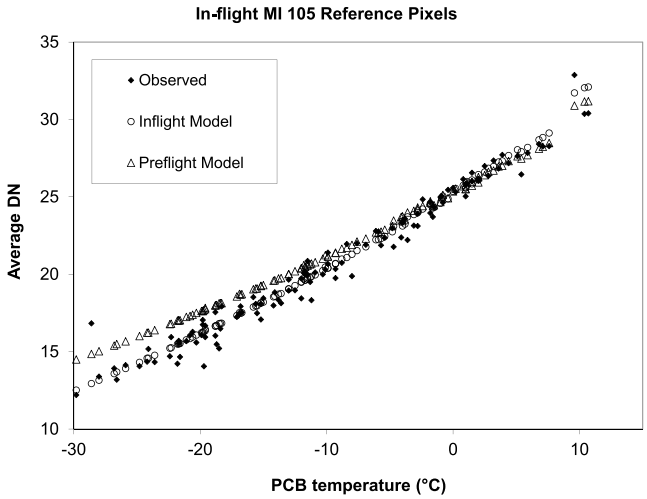

Figure 2. Average of observed reference pixel data in samples 4–13, lines 412–612 compared with models based on preflight and in-flight calibration data. PCB is printed circuit board in Microscopic Imager electronics box.

An overview of the first 450 sols (Martian days) of *Spirit* MI results was published previously (Herkenhoff et al., 2006), so this paper focuses on the reduction and analysis of MI data acquired during the last 5 years of *Spirit*'s mission, 2005–2010. During the beginning of this period, *Spirit* finished climbing to the summit of *Husband Hill* and then descended via *Haskin Ridge* into the *Inner Basin*, arriving at *Home Plate* on Sol 746 (Figure 1, Arvidson et al., 2008). *Spirit*'s right front wheel drive actuator was declared inoperative on Sol 787, and the rover spent the rest of her mission in the vicinity of Home Plate (Arvidson et al., 2010). Rover mobility was more limited during this phase of the mission, and on Sol 1871 *Spirit* became embedded in loose soil at *Troy*. Attempts to extricate the rover from the sands of Troy were partly successful, but it was not possible to tilt the rover solar panels toward the Sun before *Spirit*'s fourth winter, and ultimately insufficient power was available to continue operations. The last transmission from *Spirit* was received on 22 March 2010 (Sol 2210). During the *Spirit* mission, the rover returned 5,923 full-frame MI images.

A description of MI tactical operations, focusing on methods used during *Spirit*'s extended mission, is followed below by a summary of in-flight calibration results. We then describe MI data processing techniques, with an emphasis on advances during the extended mission. MI observations of rocks and soils are discussed separately and organized according to previously published classification schemes. Finally, MI images of rover hardware are described and MI contributions to the interpretation of the geologic history of Gusev crater are summarized. Key information regarding *Spirit* MI images is listed in Appendix A, where *features* may be outcrops, individual rocks, soil patches, or the rover, and *targets* are specific locations where the MI and other arm instruments were placed.

2. MI Tactical Operations

The methods used to operate the MI during the first 450 sols of *Spirit*'s mission were described by Herkenhoff et al. (2006), including tactical processing and analysis of data received from the rover (downlink; Alexander et al., 2006), and preparation of new sequences of commands (uplink). This section provides an updated summary of the methods and tools used to operate the MI over the last 5 years of the *Spirit* mission.

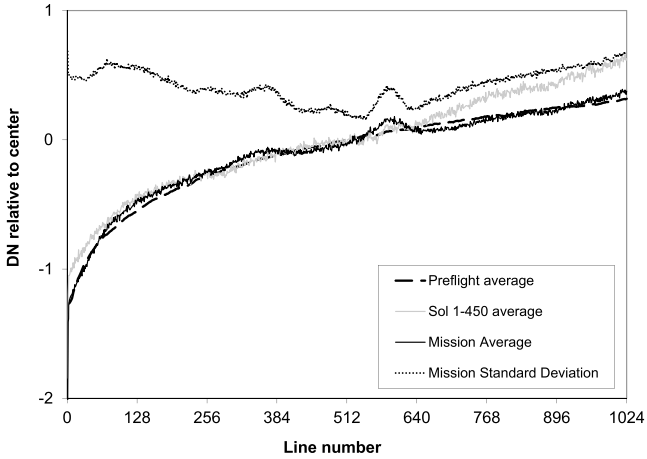

Figure 3. Normalized mean reference pixel values in samples 4–13: Preflight average (dashed), Sol 1–450 average (gray), and entire mission average (black). Standard deviation of reference pixels about mission average is shown as dotted line (maximum 0.7 DN).

2.1. Uplink

An MI/engineering camera Payload Uplink Lead (PUL) was scheduled each planning day of the *Spirit* mission. The PUL's overall responsibility was to generate and validate MI and engineering camera (Navcam and Hazcam; Maki et al., 2003) command sequences for uplink to the rover (Herkenhoff et al., 2006). The PUL tasks were often performed in person at the Caltech Jet Propulsion Laboratory (JPL, the NASA center managing the MER project) but sometimes remotely using teleconferencing and internet connections. Lessons learned in the remote operation of the *Spirit* MI and engineering cameras may be useful to current and future rover mission operations: It can be difficult to learn PUL tasks remotely, so initial experience while directly embedded with the spacecraft mission operations team is needed. Shadowing a fully trained PUL at JPL is essential to learning these tasks. Working with the tactical team in person allows nonverbal cues to be communicated and used to better allow tone of voice and other types of communication to be recognized and properly understood remotely. As operations continue, each PUL should be scheduled to work at least one tactical shift per month to maintain familiarity with the uplink procedure and operation tasks. Better yet, PULs should

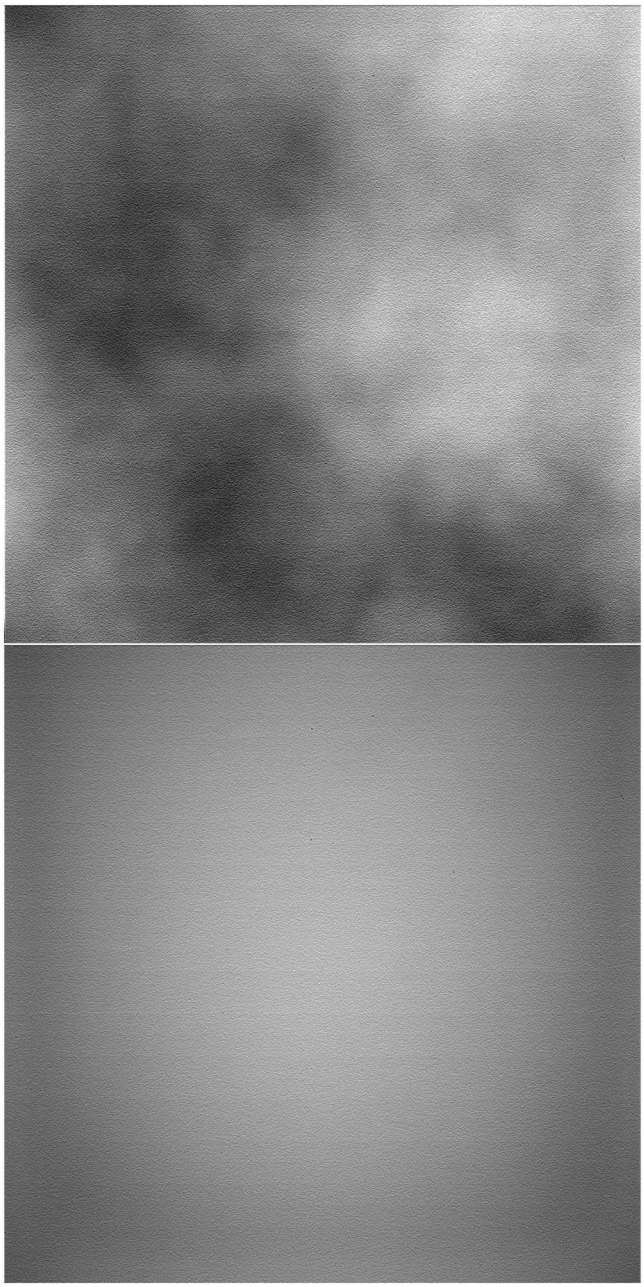

Figure 4. Microscopic Imager flat fields. (top) Average of sky flats 2M310656087 and 2M310656419 acquired on Sol 2076. (bottom) Processed flat field acquired during preflight calibration.

be scheduled for up to four tactical shifts in a row to take advantage of their familiarity with recent mission events when planning new activities.

Because the PULs were responsible for commanding seven of *Spirit*'s cameras (Herkenhoff et al., 2006), they often had a heavy operations workload, and during the early days of the mission it was sometimes challenging for the PUL to deliver command sequences on time. In response to this need, a software system called AutoPUL was developed that automated many of the steps in the PUL procedure. AutoPUL has since been used on most uplink days, resulting in a significant simplification of the PUL job. AutoPUL performs the following tasks: parse the output of the science planning meeting, turn those science directions into the appropriate uplink commands, eliminate redundancies and introduce additional commands for a variety of circumstances, present a command list to the PUL for review and approval, move command sequences to proper locations for uplink to the spacecraft, move commands to repositories for archival record keeping, generate various reports of the commands and processing, clean up temporary files as desired, and create reports on the MER internal website for documenting activities, including detailed parsing of all commands and summaries of downlink priority and data volume for each image to be acquired. This software was used until the end of the *Spirit* mission and continues to be used for *Opportunity* uplink operations.

2.2. Downlink

Onboard and ground processing of MI images was described by Herkenhoff et al. (2006). Early in the mission, experiments using various types of the onboard wavelet-based ICER compression software (Kiely & Klimesh, 2003) were analyzed and used to select optimal compression parameters for MI images. Various levels of ICER lossy *MINLOSS* (quality 1–7) compression were tested and compared with losslessly compressed MI images. This type of quality compression is ideally suited to MI images, which typically include both well-focused and poorly focused areas. The ICER quality compression preserves sharp features in well-focused parts of the image, while applying more compression to poorly focused areas. Raw MI images are usually broken into 32 segments, each of which is separately compressed to the same quality level. This approach results in variable compression rates among the segments, depending on the amount of information contained in each. Therefore, the image data are compressed to levels that preserve fine detail while minimizing downlink data volume.

3. In-Flight Calibration

The results of MI calibration activities before the MER launches were summarized by Herkenhoff et al. (2003); detailed results are available in the MI calibration report (Herkenhoff, Kirk, et al., 2004). The results of in-flight calibration through Sol 450 were summarized by Herkenhoff et al. (2006). The collection and application of in-flight MI calibration data after Sol 450 are described in this section.

No changes in the geometric optical performance of the MI were evident during the *Spirit* mission. MI images of the Compositional Calibration Target (Herkenhoff et al., 2003) were acquired on Sol 615 but do not include enough of the black dots on the edge of the target to be useful in verifying MI geometric calibration. Therefore, there are no changes to the geometric calibration results reported by Herkenhoff, Kirk, et al. (2004).

Radiometric calibration of MI images involves corrections for dark current, offset/bias (recorded in the reference pixels), flat field sensitivity variations, and conversion to radiance or I/F (the ratio of the observed

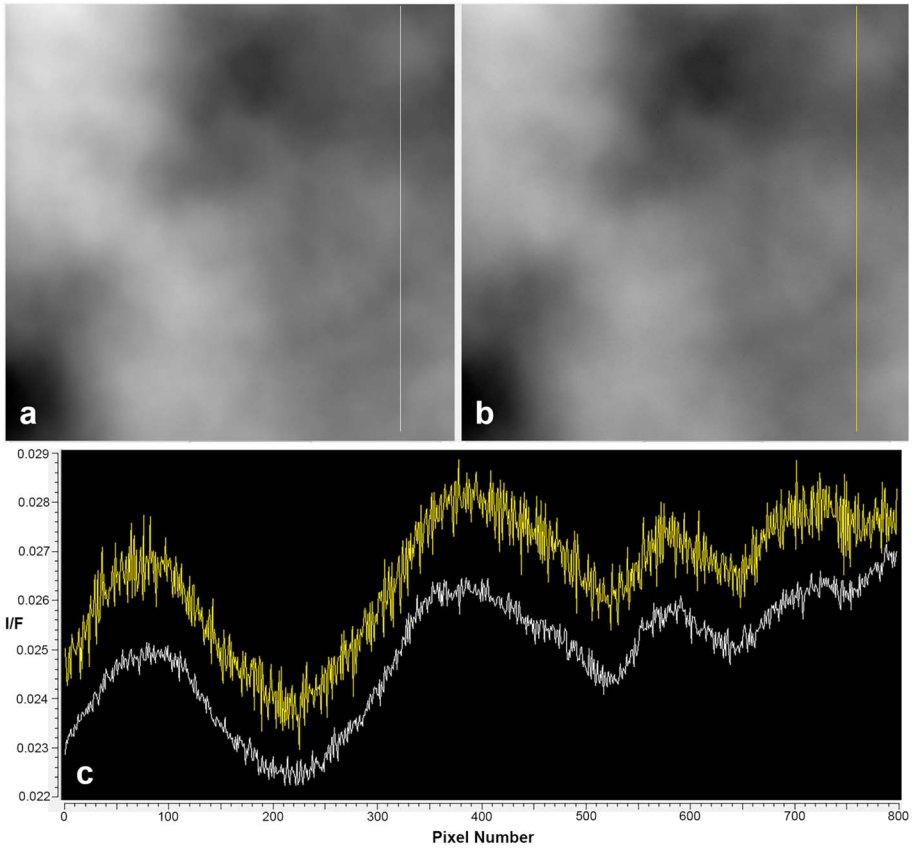

Figure 5. Comparison of flat-field correction of Microscopic Imager image taken with dust cover closed on Sol 1280, soon after the 2007 global dust storm that contaminated the MI optics. This low-contrast image allows differences in flat-field calibration to be easily characterized. (a) Image calibrated using flat field derived from Sol 2076 sky flats. (b) Image calibrated using preflight flat. (c) Plot of pixel values along profiles shown in images above. Colors correspond to colors of profiles on images.

irradiance to the irradiance expected from the solar illumination of a Lambert surface; Danielson et al., 1981). Updates to MI radiometric calibration, including reference pixel modeling, flat-field correction, and overall accuracy, are summarized below. It is not possible to acquire useful MI dark current data on the surface of Mars because the camera has no shutter and nighttime temperatures are very low, so no updates to dark current calibration have been made since Herkenhoff et al. (2006): Errors in *Spirit* MI dark current subtraction typically contribute less than 1 DN to both relative (pixel-to-pixel) and absolute radiometric calibration uncertainty within the calibrated operating temperature range of −55° to +5 °C.

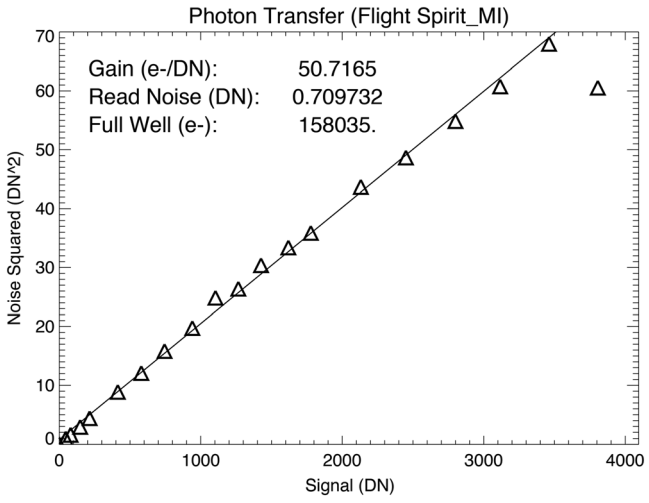

Figure 6. Sol 921 Microscopic Imager photon transfer data (triangles) and fits for gain, read noise, and full well.

3.1. Reference Pixels

The serial register on the MI focal plane assembly includes 16 extra pixels on each end that are shielded from light, known as *reference pixels*, to record the camera bias or offset for each image line (Herkenhoff et al., 2006). The offset can be set by command to ensure that the dynamic range of the CCD analog output falls within the range of the analog-to-digital converter, specifically so that low values are not clipped at zero DN. Reference pixel data were not returned with every MI image, so preflight reference pixel data were modeled and used to correct for offset in-flight images for which reference pixels were not returned. The average

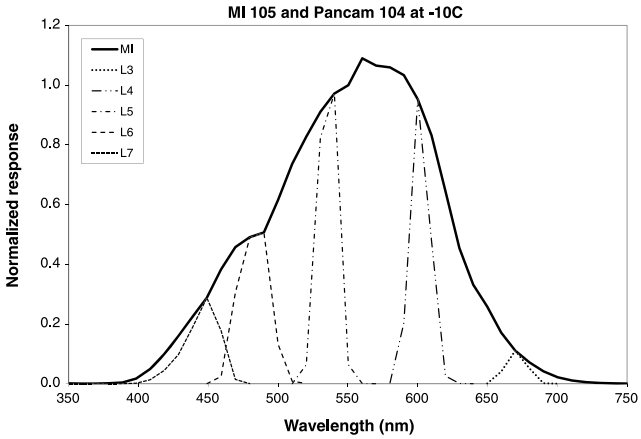

Figure 7. Normalized spectral response of *Spirit* Microscopic Imager (serial no. 105) and left Pancam (serial no. 104), based on preflight calibration data acquired at −10 °C.

reference pixel data acquired by the *Spirit* MI after landing are compared with the model developed using preflight data in Figure 2. As noted by Herkenhoff et al. (2006), the in-flight offset data are typically lower than the model based on preflight data. Similar differences were noted in *Opportunity* MI reference pixel data (Herkenhoff, Grotzinger, et al., 2008). Therefore, we have modeled all the reference pixel data acquired on Mars and improved the fit to this equation, where parameters are defined in Herkenhoff, Kirk, et al. (2004):

$$\begin{aligned}\text{REFPIXAVG} = {} & (\text{VOFFa} - \text{Video\_offset}) * \text{VOFFb} \\ & + (\text{PCBTa} + \text{PDBTb} * \text{Exposure\_time}) * e^{(\text{PCBTc} \times \text{PCB\_temperature})} \\ & + (\text{CCDTa} + \text{CCDTb} * \text{Exposure\_time}) * e^{(\text{CCDTc} \times \text{CCD\_temperature})}\end{aligned} \quad (1)$$

Specifically, the reference pixel model coefficients reported by Herkenhoff, Kirk, et al., (2004, Table 3.2.1a) were modified as follows: VOFFa = 4058, PCBTa = 41, and PCBTc = 0.0122. The standard deviation between the data and the preflight model is 1.24 DN and is reduced to 0.76 DN by the new model. Therefore, errors in correction of offset using this new model contribute less than 1 DN to the absolute radiometric calibration uncertainty.

The above analysis of the average offset for full MI frames ignores the variation in reference pixels with line number, which changed during flight relative to that observed during preflight testing (Herkenhoff et al., 2006). To characterize these changes, samples 4–13 of each line of all in-flight reference pixels were averaged and compared to corresponding preflight reference pixel averages. As shown in Figure 3, the average variation of all the reference pixels returned during the entire *Spirit* mission compares more favorably to the preflight average than the average of the reference pixels returned during the first 450 sols of the mission (Herkenhoff et al., 2006), so that line-dependent errors in offset correction are insignificant compared to other sources of error. The standard deviation of all reference pixels about the mean is less than 0.8 DN for every line, and the maximum deviation is 2 DN. Therefore, the RMS calibration error for MI images acquired within the calibrated temperature range and returned without simultaneous reference pixels, including dark current and offset errors described above, is less than 1.4 DN.

3.2. Sky Flats

A common technique for measuring variations in camera/telescope response across their field of view (FOV) is to acquire images of the sky above terrestrial observatories, assuming that the sky brightness is uniform across the FOV. Similarly, camera systems on Mars can be calibrated for *flat-field* response by imaging the Martian sky, and several MI *sky flats* were acquired during the *Spirit* mission (see Appendix A). However, this method is complicated for wide-angle cameras such as the MI because the assumption that the Martian sky brightness is uniform across the FOV is typically not valid. Because processing of MI images of the sky acquired early in the mission to correct for variations in sky brightness using simultaneous Navcam sky images did not appear to completely remove the gradient in sky brightness (Herkenhoff et al., 2006), a new technique for acquiring MI sky flats was used later in the mission. As before, the MI was pointed away from the Sun to avoid direct illumination of the MI optics, and nearly simultaneous Navcam images were acquired of the same patch of sky. The new approach included a pair of MI images, separated by a 180-degree rotation of the camera about its boresight to allow the gradient in sky brightness to be removed by averaging the images. The sky flats acquired in this way on Sol 2076 are the only ones that have proven useful in measuring the in-flight response of the MI. These images were corrected for dark current and averaged to remove the sky brightness gradient. While this technique does not account for nonlinear variations in sky brightness, modeling of sky radiance indicates that such deviations from a simple gradient in sky brightness are minimal in the direction that the MI sky flats were taken (~40° above the horizon, azimuth opposite the Sun; M. Lemmon, personal communication, 2004). The Navcam sky images are consistent with this model prediction and show no evidence for clouds in the FOV, but dust on the Navcam optical window lends some uncertainty to these conclusions.

Table 1
Sol 475 Pancam Sky Spectral Radiance ($W/m^2/sr/nm$), Weighted by Microscopic Imager Spectral Response

Pancam				MI	Weighted
Filter	Wavelength	Radiance		Weight	Radiance
L7	432	0.007		0.136	0.0010
L6	482	0.011		0.241	0.0026
L5	535	0.013		0.316	0.0041
L4	601	0.018		0.273	0.0050
L3	673	0.016		0.034	0.0005
			Sums:	1	0.0133
			MI Radiance:		0.0110
			Difference:		−17.0%

The averaged images were normalized to the average of the central 100 × 100 pixels. The pattern of sensitivity variations derived in this way from the Sol 2076 sky flats is very different from the pattern observed before launch (Figure 4), as expected because the Sol 2076 sky flats were acquired after the 2007 dust storm (Sullivan et al., 2008). MI images pointed at the horizon on Sol 1290 (after the major dust storm) with the dust cover opened and closed show that both the dust cover and the window protecting the MI optics had been contaminated by dust. By design, the MI dust cover includes a labyrinth to allow gas to escape from between the dust cover and the optical window during launch, but it was not expected to allow Martian dust into the space between the dust cover and the optics. Apparently, strong winds carried dust through the labyrinth onto the optical window.

The normalized average of these sky flats was used to correct MI images taken after the 2007 global dust storm and evaluate the quality of the flat-field correction. As shown in Figure 5, pixel-to-pixel variations are significantly reduced by applying the Sol 2076 flat-field data. The standard deviation of over 1000 pixels in a relatively uniform region of these processed images is 1.3% using the preflight flat data and 0.7% using the Sol 2076 data. Therefore, we have used these data to reprocess all *Spirit* MI data acquired after the 2007 dust storm (starting with Sol 1277). This reprocessing made use of the new reference pixel model described above, which has not been applied to prestorm data because the correction is small.

Because other MI sky flats were not useful in measuring the flat-field response, changes in response could not be measured after the 2007 dust storm, and it is impossible to determine the accuracy of the flat-field correction using the Sol 2076 sky flat data. It is likely that the distribution and thickness of dust on the MI optical window changed during the mission, especially after the dust storm that caused major dust contamination. The standard deviation about the mean of all the pixels in the processed Sol 2076 sky flat data (top of Figure 5) provides an estimate of the accuracy of the flat-field correction: 7.5%. This value includes low-frequency variations in response due to dust contamination as well as pixel-to-pixel variations, so it is likely a conservative estimate of the relative radiometric calibration accuracy. Profiles across the processed Sol 2076 sky flat data show pixel-to-pixel scatter of a few percent, so we estimate that the accuracy of flat-field correction of postcontamination MI images is about 5%. Images acquired before the 2007 dust storm, however, can be calibrated to better than 1% precision, as reported previously (Herkenhoff et al., 2006).

3.3. Photon Transfer

Sets of subframed photon transfer images were acquired on Sols 876, 915, and 921 to determine whether the in-flight performance of the MI is consistent with preflight measurements of CCD linearity, gain, read noise, and full well (maximum response). On Sol 921 the MI was explicitly pointed toward a patch of sky as part of an effort to reduce nonuniformities and changes in scene brightness over the course of the 6.2-min image

Table 2
Summary of MI Data Products

Product name	Type	Location	Changes since 2006
Raw image	EDR	Planetary Data System	None
Decompanded image	EDR	Planetary Data System	None
Calibrated DN	RDR	Planetary Data System	Reprocessed
Calibrated I/F	RDR	Planetary Data System	Reprocessed
Focal section merge	Special	Analyst's Notebook	Added HF products
Focal anaglyph	Special	Analyst's Notebook	None
Cover open/closed color composite	Special	USGS website	None
MI/Pancam color merge	Special	Cornell, USGS websites	None
MI mosaic	Special	USGS website	None
Digital elevation model	Special	USGS website	None

Note. MI = Microscopic Imager; EDR = Experiment Data Record; RDR = Reduced Data Record; HF = Helicon Focus; USGS = United States Geological Survey.

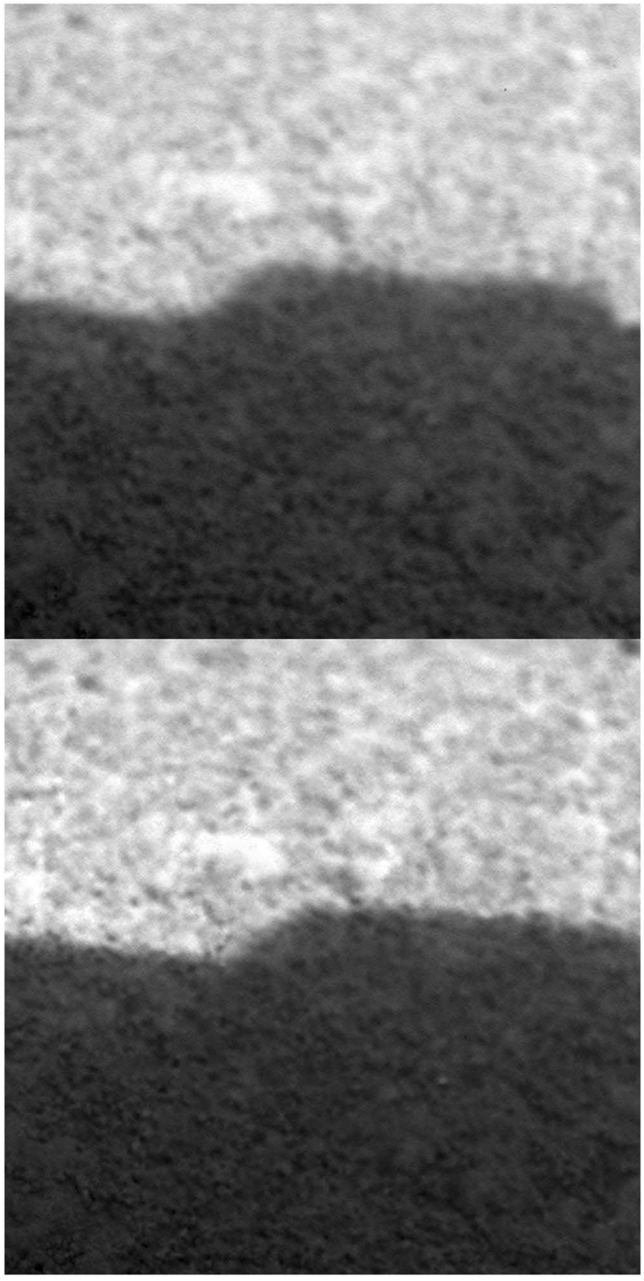

Figure 8. The 605 × 605-pixel portions of focal section merges of Microscopic Imager images acquired on Sol 703 when target *Fins* on feature *Comanche Spur* was partly shadowed. (top) Product created using IDL software. (bottom) Product created using HF software.

acquisition sequence. The results of the Sol 921 analysis (Figure 6) are slightly different from the preflight results: Gain = 47.9 ± 1.6 electrons/DN, Read Noise = 0.67 ± 0.08 DN, and Full Well = 169,304 ± 6,099 electrons within the operating temperature range (Herkenhoff, Kirk, et al., 2004). Because of the uncontrolled lighting conditions on Mars, the uncertainties in the in-flight results are estimated to be larger than uncertainties in the preflight laboratory results; thus, the in-flight results are deemed to be consistent with the preflight results. In any case, the uncertainties in these results do not significantly affect MI radiometric calibration accuracy.

3.4. Radiometric Calibration Accuracy

On Sol 475, Pancam, Navcam, and MI images of the sky were obtained to compare radiometric responses of the cameras and determine the accuracy of the conversion from DN to radiance or reflectance. The spectral range of the Pancam filters (Bell et al., 2003) spans the spectral bandpass of the MI, unlike the Navcam, which has a narrow red bandpass (Maki et al., 2003; Soderblom et al., 2008). To accurately compare the radiometric response of the Pancam and MI cameras, the spectral response of the MI (Herkenhoff, Kirk, et al., 2004) and each left Pancam filter was used to calculate weighting factors for each Pancam filter needed to simulate the MI spectral bandpass. Specifically, the spectral responses of Pancam filters L3 through L7 overlap the spectral response of the MI. The response of each of these Pancam filters at −10 °C (Bell et al., 2004) was weighted by the normalized spectral response of the MI (also at −10 °C, the closest calibrated temperature to flight data) and integrated over the passband. The results were normalized (Figure 7) and used to predict the response of the MI to the same radiance observed by Pancam by summing the products of the radiance observed in each Pancam filter and the weighting factors. The Pancam data have an absolute radiometric calibration accuracy of about 10% (Bell et al., 2006). The results are summarized in Table 1, which shows that the MI response is within 20% of the Pancam response.

In summary, MI data acquired before the 2007 dust storm (Sols 2–1253) can be radiometrically calibrated to an absolute accuracy of 30% and relative (pixel-to-pixel) accuracy of 1.5% (Herkenhoff et al., 2006). Radiometric calibration of images acquired after the 2007 contamination of the MI optics is somewhat less accurate and is difficult to quantify due to the paucity of in-flight calibration data. However, other than the dust contamination, there is no evidence of significant degradation or change in the instrument behavior.

Radiometric calibration has been performed on all MI images, and the results released as standard Planetary Data System (PDS) Experiment Data Record products (Alexander et al., 2003). Improvements and additions to higher-level Reduced Data Record and other MI products, which are often more scientifically useful than the standard products, are described in the next section.

4. MI High-Level Data Processing

Standard MI data products include raw and radiometrically calibrated images. In addition, high-level MI data products have been generated using the procedures described by Herkenhoff et al. (2006). Updates to the data processing procedures are given in this section, as appropriate. There have been no updates to the processing of MI cover open/closed color composites, which have not been acquired since early in the *Spirit* mission due to dust contamination of the MI cover. Likewise, there have been no changes to the procedures for

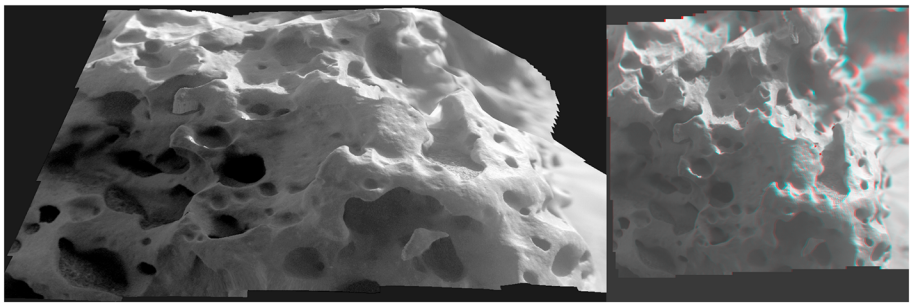

Figure 9. (left) Oblique view of Microscopic Imager orthomosaic draped onto digital elevation model generated using stereo images acquired on Sol 1053 of target *Palma* (location shown in Figure 1) on feature *Esperanza*. Area shown is 5×5 cm across, illumination from upper right. (right) Overhead red-blue anaglyph view of same target. The morphology of this rock is typical of wind-abraded terrestrial vesicular basalts (Arvidson et al., 2008).

generating mosaics of MI images, MI/Pancam color merges, or MI photoclinometry since they were described by Herkenhoff et al. (2006). Table 2 summarizes the updates to MI data products.

4.1. Focal Section Merges and Anaglyphs

Multiple MI images are typically acquired at various distances from each target to ensure that all parts of a rough target are imaged in good focus. The raw *focal sections* are returned to Earth and combined into well-focused merges using the IDL software tool described by Herkenhoff et al. (2006). A new tool for generating focal section merges is the Helicon Focus (HF) Software, developed and published by Helicon Soft Limited. Both IDL and HF software have been used to create focal merges, and each has individual strengths and weaknesses. The HF software may work better under certain conditions than the IDL software, and vice-versa. Of course, the quality of the focal merge is limited by the quality of the input images. Figure 8 shows an example where the HF product is better than the IDL product; shadow boundaries in images such as these commonly cause errors in focal merges and anaglyphs.

The HF image focus stacking algorithm combines a series of images, aligns, and blends the best-focused regions of each image into a composite image. This method effectively extends the depth of field of the MI. Nearly all of the focal merges created using HF are improved over those generated with IDL software described by Herkenhoff et al. (2006). Radiometrically calibrated (I/F), stretched (0.5% histogram) images are converted to TIFF format and imported into HF, where a processing method is selected. The method most often used to merge MI images searches a stack of images and locates the image that contains the sharpest pixel and subsequently creates a *depth map* from the information (https://www.heliconsoft.com/helicon-focus-main-parameters/). In addition, parameters are adjusted as needed to render a best overall merged image. Several iterations may be required to improve the initial focal merge using HF, for example, to eliminate possible doubling of features or perhaps to correct misalignment.

The focal merge created with the IDL software is compared against the output of HF, and the best product is archived in a special directory, although both focal merges are retained. The HF software does not create red-blue anaglyphs from the depth maps generated from focal sections; all anaglyphs are created using the IDL software.

4.2. Stereogrammetry

The methods used to process stereo MI images using BAE Systems' SOCET Set® software into digital elevation models (DEMs) were described by Herkenhoff et al. (2006). The post spacing of MI DEMs is typically 3 times the pixel scale, or 90 μm. Stereo images were typically offset 15 μm, yielding a base-to-height ratio of about 0.19. When the matching uncertainty is small (0.2 pixel) the resulting vertical (depth) precision approaches the pixel scale of 30 μm. Calculation of the expected precision of specific MI stereopairs yields values from 25 to 35 μm, consistent with the above estimate.

The effects of lossy image compression on extraction of DEMs from MI stereo pairs were determined by applying various levels of ICER quality compression to the images and using them to generate DEMs. These tests showed that ICER MINLOSS quality 2 or better (after 12 to 8-bit companding) does not affect

Table 3
Spirit MI Observations of APXS Rock Targets Classified by Ming et al. (2008)

Microtextural observations	Geochemical class	Geochemical subclass	Feature	MI/APXS target	MI sol(s)
Rounded to subrounded, coarse to very coarse, well-sorted grains, clast supported	Barnhill	Barnhill	Barnhill	Ace	747
	Barnhill	Barnhill	Barnhill	Fastball	750
	Barnhill	Barnhill	Posey	Posey Manager	754
	Barnhill	Barnhill	James *Cool Papa* Bell	Stars	761
	Barnhill	Barnhill	James *Cool Papa* Bell	Crawfords	763
	Barnhill	Barnhill	Home Plate Site 4	Pecan Pie	1368
	Barnhill	Pesapallo	Madeline English	Belles	1168
	Barnhill	Pesapallo	Fin Layer	Pesapallo	1205
	Barnhill	Pesapallo	Fin Layer	Superpesis	1209
	Barnhill	Pesapallo	Fin Layer	June Emerson	1211
	Barnhill	Pesapallo	Silica Valley	Elizabeth Emery	1216
	Barnhill	Pesapallo	Home Plate Site 3	Texas Chili	1330
	Halley	Graham Land	Enderbyland	King George Island	1027, 1031
	Halley	Graham Land	Enderbyland	King George Offset	1035
	Halley	Graham Land	Troll	Riquelme 3	1080
	Torquas	Torquas	Torquas	Torquas 1	1143
	Torquas	Torquas	Torquas	Torquas 2	1143
	Watchtower	Watchtower	Watchtower	Joker	415, 417
	Watchtower	Watchtower	Larry's Lookout	Paros	491
	Watchtower	Watchtower	Pequod	Ahab	495–6
	Watchtower	Watchtower	Pequod	Moby Dick	499
	Watchtower	Watchtower	Pequod	Doubloon	499
	Watchtower	Keystone	Methuselah	Keystone	469–70
	Watchtower	Keel	Jibsheet	Reef	481
	Watchtower	Keel	Jibsheet	Davis	484, 487
	Watchtower	Keel	Hillary	Namche Bazaar	633
	Watchtower	Keel	Hillary	Khumjung	633
	Watchtower	Keel	Kansas	Kestrel	646
Subangular to rounded, medium, well-sorted grains, clast supported	Algonquin	Comanche	Comanche Spur	Horseback	698–9
	Algonquin	Comanche	Comanche Spur	Palomino	700
Dark, rounded to subrounded coarse grains in brighter, porous matrix	Elizabeth Mahon	Elizabeth Mahon	Clara Zaph	Elizabeth Mahon	1157
	Elizabeth Mahon	Elizabeth Mahon	Silica Valley	Nancy Warren	1225, 1227
	Elizabeth Mahon	Elizabeth Mahon	Silica Valley	Norma Luker2	1291
	Elizabeth Mahon	Innocent Bystander	Silica Valley	Innocent Bystander	1251–2
	Elizabeth Mahon	Innocent Bystander	Silica Valley	Bystander Offset 2	1257, 1277
	Good Question	Good Question	Examine This	Good Question	1179
Bright, subangular to subrounded, medium to very coarse, poorly sorted grains, matrix supported	Independence	Independence	Independence	Jefferson	532
	Independence	Independence	Independence	Livingston	533
	Independence	Independence	Independence	Penn 2	538–9
Subrounded granules, poorly sorted	Independence	Assemblee	Assemblee	Gruyere	566, 571
Possible rounded coarse grains, matrix supported	Montalva	Montalva	Troll	Montalva	1070
	Montalva	Montalva	Troll	Montalva Offset	1080
Dark, poorly sorted subangular grains in brighter matrix	Halley	Halley	Enderbyland	Halley	809
	Halley	Halley	Enderbyland	Halley Offset	832
Subangular to subrounded, poorly sorted grains, clast supported	Algonquin	Algonquin	Larry's Bench	Thrasher	660
	Algonquin	Algonquin	Seminole	Osceola	672
	Algonquin	Algonquin	Seminole	Abiaka	675
	Algonquin	Algonquin	Algonquin	Iroquet	667–8
Angular to subrounded, poorly sorted grains, clast supported	Everett	Everett	Examine This	Everett	1172
	Everett	Everett	Examine This	Slide	1176
Smooth with millimeter-scale undulations, poorly sorted grains, matrix supported	Descartes	Descartes	Descartes	Discourse	552–3
	Descartes	Descartes	Bourgeoisie	Chic	557
	Descartes	Descartes	Bourgeoisie	Gentil Matrice	560
	Descartes	Descartes	Haussman	Rue Laplace	563
Smooth, massive, fine-grained, pitted	Backstay	Backstay	Backstay	Scuppers	509, 511

Table 3 *(continued)*

Microtextural observations	Geochemical class	Geochemical subclass	Feature	MI/APXS target	MI sol(s)
	Backstay	Backstay	Backstay	Scurvy	512
	Backstay?	Backstay?	Humboldt	Humboldt Peak	1340
	Fuzzy Smith	Fuzzy Smith	Close Target Rock	Fuzzy Smith	770
Smooth, massive, fine-grained, pitted	Irvine	Irvine	Irvine	Shrewsbury 2	600
	Irvine	Irvine	Esperanza	Palma	1053
	Irvine	Irvine	Arad	Masada	no images

Note. MI = Microscopic Imager; APXS = Alpha Particle X-Ray Spectrometer.

DEM generation. Therefore, this level of compression was used for all MI stereo images. An example of an MI orthomosaic draped over a DEM is shown in Figure 9.

4.3. Archived MI Data

There have been no significant changes to MI archival procedures since they were reported by Herkenhoff et al. (2006). Raw and radiometrically calibrated (I/F) MI data are available through the PDS and can be searched using the PDS Planetary Image Atlas: https://pds-imaging.jpl.nasa.gov/search/?fq=ATLAS_MISSION_NAME%3A%22mars%20exploration%20rover%22&fq=ATLAS_SPACECRAFT_NAME%3Aspirit&fq=ATLAS_INSTRUMENT_NAME%3Ami&q=*%3A*. These MI products, as well as focal section merges and anaglyphs, can be found on the Analyst's Notebook: https://an.rsl.wustl.edu/mera/merxbrowser/. We recommend that calibrated MI data products be used for scientific analyses, because they can be quantitatively compared with other calibrated camera data and theoretical radiative scattering models (e.g., Hapke 1993). Merges of *Spirit* MI and Pancam color images (see examples in Figure 21) are available at http://pancam.sese.asu.edu/images/merges/merges.html and http://astrogeology.usgs.gov/maps/mars-mer-mi-merged-products/spirit-mi-pancam-merges. When the ongoing migration of United States Geological Survey websites is completed, these and other high-level *Spirit* MI products will be available at https://www.usgs.gov/centers/astrogeo-sc/science/mer-mi-products.

5. Overview of Results

The scientific results of MI observations acquired by *Spirit* after Sol 450 are summarized in this section. Results of the MI investigation during the first 450 sols of the *Spirit* mission were summarized by Herkenhoff, Squyres, et al. (2004) and Herkenhoff et al. (2006). Observations of rocks in the Columbia Hills (Arvidson et al., 2008; McCoy et al., 2008) within Gusev crater are discussed below, followed by a discussion of soil observations.

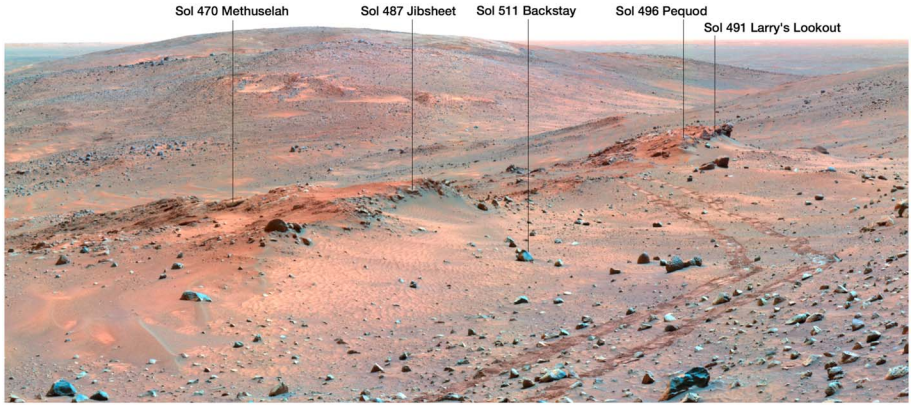

Figure 10. Pancam enhanced-color mosaic generated using the 753 μm (red, L2), 535 μm (green, L5), and 432 μm (blue, L7) filters (hereafter, this filter set is referred to as L257) of Cumberland Ridge, acquired on Sol 454 looking ~north. Note that rover tracks at bottom right span 1.2 m. Locations of Microscopic Imager images shown in Figures 11 and 14 are indicated by black lines.

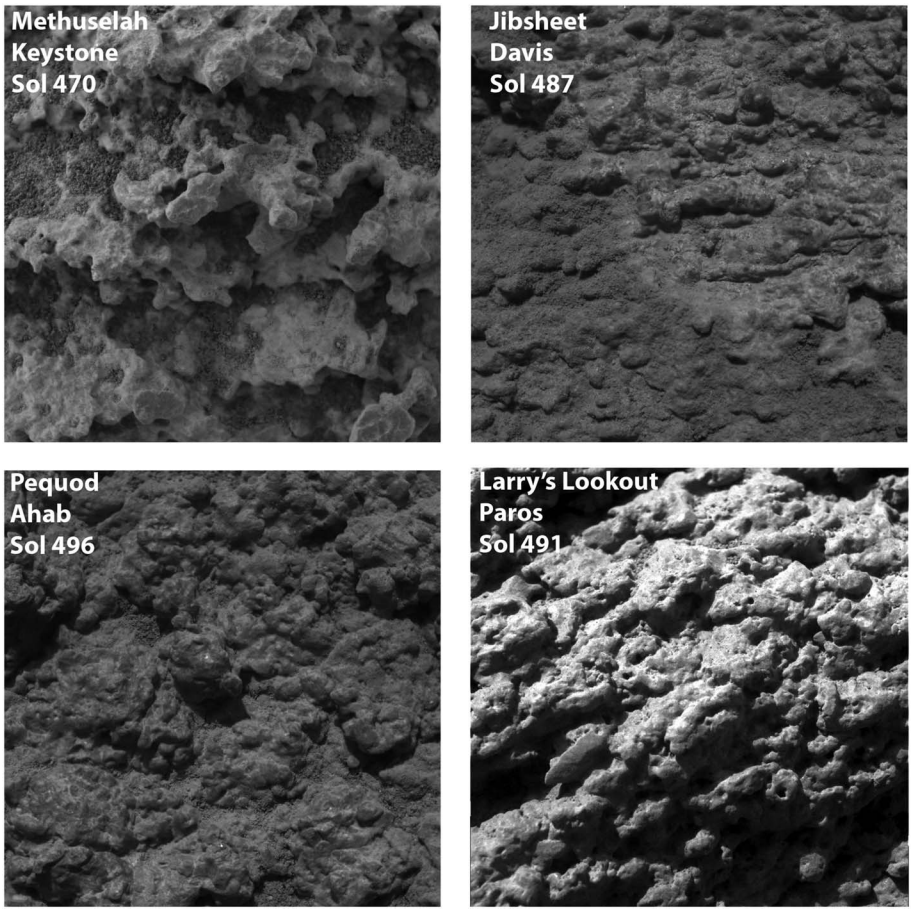

Figure 11. Microscopic images of Cumberland Ridge rock targets. Each image is ~3 cm across. Note the nodular texture, with knobby protuberances that increase in size from west to east (see Figure 10 for context). Methuselah's layers are deeply scalloped, following individual knobby protuberances. The knobby protuberances in the Jibsheet and Pequod features are composed of distinct, cemented smaller grains. Individual grains within knobby protuberances are less apparent in the Larry's Lookout target *Paros*. Illumination is from upper left except for *Keystone*, which was imaged while the target was completely in shadow. Keystone: focal merge A470_Keystone_21_raw. Davis: focal merge A487_Davis_3_raw. Ahab: focal merge A496_Ahab_2_raw. Paros: image 2M169952060.

In addition, the MI observed *Spirit*'s filter and capture magnets on Sols 505, 597, 963, 1006, 1125, 1230, 1239, and 1473 (Madsen et al., 2009; Vaughan et al., 2010). The MI was also used to image *Spirit*'s solar panels to assess contamination by dust and sand, and the area under the rover when it became stuck (see Appendix A for listing by sol).

5.1. Rock Observations

The descriptions and discussion of rocks observed by the MI are organized below according to the geochemical classification scheme of Squyres et al. (2006) and Ming et al. (2008) to facilitate comparisons with these and other previous publications. MI observations of rocks in the *Adirondack*, *Clovis*, *Wishstone*, *Peace*, and *Watchtower* geochemical classes were discussed previously (Crumpler et al., 2011; Hamilton & Ruff, 2012; Herkenhoff et al., 2006; McSween, Wyatt, et al., 2006). Additional rocks in the Watchtower class were investigated after Sol 450 and are therefore discussed below. The new classes of rocks examined by the MI are *Backstay*, *Irvine*, *Independence*, *Descartes*, *Algonquin*, *Barnhill*, *Fuzzy Smith*, *Elizabeth Mahon*, *Halley*, *Montalva*, *Everett*, *Good Question*, and *Torquas* (Ming et al., 2008). These geochemical classes are named after the features or targets listed in Table 3; their textural characteristics are summarized below. The observed textures and chemical trends indicate that the rocks were primarily formed by volcanic and impact processes and then modified by varying amounts of aqueous alteration.

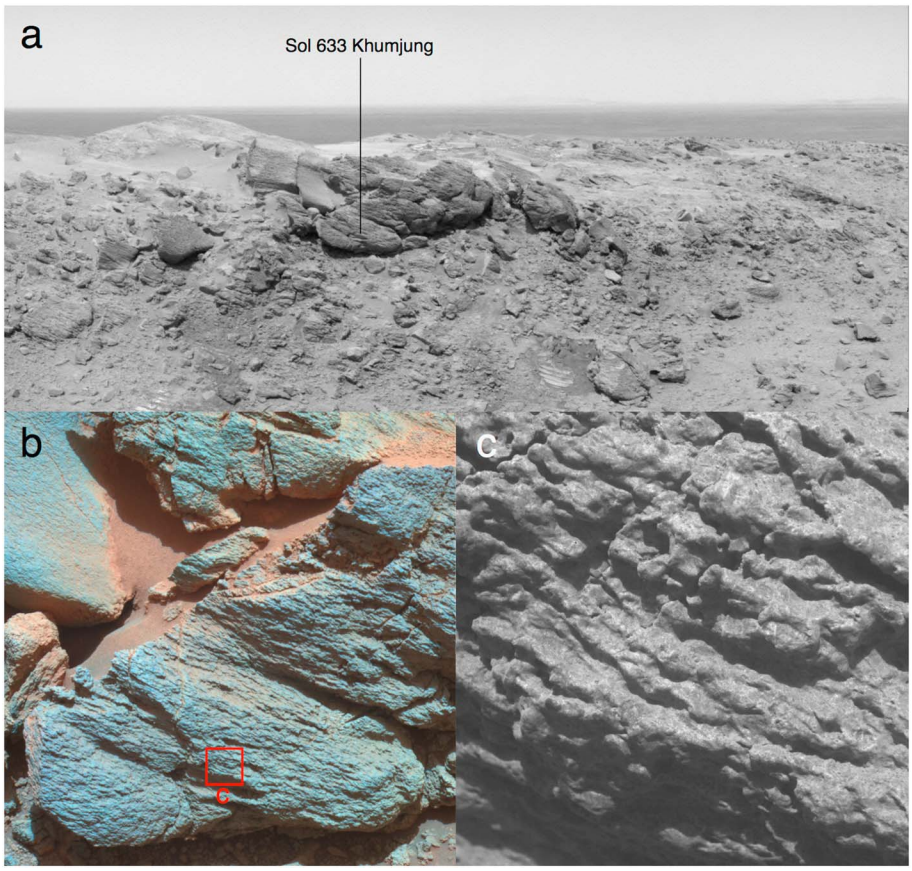

Figure 12. (a) Sol 634 Navcam view of Watchtower class feature *Hillary* at the summit of Husband Hill. (b) Sol 634 Pancam enhanced-color (L257) view showing part of the Hillary outcrop. Linear textures emphasized by shading hint at possible scalloped layering, although aeolian abrasion effects are also apparent. (c) Microscopic Imager image 2M182563021 (3 × 3 cm), part of a 2 × 3 mosaic of the *Khumjung* target on the Hillary feature. Rounded, knobby protuberances at Microscopic Imager resolution reveal that scalloped linear textures observed at Pancam resolution do not resolve into layers having any continuity.

Altered and high Ti and P basaltic debris of the Watchtower class shows a variety of microtextures (Cole et al., 2014; Herkenhoff et al., 2006) consistent with altered basaltic airfall material, emplaced by impact and/or volcanic processes. The observed textural variety (Figures 11–13) may be due to variations in the extent of aqueous alteration.

Alkaline volcanic rocks of the Backstay and Irvine classes are relatively unaltered, smooth, fine-grained basalts (Figures 14 and 15).

Matrix-supported sedimentary rocks include Independence subclass low-Fe medium to coarse sandstone (Figure 16), *Assemblee* subclass high-Cr conglomerate (Figure 17), and Descartes class lightly altered impact breccia (Figures 18 and 19).

Mafic-ultramafic magmatic sequence rocks include Algonquin subclass poorly sorted, grain-supported sediments (Figure 20) and *Comanche* subclass stratified, well-sorted ultramafic sediment containing carbonate (Figure 21).

Volcaniclastic sediments of the Barnhill and *Pesapallo* subclasses are partly reworked volcanic debris that forms Home Plate (Figures 22–25).

Silica-rich rocks include Fuzzy Smith, a fine-grained hydrothermally altered rock, Elizabeth Mahon, and Good Question (porous, cemented volcaniclastic rocks; see Figure 26). *Stapledon* was not included in the Ming et al.

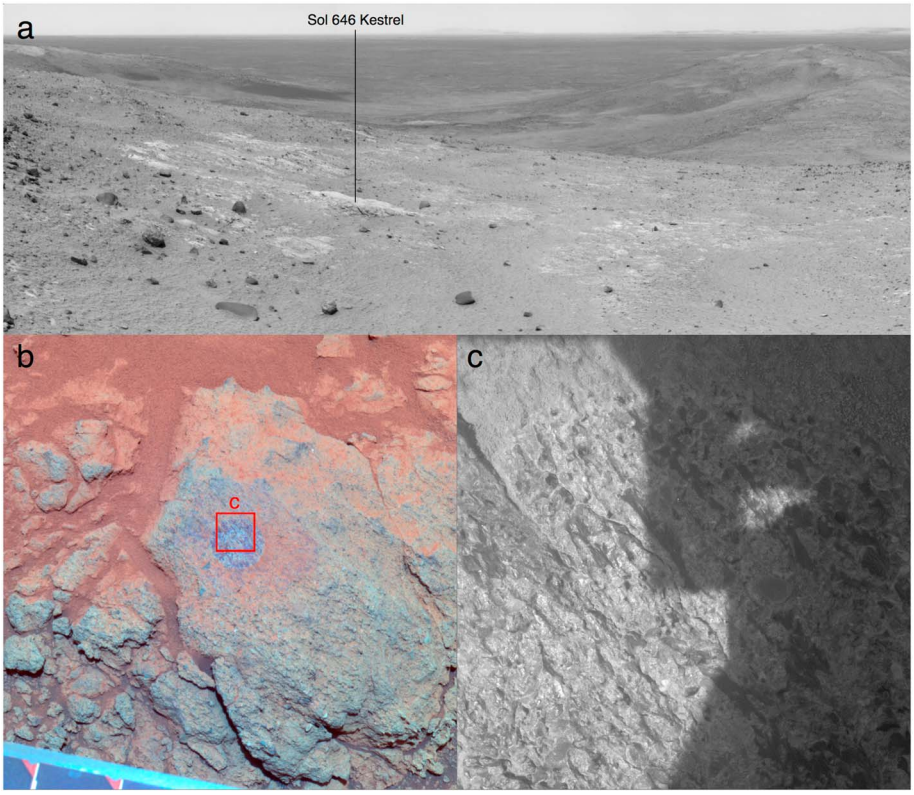

Figure 13. The Kansas target *Kestrel*, as seen in (a) Navcam mosaic looking ~NW, (b) Pancam enhanced color (L257) image with area shown in Microscopic Imager image outlined in red, and (c) Microscopic Imager image 2M183719252, acquired on Sol 646 when target was partly shadowed. Pancam and MI images were both taken after Rock Abrasion Tool brushing.

(2008) classification, but its high silica content and similar texture indicate that it belongs in this geochemical class.

Hematite-rich outcrops such as Halley are clastic rocks containing likely hematitic concretions (Figure 27). Montalva is an altered clastic rock that is also potassium rich.

Other geochemical classes include Everett, a high-Mg, well cemented volcaniclastic rock (Figure 28) and Torquas, a magnetite-rich, well sorted, reworked sandstone (Figure 29).

5.1.1. Watchtower Class Rocks

Watchtower class outcrops occur across much of the upper elevation range of Husband Hill, including both sides of *Tennessee Valley* (Figure 1). The chemical similarity of these outcrops is consistent with a common genesis; these various outcrops represent a single stratigraphic unit that can be correlated for hundreds of meters across Husband Hill.

Spirit examined several Watchtower class outcrops, on *Cumberland Ridge* (features *Methuselah*, *Jibsheet*, and *Larry's Lookout*), the Husband Hill summit (feature *Hillary* and other unnamed outcrops), and Haskin Ridge (*Kansas* feature, Ming et al., 2008; Squyres et al., 2006). Watchtower class rocks are interpreted as aqueously altered basaltic airfall material. This class has been divided into subclasses based upon iron mineralogy and oxidation state (Morris et al., 2006, 2008), visible and near-infrared spectral characteristics (Farrand et al., 2008), and thermal IR spectral characteristics (Ruff & Hamilton, 2017). While Watchtower class rocks are remarkably consistent in elemental abundances, including the soluble elements Cl and Br, they are remarkably varied in iron mineralogy (Gellert et al., 2006; Hurowitz et al., 2006; Ming et al., 2006, 2008; Morris et al., 2006, 2008; Squyres et al., 2006) and Mineral Alteration Index (MAI, Morris et al., 2006, 2008). This combination is consistent with aqueous alteration at a low water-to-rock ratio. The iron oxidation state Fe^{3+}/Fe_{tot} on Cumberland Ridge increases systematically from west to east, ranging from 0.43 to 0.94 (Morris et al., 2006, 2008).

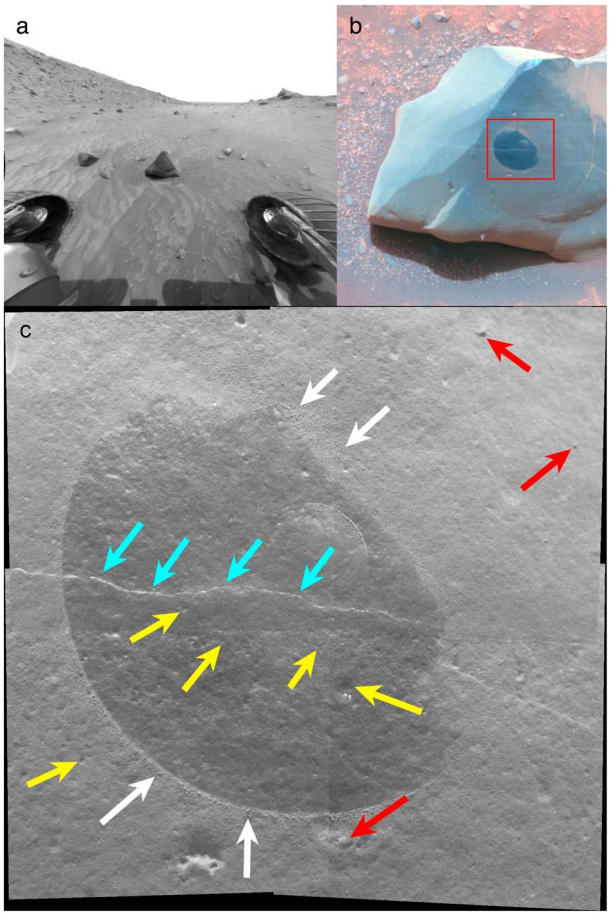

Figure 14. (a) Sol 508 Front Hazcam view of Backstay, a float rock that can also be seen in wider geological context in Figure 9. (b) Sol 511 Pancam enhanced-color (L257) view of Backstay, with area shown in Figure 14c outlined in red. Note small protrusion at lower center, probably representing inclusion that is relatively more resistant to eolian abrasion. (c) The 2 × 2 Microscopic Imager mosaic 2MM511ILFAAPERJCP2957 M222M2 of target *Scuppers*, taken on Sol 511 after Rock Abrasion Tool brushing, with illumination from top. Note the fracture (blue arrows), pits (yellow arrows), and protrusions (red arrows). Dust disturbed by the Rock Abrasion Tool is highlighted with white arrows. Area shown is about 5 × 5 cm.

5.1.1.1. Cumberland Ridge

The Cumberland Ridge outcrops in the Watchtower class (from west to east, Methuselah, Jibsheet, and Larry's Lookout features; see Figure 10) are located on northwestern Husband Hill. As seen in Pancam images, these outcrops are stratified, and MI images show that grains are well sorted and grain supported (Cole, 2015). The ~0.35- to 0.4-mm grains appear to be cemented into nodular aggregates (Figure 11; note that in this article we use the term *cement* to mean the mineralized or amorphous material that binds together the smallest visible particles: no genetic process is implied). Where individual grains are clearly visible, they appear to be subangular to subrounded, but the cementing agent makes an absolute determination of roundness difficult. The knobby, protruding aggregates increase in size from west to east, with average sizes of ~1.3, ~1.8, ~2.0, and ~2.2 mm on Methuselah, Jibsheet, Pequod, and Larry's Lookout, respectively. Jibsheet's morphology is intermediate between those of Methuselah and Larry's Lookout, and Pequod is intermediate between Jibsheet and Larry's Lookout (Figure 11). The knobby protuberances on Jibsheet and Pequod appear morphologically to be agglomerations of smaller grains, while those on Larry's Lookout exhibit a smoother texture, consistent with an increase in cementing agent from west to east. Methuselah is clearly layered, with edges showing a scalloped appearance, possibly following the contours of the entrained nodular aggregates.

5.1.1.2. Husband Hill Summit and Haskin Ridge

The microtexture of the summit Watchtower class outcrops exhibits some aspects that are similar to Cumberland Ridge targets (Figure 12). But while linear textures are also evident in Pancam images of these outcrops, they are interpreted as having been formed primarily by eolian abrasion rather than sedimentary stratification. As in the Methuselah feature, the scalloped edges of lineations appear to follow the contours of entrained nodular aggregates, which here range in size from ~1.3 to ~1.5 mm. Linear microridges extend downwind of more resistant clasts/nodules due to differential erosion by a directed source (wind). This interpretation is supported by Pancam images in which individual layers cannot be traced and variations in the orientation of linear features are consistent with eolian abrasion (Figure 12b). If there are sedimentary layers in the summit rocks, variations in resistance to abrasion between them are too slight for such layers, if they exist at MI scale, to be expressed via differential erosion from sand blasting. Instead, contrasts in abrasion resistance between matrix and somewhat more resistant inclusions/clasts are greater and more controlling and combine with sand blasting to dominate the observed surface texture.

The microtexture of the Kansas feature, on Haskin Ridge, is difficult to discern due to the lighting conditions during image acquisition, but appears to be poorly sorted, with more angular grains (Figure 13). Kansas is composed of 1- to 2-mm thick laminae, which are common to many of the ledge-forming outcrops of the Columbia Hills. The *Kestrel* target shows well-sorted 1- to 2-mm grains typical of a lapilli tuff (Crumpler et al., 2011), a lithified aggregate of ash and lapilli.

5.1.2. Backstay Class Rocks

Backstay, the type rock for this class, is a smooth, faceted float rock located in front of the Jibsheet feature on Cumberland Ridge (Figure 10). Several additional instances of Backstay class rocks were identified on Husband Hill, all as float (Ruff et al., 2006). Backstay has a considerably smoother microtexture than the nearby Watchtower class outcrops and surrounding float and is similar in appearance to Adirondack, the crystalline basalt that is the characteristic float on the Gusev plains. Backstay exhibits shallow pits and up to ~0.6-mm protrusions that may be phenocrysts that are more resistant to eolian abrasion (Figures 14b and 14c). A

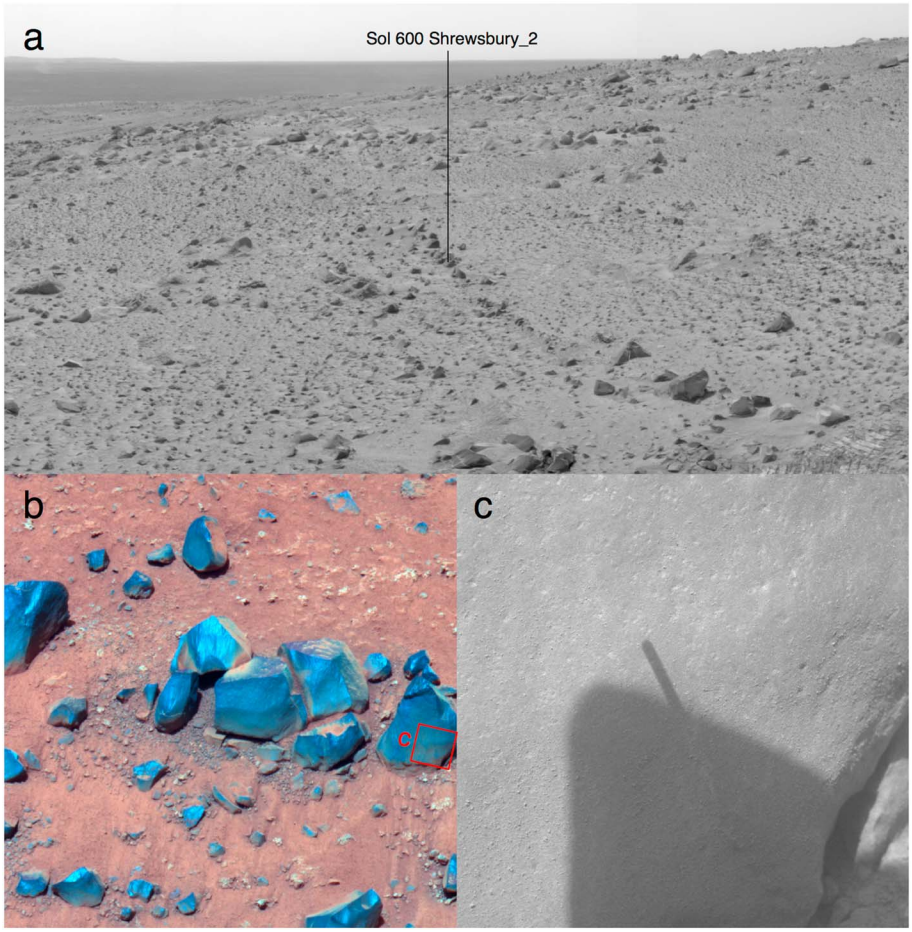

Figure 15. (a) Sol 598 Navcam view showing dark rocks arranged in what seems to be a linear array near the summit of Husband Hill. (b) Sol 603 Pancam enhanced-color (L257) view of the Irvine group of these dark rocks. Colors indicate little dust on near-vertical rock surfaces. (c) Merge of two Microscopic Imager images of target Shrewsbury_2, acquired on Sol 600 when target was partly shadowed by the Instrument Deployment Device. This rock is smooth and fine grained, with a massive microtexture similar to that of Backstay and only a sparse scattering of very small dust aggregates. View is ~3 cm across; location of Microscopic Imager image outlined in red in Figure 15b.

bright curvilinear feature that extends across the rock surface is likely a fracture partly infilled with dust. Backstay is interpreted as a lava or dike rock (McSween, Wyatt, et al., 2006).

Backstay class rocks are depleted in Fe and enriched in Ti, Al, K, and Na relative to Adirondack class rocks; their geochemistry and mineralogy are consistent with a relatively unaltered basalt/trachybasalt (Ming et al., 2008; Squyres et al., 2006).

5.1.3. Irvine Class Rocks

While traversing between Cumberland Ridge and the Husband Hill summit, *Spirit* observed a linear array of small angular rocks suggestive of eroded fragments of an intrusive dike (Figure 15a). Notwithstanding the arrangement of these rocks and their basaltic composition, there is no firm evidence that this linear cluster indeed represents a dike, and the rocks may in fact be float material (McSween, Ruff, et al., 2006; Ruff et al., 2006). On a microscopic scale, the texture of the Irvine class rock *Shrewsbury_2* is similar to the relatively unaltered Adirondack class basalt and Backstay class basalt/trachybasalt (Figure 15c); it is consistent with crystallized volcanic rock. Its microtexture is smooth, with ~0.1- to 0.5-mm pits and protuberances consistent with wind-abraded and resistant phenocrysts, respectively. Alternatively, as the target was not brushed by the RAT, the protuberances may be dust agglomerates. The wind-abraded vesicular rock Esperanza (Figure 9) has a chemical composition similar to Irvine (Ming et al., 2008).

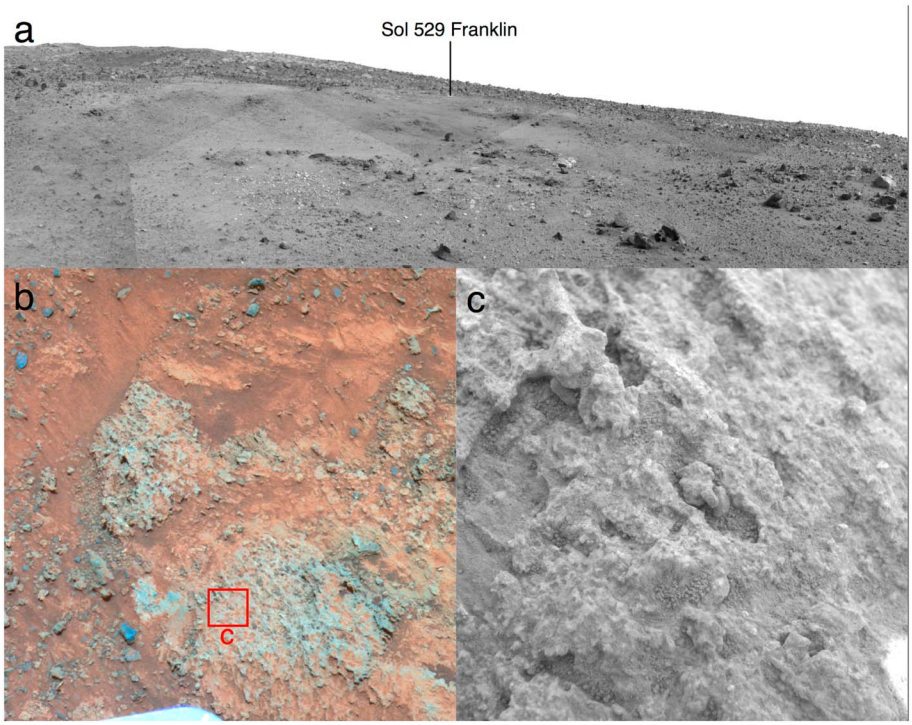

Figure 16. (a) Sol 524 Navcam view showing the setting of the feature *Independence* near the summit of Husband Hill. (b) Sol 536 enhanced-color (L257) Pancam view of Independence revealing eolian scouring from upper left to lower right that has affected the rock surface and, more recently, the surrounding regolith. (c) Merge of Microscopic Imager focal sections of Independence subclass target *Franklin*, acquired on Sol 529 in full shadow. The irregular surface here displays poorly sorted, matrix-supported grains weathering out due to eolian abrasion (note the erosional spire extending beyond upper left margin of the image, consistent with interpretation from Pancam image) and probably other weathering processes.

5.1.4. Independence and Descartes Class Rocks

Spirit encountered the Independence and Descartes class lithologies to the southwest of Tennessee Valley while traversing from Cumberland Ridge to the Husband Hill summit. Independence and Descartes display pits and undulations (see Figures 16 and 18b); the latter has similar wavelengths and may have been formed by eolian abrasion. Despite its geographic location within the Descartes site, Assemblee is more chemically similar to Independence (Ming et al., 2008).

5.1.4.1. Independence Subclass

Independence is a bright outcrop with low relief, located ~100 m southwest of Cumberland Ridge. At MI scale, its surface is rough, with irregularly shaped cavities ranging in size from ~1 mm to >1 cm (Figure 16c). The texture is granular, with bright, poorly sorted, matrix-supported clasts that are typically subrounded to subangular. Approximately 0.4- to 0.5-mm clasts dominate, but diameters range up to ~1.5 mm; the larger clasts may be cemented. Independence has nearly the lowest Fe abundance of all Gusev rocks examined by the APXS and is enriched in Ni, Si, and Al relative to Adirondack class rocks (Ming et al., 2008). Together, these observations suggest that Independence is a medium to coarse sandstone with meteoritic material in the clasts and/or cement. The rock may also contain montmorillonite or its compositional equivalent (Clark et al., 2007).

5.1.4.1.1. Assemblee Subclass

Assemblee is a small, knobby outcrop adjacent to the Descartes class outcrops, ~100 m southeast of Independence. Despite Assemblee's chemical similarity to Independence, the microtextures of these two subclasses are markedly different (Figure 17). Assemblee is fractured in several locations and is poorly sorted, with large embedded, faceted, subrounded clasts that are unique to this subclass. The clasts' texture is smoother than the surrounding matrix. Diameters are typically ~3.2 mm but range from ~1.7 to ~6 mm. The matrix, which exhibits ~0.15 and ~1 mm pits and knobs, is considerably smoother than that of

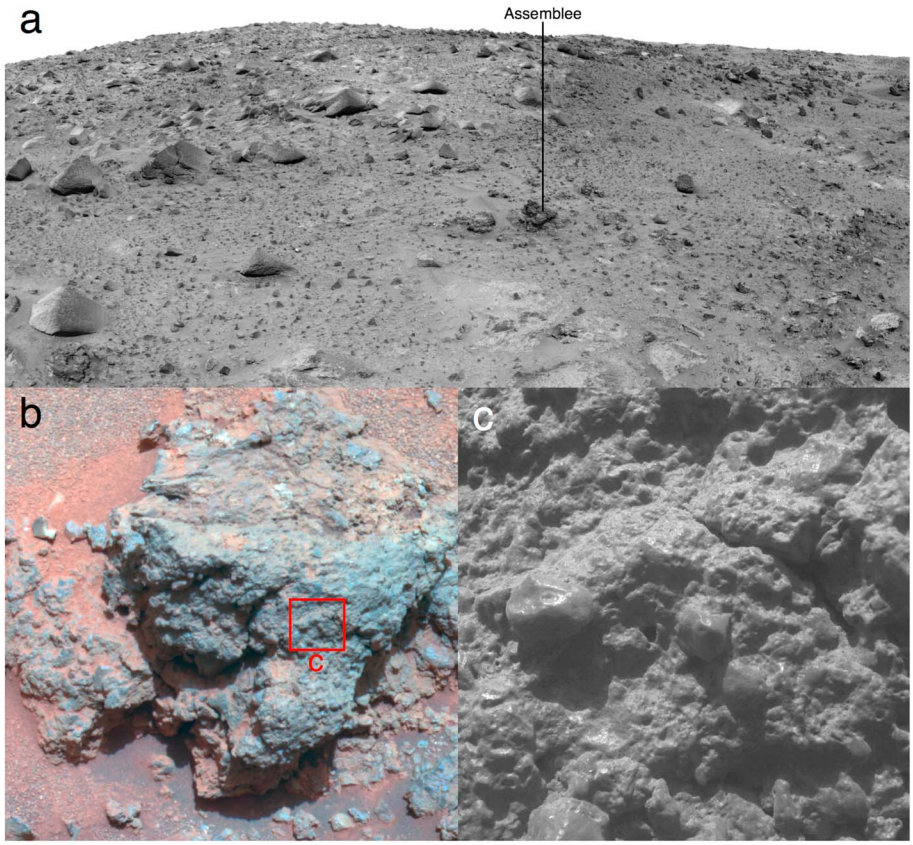

Figure 17. (a) Sol 556 Navcam view of feature *Assemblee* near the summit of Husband Hill (see also Figure 19a). Rocks with similar morphology to Assemblee are more common in the foreground at lower right and differ from the morphology of larger, presumably more resistant rocks at the upper left in this view. (b) Sol 572 Pancam L257 enhanced-color view of Assemblee revealing large, resistant, subrounded clasts or inclusions weathering from a weaker matrix. The 3 × 3-cm area shown in Figure 17c is outlined in red. (c) Merge of Microscopic Imager focal sections of Assemblee subclass target *Gruyere*. Images acquired on Sol 566 with illumination from upper left. Even at this scale, it is unclear whether the subrounded shapes of the clasts or inclusions are primary or are being acquired upon exposure by weathering.

Independence. Numerous ~0.4- to 0.5-mm features, notably similar in size to clasts in Independence, may be grains embedded in the matrix. These observations are consistent with Assemblee being a conglomerate but it probably formed by impact rather than fluvial processes.

5.1.4.2. Descartes Class

The overall microtexture of Descartes class rocks is smooth with millimeter-scale topographic undulations. It is matrix supported, with clasts that range in size from below the MI resolution to >1 cm (Figure 18). The matrix features bright and dark regions, which may reflect differences in composition or in dust coverage. In one location, a filled fracture or vein cuts across both matrix and a large clast (Figure 18b). Other regions (Figure 19) exhibit undulations and ~0.3- to 4.3-mm pits that may have been formed by eolian abrasion. The large clasts themselves contain grains up to ~0.5 mm in size, within a fine-grained matrix. This is consistent with these clasts themselves being fragments of poorly sorted, matrix-supported clastic rock; Arvidson et al. (2008) identified one large embedded clast as Wishstone class and interpreted Descartes as a breccia that formed as the result of an impact into local materials.

5.1.5. Algonquin Class Rocks

As *Spirit* descended the southeast flank of Husband Hill, she encountered five outcrops that may represent a mafic-ultramafic igneous fractionation sequence, becoming increasingly ultramafic with decreasing elevation (Ming et al., 2008, McSween et al., 2008). In descending order of elevation, these are *Larry's Bench*, *Seminole*, Algonquin, and the Comanche and Comanche Spur features. The geochemical sequence has been divided into the Algonquin subclass, encompassing Larry's Bench, Seminole, and Algonquin, and the

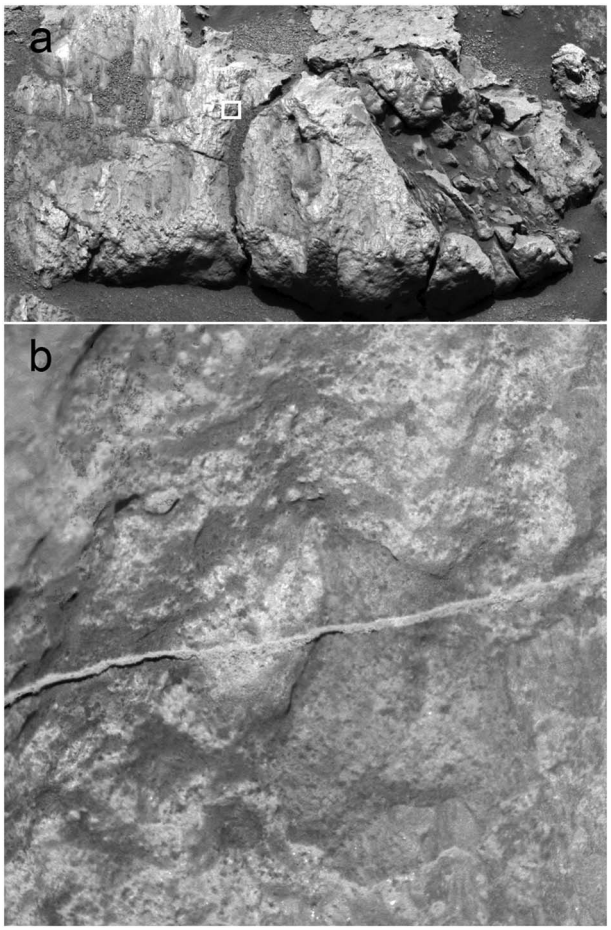

Figure 18. (a) Radiometrically calibrated blue (L7) Pancam subframe 2P175278228IOFAD40P2558L7M1 of the Descartes feature, acquired on Sol 551, with the 3 × 3-cm area shown in Figure 18b outlined in white. See Figure 19a for context. (b) The *Discourse* target on the Descartes outcrop. Focal merge of Microscopic Imager images taken on Sol 552 with illumination from top. A vein or filled fracture cuts across both matrix and a 1.7 cm embedded lithic fragment.

Comanche subclass, encompassing Comanche and Comanche Spur (Ming et al., 2008). The Algonquin subclass microtextures are similar to each other and are quite distinct from the Comanche subclass microtextures observed by the MI.

5.1.5.1. Algonquin Subclass

The Algonquin subclass targets are poorly sorted and grain supported. Subangular to subrounded clasts are evident in all outcrops, though microtextures vary. The *Thrasher* target on Larry's Bench, the northernmost Algonquin subclass outcrop, exhibits significant relief; the RAT brush removed dust from the higher relief regions only (Figure 20b). A linear fracture runs across this target. Other curvilinear features may represent bedding or fractures, or they may have been etched by eolian processes. The brushed area exhibits dark clasts with sizes ranging from below the MI resolution to ~0.5 mm. Smooth, dark regions, with a grain size below the MI resolution of 0.1 mm, appear to follow the contours of the rock and may be a surface coating. Alternatively, the RAT's brush may have been more effective in removing material from these areas.

Seminole consists of poorly sorted, millimeter-scale grains with texture similar to that seen in Thrasher (Crumpler et al., 2011). Seminole exhibits a jagged, *hackly* texture (Yingst et al., 2007), with a few smooth, dark features that may be a surface coating, or may have resulted from the RAT brushing (Figure 20d). Brushing did not remove dust in the depressions. Grains ~0.3–0.5 mm across dominate, but grain sizes range from below MI resolution to ~0.6 mm. Crumpler et al. (2011) concluded that Algonquin is a coarsely sorted, immature sandstone including lithic fragments, distinct from the underlying units. Ruff et al. (2014) interpreted the observations as indicative of volcanic tephra rather than detrital sediments.

RAT brushing was most effective on the Algonquin target *Iroquet*. Algonquin exhibits the widest variety of grain sizes and shapes (Figure 20f), though this may be due to the suitability of its surface for sample preparation and analysis by the IDD instruments. Clasts range in size from below MI resolution to ~1.8 mm and exhibit a range of reflectances. Many clasts are highly angular.

5.1.5.2. Comanche Subclass

Comanche was the first in situ example of carbonate-bearing rock identified on Mars; it contains 16–34 wt % carbonate (Morris et al., 2010). Its microtexture is notably different from that of Algonquin and is like that of Watchtower (Figure 21; Cole et al., 2014). It is layered at centimeter scale, nodular, and grain supported, with a low concentration of cementing agent between protruding grains. The ~0.5-mm grains are well sorted, subangular to rounded, and larger than the grains in the Algonquin subclass. In situ measurements were performed only on the Comanche Spur feature, but Mini-TES thermal infrared observations are consistent with a common composition spanning the two outcrops (Morris et al., 2010). The microtexture of Comanche Spur is not consistent with an igneous carbonatite nor is its high olivine abundance (Le Bas, 1981; Morris et al., 2010). Both the texture and the mineralogy are consistent with carbonate precipitation from a neutral-pH fluid; the carbonate may reside in the grains as globules (Morris et al., 2010) and/or in the cement.

The rounded particles in the *Palomino* target on Comanche Spur are similar to lapilli seen elsewhere on Husband Hill and the basin to the south (Crumpler et al., 2011). Ruff et al. (2014) hypothesized that the coarser grains in Comanche relative to Algonquin could be the result of particle-size sorting of pyroclastic debris with distance from a single volcanic vent or separate eruptions with slightly different characteristics.

5.1.6. Barnhill Class Rocks

Spirit spent most of her mission in the vicinity of Home Plate, which has been interpreted as an erosional remnant of a volcaniclastic or impact-generated deposit that has been partly reworked by eolian processes

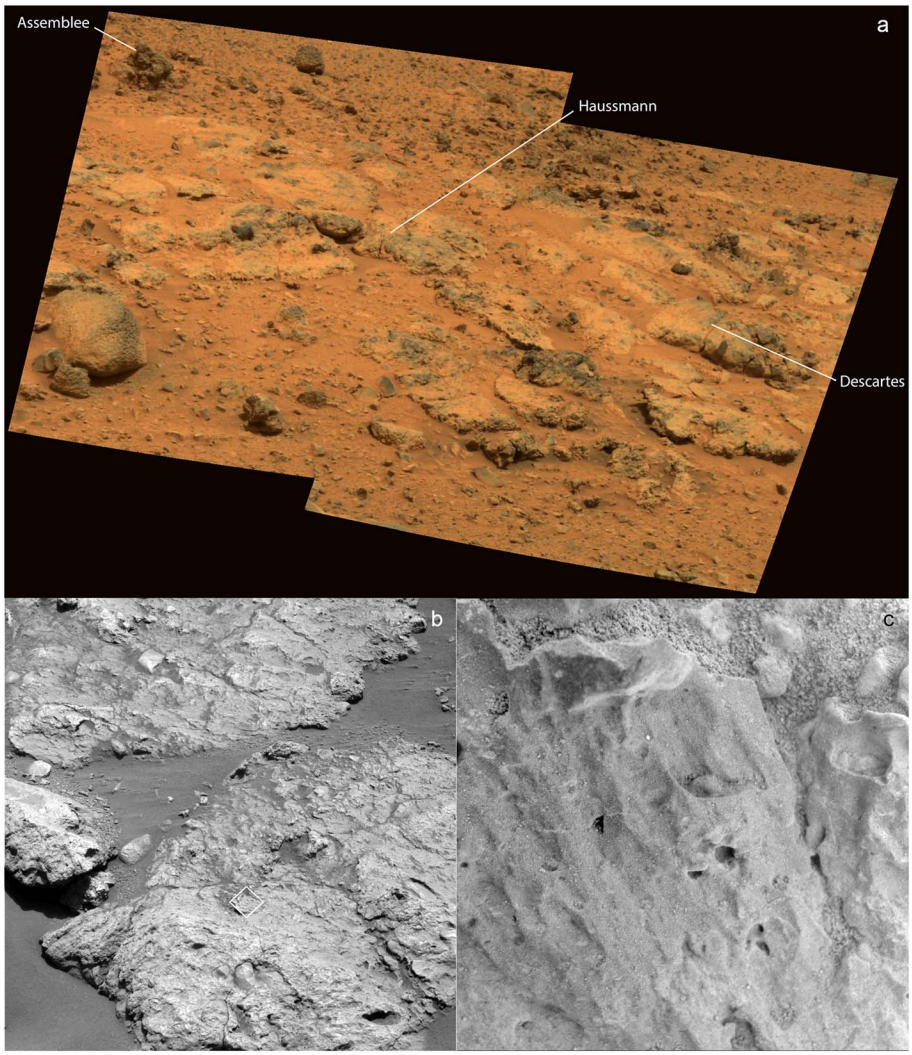

Figure 19. (a) Greyscale version of L257 Pancam mosaic of *Haussman* feature and vicinity, acquired on Sol 550. (b) Radiometrically calibrated blue Pancam image 2P175544154IOFAD56P2573L7M1 of the Haussmann feature, taken on Sol 554, with 3 × 3-cm area shown in Figure 19c outlined in white. (c) Radiometrically calibrated Microscopic Imager image 2M176344321 of the *Rue Legendre* target, acquired on Sol 563 when target was fully shadowed. Note the pits and undulations.

(Arvidson et al., 2008; Ming et al., 2008; Squyres et al., 2007; Yingst et al., 2010). Among the rocks first examined at Home Plate are those of the Barnhill subclass. Rocks in the *Pesapallo* subclass, on the east side of Home Plate, were studied later in the mission and show microtextures that are similar to those seen in MI images of rocks in the Barnhill subclass.

Rock targets Pesapallo, *Superpesis*, *June Emerson*, and Barnhill are distinguished by the predominance of rounded, similarly sized (0.5–1.5 mm) grains (Figure 22). Lewis et al. (2008) interpreted the knobby texture of Barnhill as the result of diagenetic or weathering processes that have obscured the original clastic texture. While the individual grains dominate the texture of targets in the Barnhill geochemical class, heterogeneous wear leaving stalks and subparallel ridges and rims all indicate significant amounts of a welding or a cementing agent that is less resistant to wear than the grains themselves. The texture is dominated by the individual grains but is strongly influenced by the cementing/welding agent. This is seen most strongly at the Barnhill feature, shown in Figure 22.

MI images of rock targets *Snout*, *Betty Wagoner*, *Elizabeth Emery*, and *Jane Stoll* show subrounded to angular grains, cemented together in a clast-supported matrix. Grains are darker and more reflective

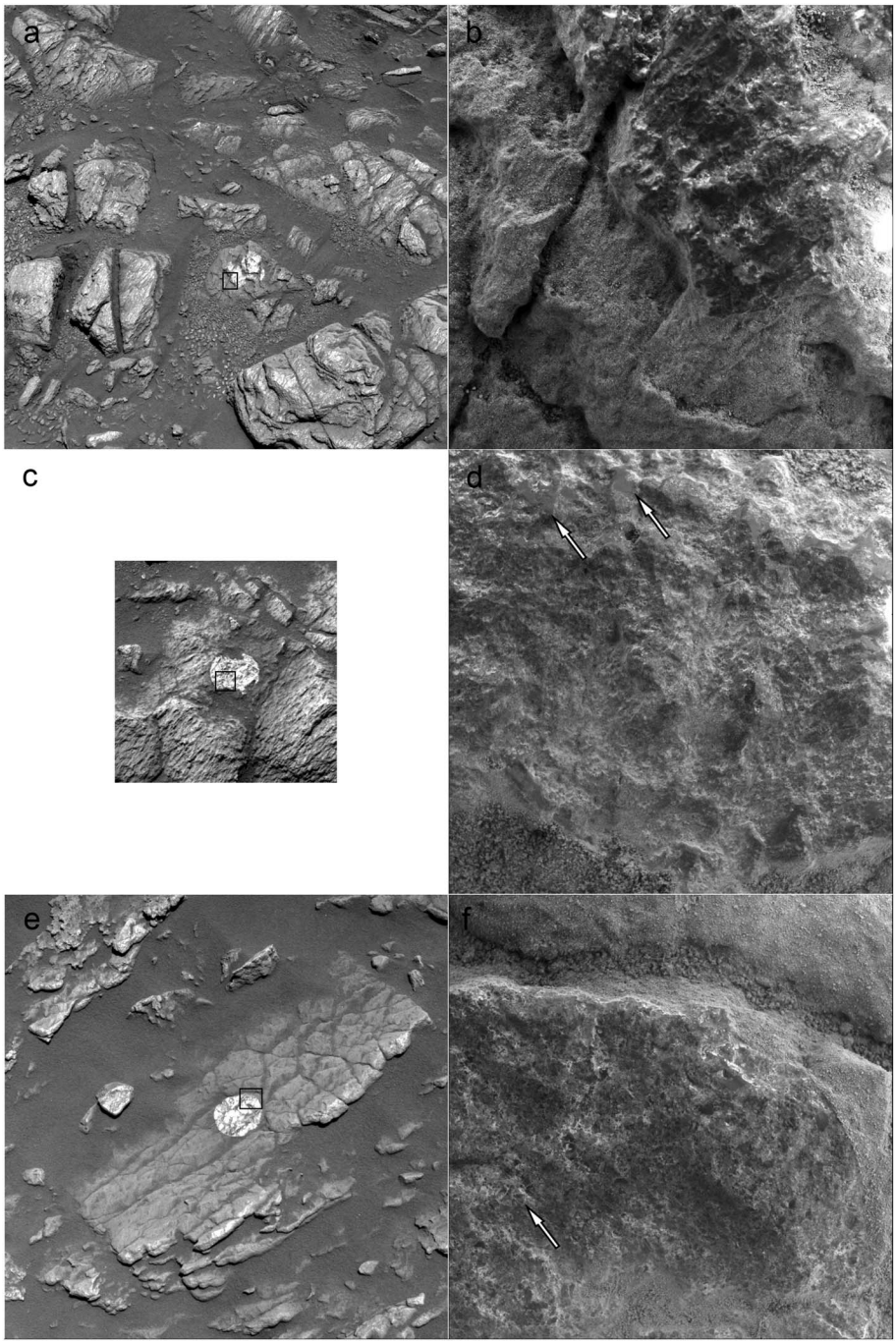

Figure 20. Brushed Algonquin class targets; see Figure 1 for locations. (a) Radiometrically calibrated blue Pancam image 2P185310882lOFAJB3P2535L7C6 of the Larry's Bench feature, taken on Sol 664, with 3 × 3-cm area shown in Figure 20b outlined in black. (b) Merge of Microscopic Imager images of Thrasher acquired on Sol 660, when the target was almost completely in shadow. Smooth, dark patch above and right of center may be a surface coating or an area on which the Rock Abrasion Tool brush was particularly effective. (c) Radiometrically calibrated blue Pancam subframe 2P186560057lOFAJQXP2552L7M1 of the Seminole feature, taken on Sol 675, with 3 × 3-cm area shown in Figure 20d outlined in black. (d) Radiometrically calibrated Microscopic Imager image 2M186289443 of *Abiaka* target, acquired on Sol 675 when target was in full shadow. Arrows point to smooth, dark spots that may be surface coatings or areas on which the Rock Abrasion Tool brush was particularly effective. (e) Radiometrically calibrated blue Pancam image 2P187619284lOFAJY0P2575L7M1 of the Algonquin feature, taken on Sol 690, with 3 × 3-cm area shown in Figure 20f outlined in black. (f) Radiometrically calibrated Microscopic Imager image 2M187443599 of *Iroquet* target, acquired on Sol 688 in full shadow. Arrow points to angular clasts.

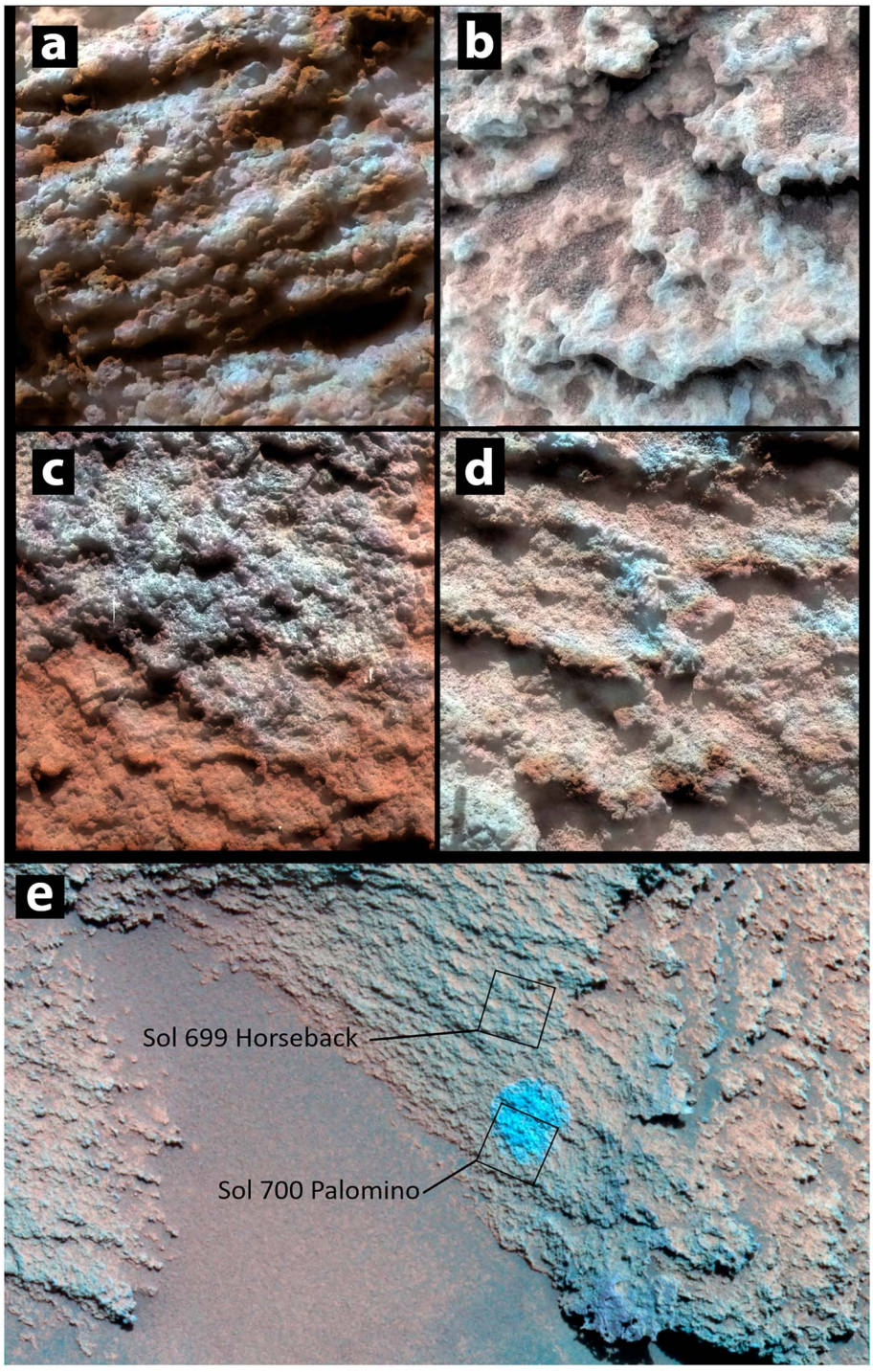

Figure 21. Merges of Pancam enhanced L257 color and Microscopic Imager images of Watchtower and Comanche class targets. Each Microscopic Imager image is ~3 cm across; see Figure 1 for locations. Both classes are stratified and exhibit a nodular texture; some targets' layers exhibit scalloped edges. (a) Paros, Larry's Lookout feature. Pancam acquired on Sol 489, Microscopic Imager image 2M169951417 acquired on Sol 491 with illumination from top. See Figure 10 for context. (b) Keystone, Methuselah feature. Pancam acquired on Sol 471, Microscopic Imager image 2M168092371 acquired on Sol 470 when target was fully shadowed. See Figure 10 for context. (c) Palomino, Comanche Spur feature. Pancam acquired on Sol 704, Microscopic Imager image 2M188509689 acquired on Sol 700 with illumination from top. Short vertical white lines are due to saturation and blooming of very bright pixels (likely specular reflections). (d) Horseback, Comanche Spur feature. Pancam acquired on Sol 704, Microscopic Imager image 2M188422137 acquired on Sol 699 with illumination from top. (e) Part of enhanced L257 color Pancam image of the Comanche Spur feature, taken on Sol 704, with areas shown in Figures 21c and 21d outlined in black.

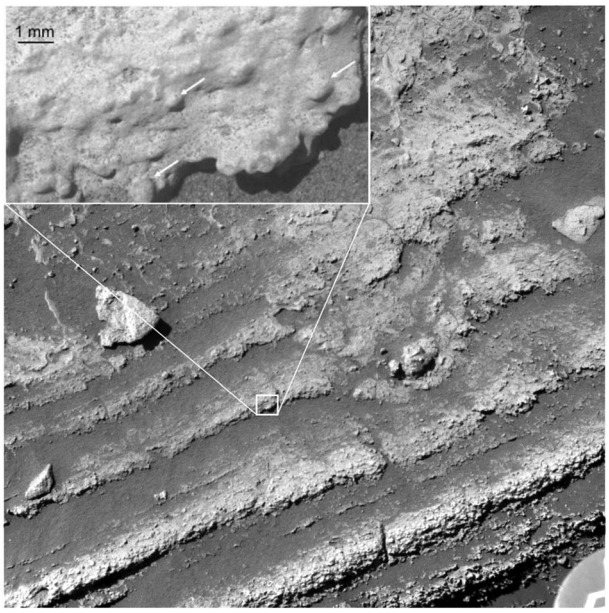

Figure 22. Radiometrically calibrated blue Pancam image 2P193032974IOFA O55P2276L7M1 of the Barnhill feature (see Figure 24c for context), taken on Sol 751, with 3 × 3-cm area shown in inset outlined in white. Note the possible bomb sag right of center. Inset is a subframe of Microscopic Imager image 2M192678831 of target *Pitcher*, acquired on Sol 747 with illumination from top. Pitcher is characterized by varied concentrations of subrounded to spheroidal 0.6- to 0.9-mm diameter grains (arrows) in a fine-grained, cemented matrix.

when brushed (Figure 23). The bumpy texture of these rocks appears to be derived from their constituent grains. Dark, rounded grains are visible in Snout and Betty Wagoner. Where layering is visible, coarser and finer-grained laminae alternate. Grain sizes are bimodal (1–5 mm and subresolution, Figure 23c). These rock targets display a continuum of grain shapes, from Riquelme (nearly all grains are spheroidal, see Halley section) to Snout (very few clearly spheroidal grains). Rocks on the west side of Home Plate (Barnhill subclass) are well sorted, consistent with eolian reworking of grains (Lewis et al., 2008). Grains in the rocks on the east side of Home Plate (Pesapallo subclass) are poorly sorted and range in size up to 3 mm in Elizabeth Emery. Such large clasts cannot be transported in saltation, leading Lewis et al. (2008) to infer a pyroclastic surge origin for Home Plate's upper unit, with possible eolian reworking of the western part of the deposit. Posey is characterized by subparallel laminae slightly more than individual grain-scale thickness of more and less-resistant material. The laminae end in rough, curvilinear rims, as shown in Figure 24a. These laminae may represent the coarse-to-fine grained sequences consistent with a tuff ring or base surge origin.

Unlike other rocks in the Barnhill class, *James Cool Papa Bell* has a massive texture with angular-edged, semicircular fracture patterns. Very small (0.1-mm diameter) dark rounded grains are randomly mixed throughout a much finer-grained matrix in Cool Papa Bell (Figure 25); these have been interpreted as either ash-sized accretionary lapilli or impact spherules (Yingst et al., 2007).

5.1.7. Fuzzy Smith Class Rock

Fuzzy Smith defines its own geochemical class (high Si and Ti) and has a massive, hackly, somewhat pitted texture with angular or rough edges. Individual grains are generally not discernable at MI resolution, though darker, irregular patches exist that may represent grains. This rock is similar in texture to those at Larry's Bench, except for the existence of voids similar in size and shape to some of those seen in Algonquin. The microtexture and morphology of this rock is less diagnostic of origin than the coarser-grained clastic types, so interpretation of origin is uncertain. Chemical data suggest that Fuzzy Smith is the product of hydrothermal alteration in a volcanic environment.

5.1.8. Elizabeth Mahon and Good Question Class Rocks

Rock targets Elizabeth Mahon, *Nancy Warren*, *Norma Luker*, *Innocent Bystander*, and Good Question contain coarse (0.3–1.25 mm), possibly rounded grains in a copious cementing agent. The cementing agent has a porous texture and appears pitted or sponge like. Rocks in these classes appear brighter than other rocks, with nodules and stalks forming a digitate texture (Figure 26). They have a granular texture with dark, rounded to subrounded grains in places embedded in angular-edged ridges, which may represent layers of more resistant material. An ~1-cm-long piece of Elizabeth Mahon appears to have recently broken away from the rest of the rock, exposing a more porous interior that is probably representative of primary textures. Similarly, the fresh surfaces of Innocent Bystander (see supporting information) and Norma Luker (broken open by the rover wheels) have a porous texture that may be the result of incomplete cementation (Ruff et al., 2011). Similar textures are observed at an active hot spring in Chile (Ruff & Farmer, 2016), so eolian abrasion may not have been involved in creating the morphology seen at Elizabeth Mahon.

These digitate, opaline silica structures were interpreted to have formed under hydrothermal conditions, perhaps due to fumarolic leaching of a basaltic substrate (Squyres et al., 2008), and have been hypothesized to be microstromatolites based on their similarities to microbially-mediated samples from Chile (Ruff & Farmer, 2016). The rocks in both of these classes are enriched in Si (Ming et al., 2008). Based on their texture, MI targets *Puenta Arenas* and *Darlene Mickelson* were also interpreted as silica-rich rocks, although they were not investigated by the APXS (Ruff et al., 2011). These rocks are interpreted as volcaniclastic material that has been cemented by silica, as APXS, Mini-TES, and Pancam observations of these rocks indicate that they are silica rich (Squyres et al., 2008). However, opaline silica was not detected in Good Question, the lone example of its geochemical class (Ming et al., 2008).

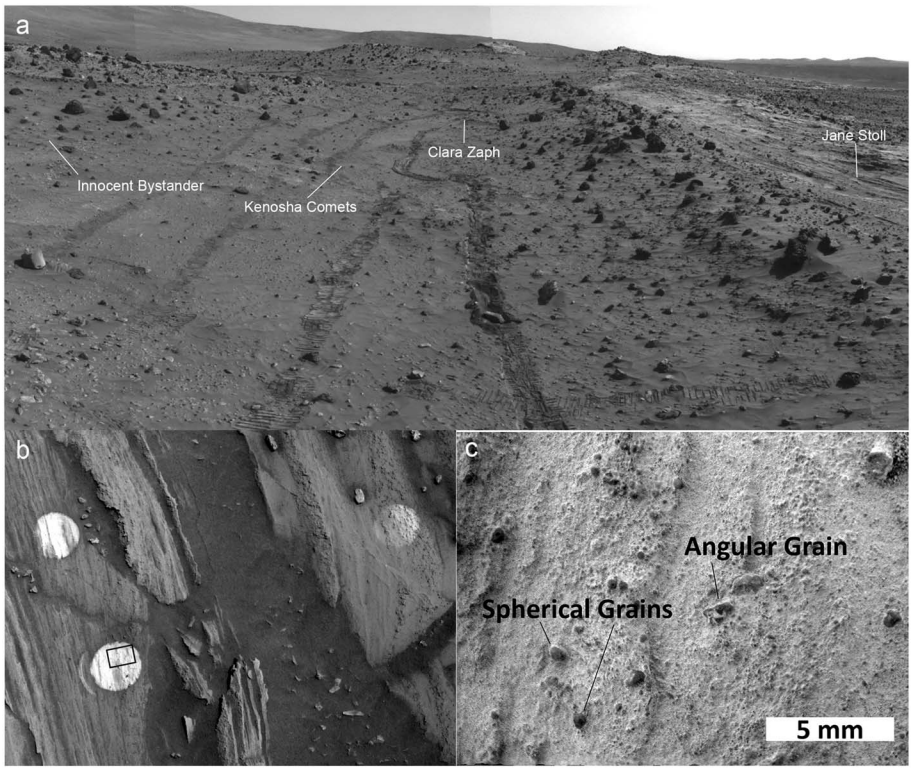

Figure 23. (a) Navcam mosaic of *Silica Valley* feature, acquired on Sol 1132 looking ~SSW. Rover tracks span 1.2 m. (b) Radiometrically calibrated blue Pancam image 2P234663600IOFATF3P2561L7M1, taken on Sol 1220, with area shown in Figure 23c outlined in black. Areas that have been brushed by the RAT (about 5-cm diameter) appear bright in this image. (c) Brushed target Jane Stoll, showing the variation in embedded grain shapes. Brushed spheroidal grains in this target are darker; some have a grainy texture while others have a shiny luster. Part of focal merge of radiometrically calibrated Microscopic Imager images acquired on Sol 1217 when target was fully shadowed.

5.1.9. Halley Class Rocks

These hematite-rich clastic rocks southeast of Home Plate (Figure 1) show a variety of microtextures. Halley, the lone member of the Halley subclass (Ming et al., 2008), is composed of poorly sorted dark subangular grains in a brighter matrix. Rocks of the *Graham Land* subclass contain variable concentrations of very coarse, rounded grains. Well-sorted, round grains dominate the *King George Island* target (Arvidson et al., 2008) but are less abundant in *Riquelme*, which has laminae 1–3 mm in thickness (Figure 27). Spheroidal grains that have been brushed clean by the RAT are darker and have either a grainy or shiny luster. These spheroidal grains are likely hematitic concretions that have been reworked by winds into laminated deposits, consistent with chemical and mineralogic data.

5.1.10. Montalva Class Rock

The rock Montalva, near Halley (Figure 1), contains possible grains of indeterminate shape surrounded by a cementing agent and has a texture similar to that of nearby Troll targets (Figure 31). Montalva defines its own geochemical class of high K, hematite-rich rock (Ming et al., 2008). MI and APXS data both indicate that this rock has been highly altered.

5.1.11. Everett Class Rocks

Everett-class high-Mg, magnetite-rich targets Everett and *Slide* (Ming et al., 2008), found on the east side of Home Plate (Figure 1), contain poorly sorted subrounded to angular grains in a clast-supported matrix (Figure 28, Ruff et al., 2011). These rocks have a clast size and shape distribution that is similar to Comanche.

These well-cemented clastic rocks are interpreted to include accretionary lapilli in varying proportions and to have been deposited in a wet volcanic environment and subsequently lithified in part by the cementing agent. Laminae seen in these rocks may be indicative of eruptive pulses.

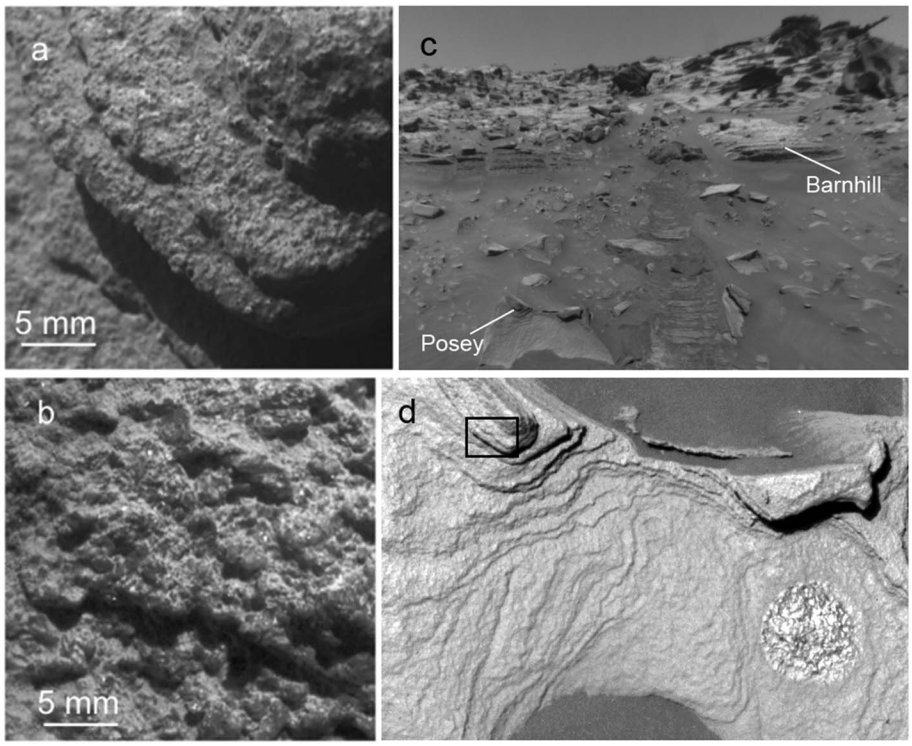

Figure 24. (a) Subframe of Microscopic Imager image 2M193210336 of target *Snout*, acquired on Sol 753 with illumination from top, showing texture characterized by a mix of larger subangular to spheroidal (1–5 mm) grains in a finer-grained, clast-supported matrix. The size distribution and shape of constituent grains is like that of the target Palomino on Comanche Spur (b, subframe from Microscopic Imager image 2M188508626 acquired on Sol 700 with illumination from top; see Figure 21e for context). (c) Part of Front Hazcam image 2F193038085RSLAOA0P1214L0MZ acquired on Sol 751, showing NW side of Home Plate and locations of Posey and Barnhill features. James *Cool Papa* Bell feature is just over the horizon in this view. (d) Radiometrically calibrated blue Pancam subframe 2P193214728IOFAOA0P2583L7M1 of the Posey feature, taken on Sol 753, with area shown in Figure 24a outlined in black.

5.1.12. Torquas Class Rock

Like King George Island, the rock Torquas, located east of Home Plate (Figure 1), contains abundant well-sorted, millimeter-size rounded sand grains (Figure 29) but is enriched in magnetite rather than hematite (Morris et al., 2006, 2008). Again, the clast-supported texture suggests reworking of sand grains (perhaps impact spherules) to form this rock.

5.1.13. Unclassified Rocks

Ming et al. (2008) classified rocks observed through Sol 1368. Rocks observed by the MI after then include *Chanute* (Sols 1409–1434, very fine grained), *Freeman* (Sol 1452, subrounded dark fine sand grains in finer-grained matrix, shiny luster), *Wendell Pruitt* (Sol 1486, very fine grained), *Stapledon* (Sol 1796, similar to other silica-rich rocks), *Olive Pit* (fine-grained centimeter-size pebble in soil, Sol 1979), and *Stratius* (Sol 2044, dust covered, texture not evident). MI images of Stapledon (Figure 30) show textures similar to Innocent Bystander (Ruff et al., 2011); this and the APXS measurement of high silica content imply that it is a member of the Elizabeth Mahon class.

5.1.14. Comparison of Home Plate Rocks With Algonquin-Class Rocks

There are similarities between the microtexture of ultramafic Algonquin class rocks on the SE flank of Husband Hill and that of the layered basaltic materials of Home Plate (Barnhill, Halley, Torquas, and Everett classes). The key characteristics of the textural links between classes are as follows.

1. Grain morphology and appearance are characterized by coarse to very coarse rounded grains that are sometimes mixed with more angular grains. The most well-rounded grains are likely accretionary lapilli (Figure 31), which would require the presence of sufficient water during eruption for ash to nucleate.

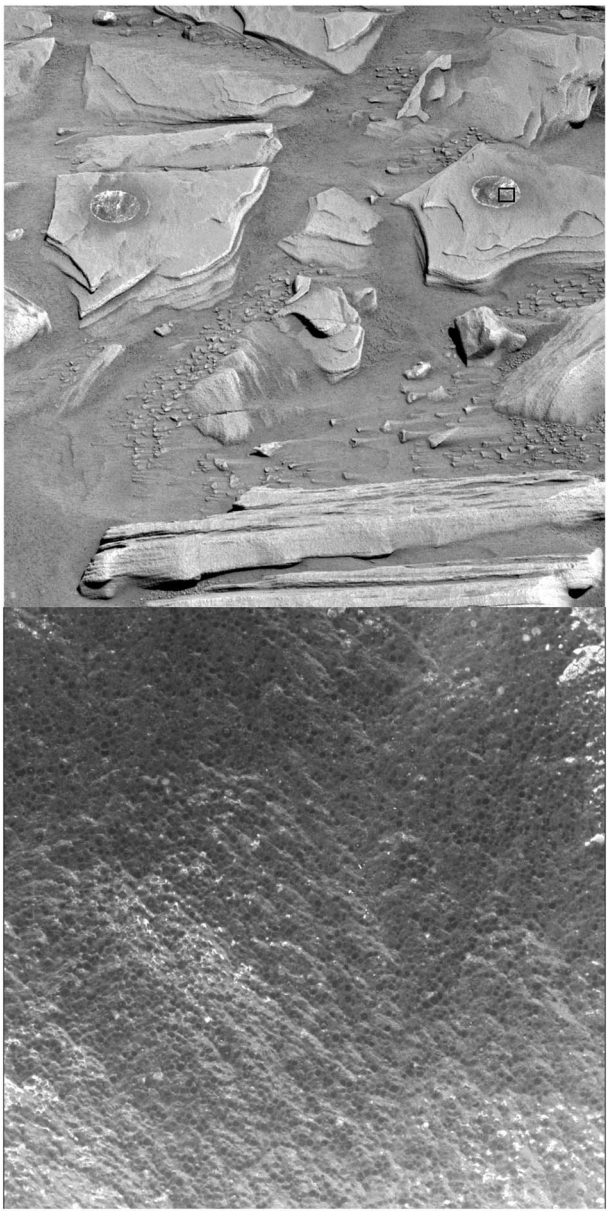

Figure 25. (top) Blue Pancam image 2P194187730EFFAODUP2589L7M1 of the James "Cool Papa" Bell feature, taken on Sol 764, with area shown below outlined in black. (bottom) Microscopic Imager image 2M19400729 of target "Crawfords" acquired on Sol 763 when target was fully shadowed, demonstrating massive, fine-grained texture. This rock has very small (0.1 mm diameter) dark spheroidal grains interspersed abundantly throughout.

2. The rocks are composed of clasts with similar grain size. Impact or volcanic activity could produce the wide range of grain sizes observed and would be consistent with production of angular grains.
3. Clast-supported textures dominate in nearly all cases (Table 3). The presence of a cementing/welding agent is evident in several targets, indicating either reworking of in situ deposits or cementation of grains shortly after deposition, possibly by palagonitization or nano-phase Fe-oxide alteration.

Microtextural evidence suggests that similar processes resulted in the deposition of basaltic Home Plate and ultramafic Algonquin rocks. Both classes are volcaniclastic and likely saw interaction with fluids during or after emplacement. If there is a genetic relationship between these classes, then the Home Plate structure may represent part of a larger geologic unit of hydrovolcanic origin (Yingst et al., 2007). Detailed geologic mapping may help determine whether this is the case.

An alternate interpretation of the well-rounded grains in Home Plate rocks is that they are impact spherules. Impact spherules on Earth have a glassy texture and have a wide distribution of mostly sand sizes. It is expected that larger spherules would be more likely to be disrupted upon impact, and that smaller spherules would occur as more angular fragments. Terrestrial impact spherules tend to have lower water content than volcaniclastics but contain Fe^{2+} and higher amounts of platinum-group elements. Most of the rocks at and near Home Plate are enriched in Ni relative to the Adirondack class plain basalts, but the Ni enrichments are correlated with Zn, suggesting that both elements were added by a single, possibly hydrothermal process (Ming et al., 2008). The enrichment and association of halogen and other volatile elements in Barnhill class rocks also suggests hydrothermal alteration (Schmidt et al., 2008). The rounded grains in targets such as Barnhill, Riquelme, and Torquas have sizes (0.5–1.0 mm) consistent with an origin as impact spherules. However, millimeter-size grains are not evenly and broadly distributed around Home Plate (which is only about 80-m diameter) as would be expected if they were emplaced by impact and not significantly reworked. Rocks with textures that are somewhat similar (Comanche and Barnhill share several characteristics) do not have the high concentration of spheroidal grains seen in and around Home Plate. Unaltered impact spherules have a glassy luster while lapilli are dull aggregates of microscopic ash fragments, but dust coatings make determination of luster difficult for these rocks. However, for brushed targets, the lack of reflective surfaces suggests that they are not glassy. Finer grains are not observed, probably because the ash grains that formed them are finer than 0.1 mm, and therefore cannot be resolved by the MI. Because the spheroidal grains are highly localized, we conclude that they were emplaced by volcanic rather than impact processes.

5.2. Soil Observations

The MI was used to image various soil targets in Gusev crater (Table 4) to help constrain modes of origin, of weathering, and transport of Martian fines. In many instances, microscopic imaging of soils supported assessments of their physical properties, in particular the degree of induration and deformation behavior under load (Herkenhoff, Golombek, et al., 2008). The term Martian soil is used here to denote any loose, unconsolidated materials that can be distinguished from rocks, bedrock, or strongly cohesive sediments. No implication of the presence or absence of organic materials or living matter is intended.

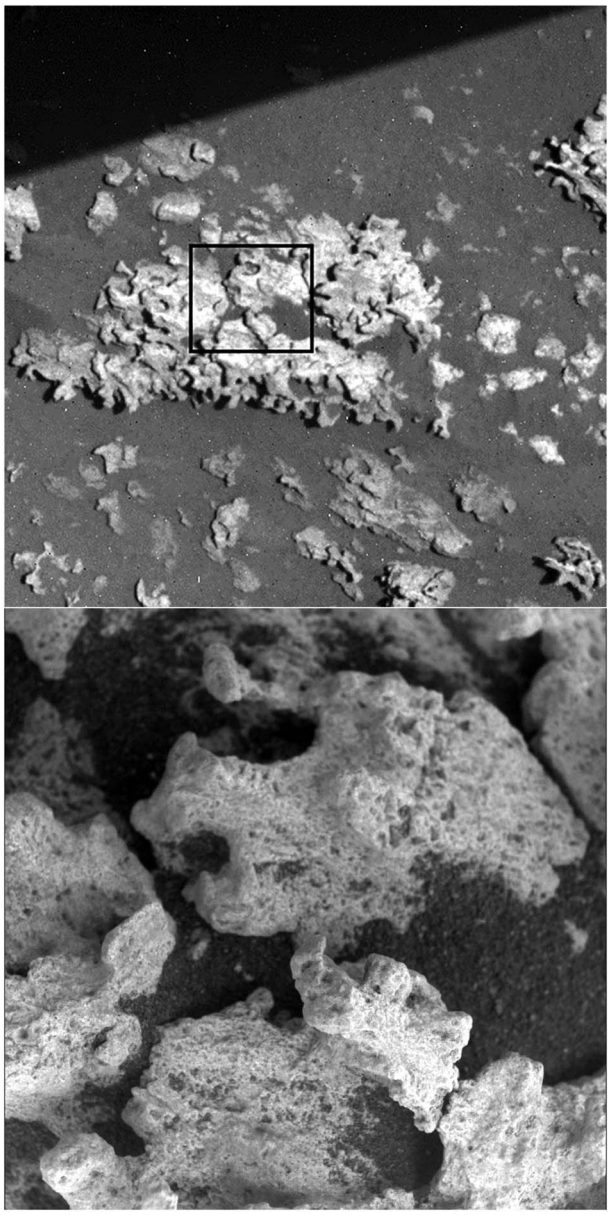

Figure 26. (top) Blue Pancam subframe 2P229344608ESFAS__P2582L7M1 of the digitate *Clara Zaph* feature, taken on Sol 1160 with shadow at upper left and 3 × 3-cm area shown below outlined in black. For context, see Figure 23a. (bottom) Radiometrically calibrated MI image 2M229074932 of Elizabeth Mahon, taken on Sol 1157 when target was in shadow, showing pitted clastic texture.

5.2.1. Eolian Influences on Soil Textures

Multiple studies of soil grain characteristics using *Spirit* MI data have been published (Cabrol et al., 2008, 2014; Greeley et al., 2008; Karunatillake et al., 2010, 2014; Yingst et al., 2008, 2010). Subsurface soils were exposed in wheel trenches and other wheel disturbances, but the number of such observations was limited. Nevertheless, differences between surface and subsurface soils were always seen at these sites. Surficial materials commonly show more evidence for eolian influences (particularly sorting), compared with subsurface soils. McGlynn et al. (2011) examined MI images of soils acquired through Sol 1360 and found that subsurface soils resemble crushed sediment analogs, indicating impact comminution. They concluded that the observed soil properties are the result of impact disruption of altered basalt, followed by eolian reworking of the near-surface layer. Incomplete sorting of sand by saltation and concentration of coarser grains by creep has produced bimodal mixed soils (McGlynn et al., 2011). Cabrol et al. (2014) measured about 20,000 sedimentary grains in 77 MI images, of which nearly 8,000 well-exposed grains 0.1–2 mm across in 51 images were analyzed statistically. They identified three classes of geological processes from the sorting and skewness of the grain size-frequency distributions: (1) modern eolian saltation, sorting, and deposition of fine to medium sands, (2) limited transport/reworking of more angular, recently eroded coarse sands, and (3) eolian saltation-driven impact creep of well rounded, coarse ripple armor (currently inactive). These results indicate that eolian processes are primarily responsible for the observed distribution of sizes and shapes of sand grains along *Spirit*'s traverse (Cabrol et al., 2014).

The presence of $<$4-μm air fall dust particles was expected at the surface of Gusev crater, based on prelanding analysis of albedo and thermal inertia data obtained from orbit (Golombek et al., 2003). Wind tunnel experiments have shown that smooth mantles of dust-sized grains are more difficult for wind to mobilize than sand-sized grains, due to the increasing influence of interparticle cohesion at the finest particle sizes (Iversen & White, 1982). In situ MI views during the initial stages of Spirit's traverse confirmed the presence of dust at the surface but in an unexpected way: Air fall dust was present as easily resolved sand-sized aggregates (Herkenhoff, Squyres, et al., 2004). Dust aggregates have irregular shapes, including fragile, filamentary textures. Larger examples of dust aggregates were found more commonly in areas protected from the wind, while more exposed surfaces (such as sloping rock faces extending upward into the atmospheric boundary layer) generally hosted fewer obvious dust aggregates that were also smaller and harder to resolve (Sullivan et al., 2008). Dust aggregates were seen also during MI monitoring of the rover's solar panel surface (Vaughan et al., 2010; see section 5.3.2). The low density and fragility of dust aggregates was demonstrated by compression and remolding by ~1 N touches of the arm-mounted Mössbauer contact plate (see figures in Herkenhoff, Squyres, et al., 2004, Herkenhoff, Golombek, et al., 2008 for examples). Dust aggregates have the drag cross section of sand grains but a substantially lower overall density; therefore, they are easier for the wind to mobilize than ordinary silicate-density sand grains. The raising of dust on Mars, including dust devil activity, therefore does not require winds strong enough to first saltate silicate-density, sand-sized grains as a triggering event (Greeley et al., 2010; Sullivan et al., 2008).

A strong wind event between Sols 417 and 421 cleared much of the transient dust mantle from *Spirit*'s landing site (see Figures 1 and 56 of Sullivan et al. (2008) for orbital views). This increased the information available in MI images of rocks and soils. In particular, eolian bedforms, drifts, and soil surfaces composed of

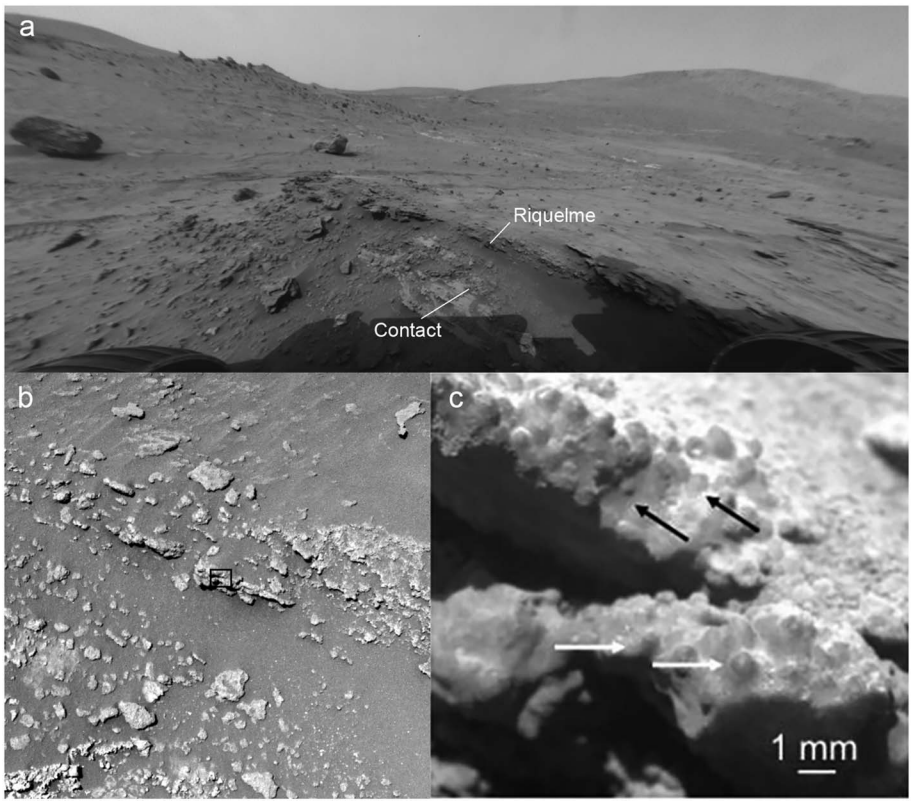

Figure 27. (a) Part of Sol 1069 Front Hazcam image 2F221268565RSLASCGP1214L0MZ, looking east. (b) Blue Pancam subframe 2P222242521ESFASCGP2537L7M1 of the *Troll* feature, taken on Sol 1080, with area shown in Figure 27c outlined in black. (c) Subframe of Microscopic Imager image 2M222243402, acquired on Sol 1080 with illumination from top. Target Riquelme shows varied concentrations of subrounded to spheroidal 0.6–0.9 mm diameter grains (white arrows) in a fine-grained matrix. Laminae are no more than four grains thick (black arrows).

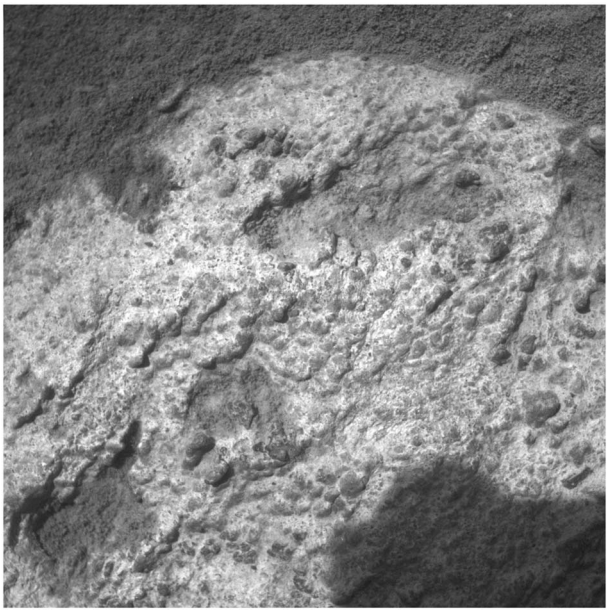

Figure 28. Radiometrically calibrated Microscopic Imager image 2M230768863IFFAT48P2956M2F1 of Slide target, acquired on Sol 1176 with illumination from upper left. Field of view is 3 × 3 cm; darker area at lower right is shadow of Instrument Deployment Device.

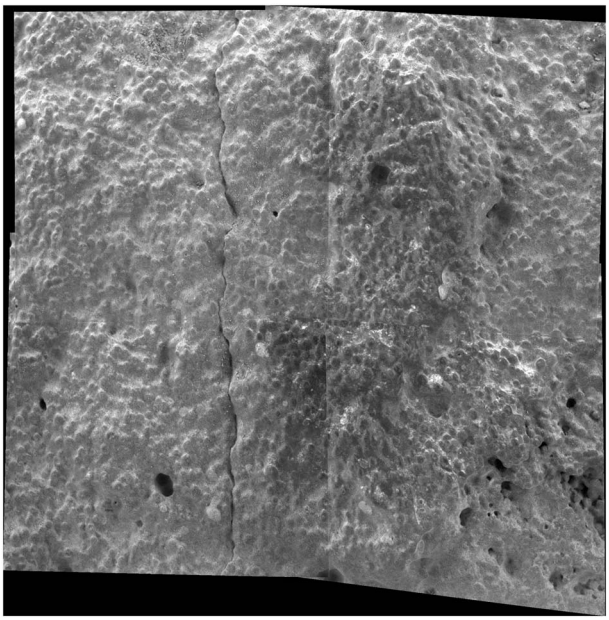

Figure 29. Mosaic of Microscopic Imager images of Torquas, acquired on Sol 1143 after Rock Abrasion Tool brushing when the scene was fully shadowed. Field of view is about 5 × 5 cm.

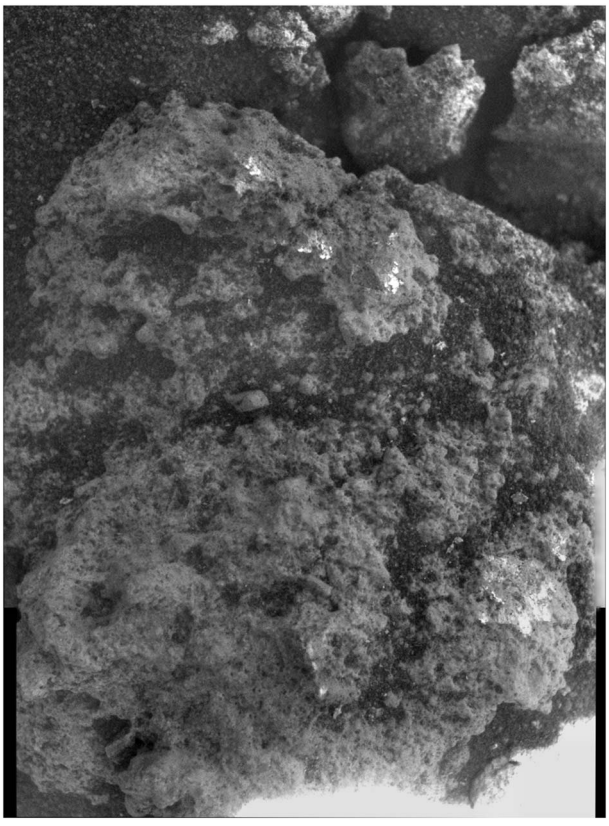

Figure 30. Mosaic of Microscopic Imager images of Stapledon, acquired on Sol 1796 when target was shadowed except at lower right corner. Scene is ~3 cm across, showing dark sand partly covering the rough rock surface.

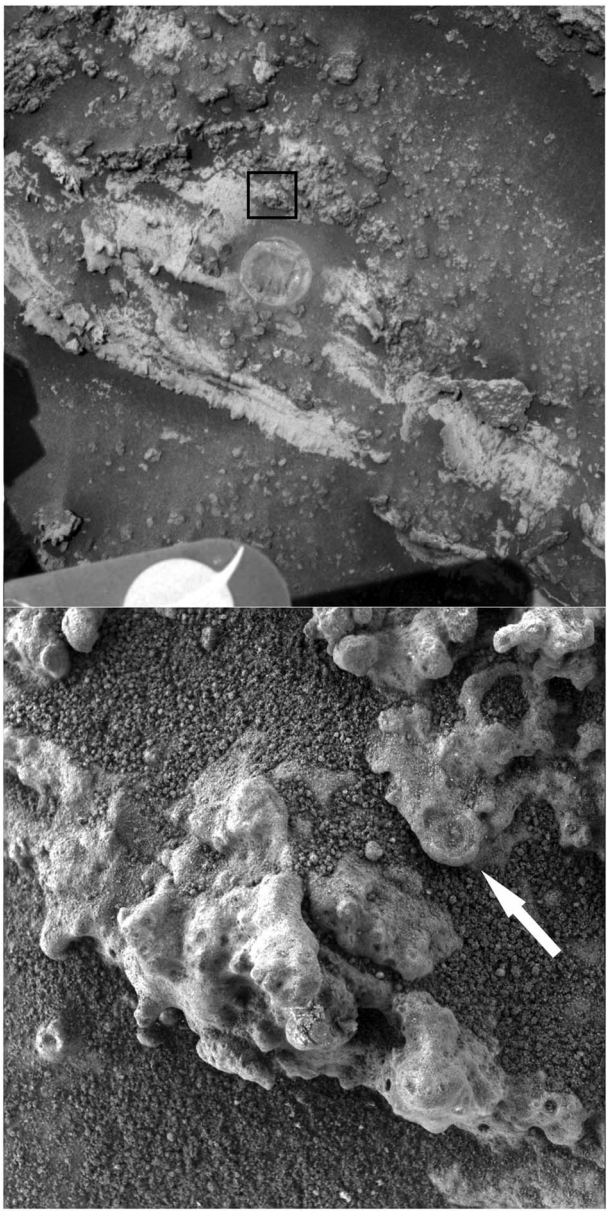

Figure 31. (top) Red Pancam image 2P221620223EFFASCGP2534L2M1 of the Troll feature, taken on Sol 1073, with 3 × 3-cm area shown below outlined in black. The Rock Abrasion Tool-brushed *Montalva* target is visible just above and left of center. For context, see Figure 27a. (bottom) Focal merge of Microscopic Imager images of Halley class target *Contact* acquired on Sol 1085 in full shadow. Arrow indicates potentially accretionary (volcanic or impact generated) lapillus, showing a core with surrounding layers. Target has nodular texture, with nodules ranging from 0.9 to ~4.0 mm across. Grains at ends of nodules are angular to subrounded. Subangular to rounded, fine to medium sand-sized particles cover low areas.

grains finer than 500 μm became more readily identifiable and interpretable, because these surfaces were less obscured by thin, transient mantles of sand-sized aggregates of airfall dust.

Lightly crusted soils with relatively dark, well-sorted ~200- to 300-μm surface grains were encountered in several places around the Columbia Hills, including near Larry's Lookout (MI observations on Sols 460 and 494), and at *El Dorado*, a 170-m-wide field of large, dark ripples (Figure 1). Crustiness of the surface in these locations is apparent only from morphologies of soil disturbances; the appearance of undisturbed surface grains in these locations otherwise would have been ambiguous regarding surface cohesion. In each of these cases, soils underneath the weak surface crusts were poorly sorted ≤300-μm particles,

Table 4
Summary of Gusev Soils at MI Resolution

Sol	Feature/target name	Soil type	Soil type and description
013	/First Soil1Final	Unstructured	Very fine grained soil; individual particles are below MI resolution.
015	/First Soil1Final	Unstructured	Similar to 013.
039	Squiggle/Sideslope2	Bedform	Disturbed (MB contact plate) - Elongated to round granules and finer sand particles.
041	Arena/Crest	Bedform	Lower density of granules, some platy with finer sand particles.
041	Arena/Trough	Bedform	Lower density of granules, some platy with finer sand particles.
043	Mimi Tracks/2	Unstructured	Disturbed (MB contact plate) - Granules pressed into very fine grained material.
044	Ramp Flats/1	Composite	Very fine grained material embedding rounded to angular pebbles.
045	Angel Flats/Halo 01	Bedform	Sand particles, fine to granule size. Higher albedo, unresolved material fills intergranular space.
046	Grande Flats/Trout 1	Composite	Comparable to 044.
048	Road Cut/Wall 1	Vert. exposure.	Comparable to 013–015 but with larger clumps of material and localized granules.
048	Road Cut/Floor	Unstructured	Similar in texture to 013–015, with soil clumps and granules. Aggregates are present and soil appears possibly cemented and brittle in places.
049	Road Cut/Dividing Line	Vert. exposure	Similar to 048 Wall 1. Sand size particles present.
050	Road Cut/Mason Dixon	Vert. exposure	Disturbed soil - Material under MB plate pressure behaves as flour. Small particle aggregates below MI resolution and sand present.
051	Split Rock Flats 2	Unstructured	Similar to 013–015.
052	Sugar/SugarT 1	Bedform	Similar to 039. Dusty granules. Particles below MI resolution form aggregates.
053	Wrinkle Ridge/1	Composite	Comparable to 044.
063	Plank/Nail	Unstructured	Very fine-grained material; fine sand present. Gray and high albedo.
065	Sugar Loaf/Escarpment1	Unstructured	Similar to 013–015 before pressure from MB plate.
065	Sugar Loaf/Flats 1	Unstructured	Very fine grained soil, mostly below MI resolution. Behaves like flour under MB contact plate pressure.
068	Deserts/Gobi1	Composite	Similar to 044 but larger fraction of soil below MI resolution.
071	Deserts/Window	Composite	Crusty, cemented, and clean-cut fracture in soil. Similar to Road Cut (049).
073	Bear Paw/Polar	Bedform	Similar to 039, 045. Granules and fine, dust-like particles grouped in brighter aggregates.
073	Bear Paw/Spectacle2	Bedform	Scuffed, exposes dust free, darker, finer (fine sand) material.
073	Bear Paw/Kodiak	Bedform	Scuffed, mixed material. Exposes dust free, bright and dark granules, rounded and elongated, sitting on a bed of dark and bright sand-size particles.
075	Patio/Soil 2	Composite	Similar to 068.
077	Mazatzal Flats/Soil 1	Unstructured	Majority of fine to very fine sand. Brighter, thinner particles grouped in aggregates occupy intergrain space (dust?).
078	Mazatzal/Arizona	Rock	Particle deposition and erosion on rock resembles 013–015 and other similar soils, supporting the hypothesis of consolidated dust deposits.
105	Bitterroot Flats/Flats 1	Composite	Similar to 044 with smaller pebbles.
110	Waffle Flats/Soil 1	Composite	Similar to 105.
113	Big Hole/Mayfly	Composite	Similar to 044.
114, 116	Big Hole/Stonefly	Trench	Similarities with Road Cut (049). Possible layering. Particles below resolution and very fine sand represent the largest fraction. Aggregates and granules are present. Top layer has higher albedo than exposed trench material.
122	Cutthroat/Owens	Unstructured	Crusty, fractured, unresolved material with granules and coarser sand in cracks. Soil detaches in flakes of higher albedo compared to rest of soil.
140	The Boroughs/Williamsburgh	Trench	Comparable to 114, 116.
141	The Boroughs/Mills3	Unstructured	Very fine sand and unresolved material forming aggregates that in places can reach up to millimeter size. Mixture of bright and dark material.
158	Shredded/Dark4	Unstructured	Disturbed (MB contact plate). Typical unstructured soil (013–015). Behaves like flour under compaction.
160	End of the Rainbow/Dantes Peak	Rock, soil	

Table 4 *(continued)*

Sol	Feature/target name	Soil type	Soil type and description
			Deposit on rock near West Spur. Fine sand material, clear of dust, suggesting drifting material passing over rock. Very fine-grained material in rock interstices consistent with dust and dust aggregates.
164	End of Rainbow/Goldfin1	Bedform	Drift material made of fine to medium sand. Abundance of unresolved particles between grains, possibly dust.
166	Fort Knox/Goldstaub	Unstructured	Very fine to fine individual sand particles of low albedo. Patch of soil made of very fine particles has higher albedo.
167	Goldfinger/OddJob	Unstructured	Composed of fine to medium sand with exposure of brighter material of finer texture. Under pressure of MB contact plate, sand particles appear to sink, suggesting the presence of an underlying finer, brighter material.
177	String of Pearls/Pearl1	Unstructured	Very dusty soil composed of particles ranging from below resolution to medium sand. Overall gray albedo. Isolated bright angular fragments detached from local rock.
181	CookieCutter/Shortbread1	Unstructured	Individual particles are below MI resolution. They are grouped into aggregates and clumps from 100 s of micrometer to millimeter in size. Albedo ranges from low to high. Clumps can show clear-cut fractures suggesting cohesiveness.
227	Frio/Kilamey Flats	Composite	Soil component includes typical unstructured soil characteristics (013–015) and rounded pebbles.
235	Ebenezer/Fritz	Unstructured	Soil behaves like flour under pressure of MB contact plate. MB plate sinks deeply. Outside the plate area, material collects in aggregates and clumps of 100 s of micrometer in size. The wall created by the MB contact plate is vertical suggesting material cohesiveness.
240	Tikal Area/GreenEyes	Unstructured	Similar to 235 but outside MB contact plate area. Soil shows characteristics comparable to 013–015 and other similar soils.
258	Tikal Area/GreenEyes	Unstructured	Undisturbed area and area disturbed by MB contact plate show typical characteristics of unstructured soil (013–015).
259	Conjunction Junction/Disturbance	Unstructured	Disturbed (MB contact plate) - MB contact plate sinks deeply into flour-like material. Plate footprint is heterogeneous.
279, 281	TakeABreak/Coffee	Composite	Rocky soil, with pebbles dominant. Covered by unresolved dark material. Material is crusty in places. Aggregates are present; some have higher albedo.
314	Yams/Tofurkey	Unstructured	Disturbed by MB contact plate. Comparable to 122 but without granules.
341	Penny/Ds1	Unstructured	Disturbed, soil includes very fine to fine material below MI resolution, fine to coarse sand. Fine to medium sand has a lower albedo than finer material and coarser sand. Material under compaction of MB plate is made of fine sand with particles at the limit of MI resolution. Localized patch of unresolved, very bright and flour-like material.
372	Peace/Mosaic	Composite	Very dusty soil with particles ranging from below MI resolution to coarse sand. Overall gray albedo. Fills rock cracks.
373	Peace/Equality	Bedform	Local drift material on top of outcropping rock. Well-sorted sample of medium sand with finer component, including below MI resolution. Overall gray albedo.
399	Pasadena/Marengo	Composite	Disturbed soil - A few rounded pebbles on soil reminiscent of the Borough's trench top layer in structure and albedo.
400	Pasadena/Paso Robles	Unstructured	Disturbed soil (MB contact plate) - Gray soil composed of particles at the limit of MI resolution or below grouped in clumps. Possibly some granules or very coarse sand size particles.
426	Paso Robles 2/Big Clod	Composite	Disturbed soil (MB contact plate) - Angular to subrounded pebbles embedded in dark material below MI resolution. Pebble albedo suggests that they are fragments of local rocks. Fine sand present.
426	Paso Robles 2/Bitty Clod	Composite	Very low albedo, unresolved particles. Top layer is made of clumps of cemented particles at and below MI resolution with low and high albedo. Very coarse sand to granules, many very angular. Unclear whether they are actual clasts or detached fragments of brittle crust.
428	Paso Robles 2/Paso Light1	Composite	

Table 4 *(continued)*

Sol	Feature/target name	Soil type	Soil type and description
			Disturbed soil - Many rounded to subangular pebbles. The soil has a fine sand component. The material under the pressure of the MB contact plate is similar to 341.
431	Paso Roble2/Paso Dark1	Composite	The main component is a dark fine sand. Presence of medium sand. Angular pebble-size and smaller fragments are consistent with fragments of local bright outcropping rocks.
457	Crumble/Chunky	Composite	Fine to medium sand with angular rock fragments ranging in size from 100 s μm to centimeter.
457	Crumble/Almonds	Composite	Similar to previous but with higher density of pebbles or larger size.
460	Crumble/Cashew	Composite	Sandy drift material (fine to medium size grains, subangular to subrounded) and large angular to subrounded clasts. The overall albedo of the drift is gray with bright sand particles. Two isolated spherules (300 and 600 μm).
477	Jibsheet/Hoof	Bedform	Low albedo, fine to medium sand particles with an isolated bright angular clast. High albedo, very round to circular, medium to coarse sand-size particles are interspersed with the drift material. No dust visible.
480	Jibsheet/Bell	Composite	Disturbed soil (MB contact plate) - Drift material mixed with local soil: very fine particles below and at MI resolution up to medium sand. Isolated bright granules and rock fragments. Albedo ranges from intermediate to high. MB footprint is incomplete. Dark fine sand particles pressed into finer high albedo material.
481	Jibsheet/Reef	Bedform	Low albedo fine to medium sand surrounding outcropping bright rocks. No dust.
494	Slump/Hitting	Unstructured	Consolidated crust detaching in fragments with sharp edges and clean-cut fractures. The top layer is formed of homogeneous fine gray sand.
494	Slump/Wallstreet	Unstructured	Similar to previous soil but angular fragments are dominant and larger. Dark fine sand and unresolved material appear to be deposited on top of the bright fragments rather than part of the crust composition. Crust is composed of unresolved material.
499	Pequod/Doubloon	Composite	Lag of platy round to angular granules and bright, coarse sand on top of fine to medium dark sand.
588	Lambert/Whymper	Unstructured	Unresolved particles. Soil behaves like flour under pressure of MB contact plate with albedo change. Particles form aggregates that can reach up to a few 100 s of micrometer in size.
607 612	Cliffhanger/HangTwo	Composite	Coarse to very coarse angular sand up to granule size. Distribution and shape are reminiscent of 499 (Doubloon). Grains are packed against each other and dusty. Unresolved dust particles form aggregates that fill intergranular spaces.
611	LandsEnd/Cliffhanger	Composite	Similar material as previous but pressed under MB contact plate. When pressed, grains sink in dark, unresolved material and maintain their structure.
707	El Dorado/Gallant Knight	Bedform	Fine to medium size sand with albedo ranging from dark to bright. Bright, very round to round sand size particles, some elongated, are interspersed in the deposit. Bright, small (100 s of micrometer) fragment present.
709	El DoradoScuff/Shadow	Bedform	Homogeneous, well-sorted medium sand dune field. Grains are packed against each other under pressure of MB contact plate with little lost space.
710	El Dorado/Edgar	Bedform	Fine sand of dark to bright albedo.
812	Enderbyland/Mawson	Composite	Rounded to subangular bright granules over darker fine to medium sand. A significant fraction of these particles is very rounded while other particles are angular. They also have distinct albedo, consistent with two distinct populations and/or alteration processes. A fraction of the soil is composed of particles at or below MI resolution with an albedo higher than the dark sand. Very little dust.
822	Enderbyland/Progress	Bedform	Veneer of local drift material on top of unresolved underlying soil particles. Sand size ranges from fine to medium, with gray albedo.

Table 4 *(continued)*

Sol	Feature/target name	Soil type	Soil type and description
			Shape varies from angular to rounded. Some particles are very rounded (spherule like).
830, 842, 858	Enderbyland/Progress	Unstructured	Disturbed soil (RAT Brush) - Relatively deep brush impression in a very fine-grained soil. Individual particles are below MI resolution and form cohesive aggregates to clumps. The walls of the excavation are vertical with no collapse. Very high albedo in places.
861, 880	Enderbyland/Brunt	Unstructured	Dark soil composed of particles mostly below, or at, MI resolution. Isolated dark, rounded, fine to medium sand and bright fragments detached from local rocks.
908, 1008	Enderbyland/Palmer	Bedform	Ripple composed of well sorted, rounded fine to medium sand. Other material includes fine sand and unresolved particles, possibly part of the underlying soil.
913	Enderbyland/Palmer2	Bedform	Same as previous but with more underlying soil exposed. Presence of bright granules ranging from subangular to very rounded. A 3.5 × 1-mm crack with vertical walls suggests that the underlying soil has a thin, cohesive crust component.
930	Enderbyland/Halley Brunt 2	Composite	Soil composed of underlying unstructured soil with veneers of sand particles up to medium size, rounded, likely from local drifts and ripples.
1007	Enderbyland/Clasts	Clast, soil	Bright clast embedded in composite soil made of dark sand (fine to medium size), rounded to angular. Presence of medium sand size spherules of higher albedo and bright rock fragments.
1008	Enderbyland/Mawson	Composite	(See 812) Rounded to subangular bright granules over darker fine to medium sand. A significant fraction of these particles is very rounded while other particles are angular. Material pressed under the MB plate produces a smooth-looking contact zone composed of individual particles below MI resolution. Where pressed, large granules sink into the soil. Sinkage areas have vertical walls with no collapse, showing cohesiveness. Little dust.
1013	Enderbyland/Berkner Island	Composite	(Disturbed, MB contact plate) - Most of the soil presents typical characteristics of unstructured soil (i.e., behaves like flour when pressed, particles below MI resolution). Granules, pebbles, and soil clumps present. The soil is dual tone, with bright material in the disturbed area and surrounding dark material.
1017	Enderbyland/Bear Island	Unstructured	(Disturbed, MB contact plate) - Unresolved particles; behaves like flour when pressed. Walls of compacted area are vertical with no collapse, showing cohesiveness. Dual-tone soil, similar to 1013.
1027, 1031	Enderbyland/King George Island	Outcrop	A plausible source, as are similar outcrops, of spherical particles observed on the ground in the Home Plate region. Interpreted as lapilli. Grain size ranges from fine sand to granules.
1034	Enderbyland/Clarence	Bedform	Similar to 908.
1034	Enderbyland/Deception	Unstructured	Crusty soil formed of unresolved particles detaching in flakes and clumps with clean-cut fractures showing soil cohesiveness. Aggregates and fine sand particles are present.
1035	Enderbyland/King George Offset	Outcrop	Similar to 1027 but with larger grains overall.
1085	Troll/Londonderry	Bedform	Dune composed of well-rounded fine to medium sand. Albedo is dark gray on average. Presence of larger, very round, spherule-like particles of higher albedo and subangular bright fragments ranging from 200 μm to >1 mm.
1099	Tyrone area/Mount Darwin	Unstructured	Soil exposed by *Spirit*'s wheel with albedo ranging from very bright to dark gray with intermediate tones, possibly due to the mixing of previous two soil types. Albedo changes are not associated with textural changes. Material is equally fine grained and forms small aggregates to larger clumps, showing cohesiveness. Clumps have clear-cut edges.
1172	Examine This/Everett	Unstructured	Disturbed soil (wheel scuff) - Wheel exposes very bright soil that contrast with the overlying dark material. The bright material appears to extend very close to the surface. Most grains (bright and dark) are below MI resolution. Coarse, rounded sand and smaller particles are present. Bright soil forms aggregates in places.

Table 4 *(continued)*

Sol	Feature/target name	Soil type	Soil type and description
1189	Gertrude Weise/Kenosha Comets	Composite	Unresolved particles up to granule size, including many soil clumps.
1198	Gertrude Weise/Lefty Ganote	Composite	Soil made of dark sandy drift material, fine to medium size sand with unresolved bright soil particles that form aggregates. Aggregates and larger clumps are formed in both bright and dark material.
1230	Silica Valley/Calibration Soil	Bedform	Disturbed soil (MB contact plate) - Sandy drift material with grain-size ranging from fine to medium sand. Underlying material is below MI resolution and of greyer albedo. Isolated small gray spherules are present. Small angular to subrounded bright fragments are present. Fine sand particles are pressed into finer, brighter material under compaction.
1232	Silica Valley/Darlene Mickelsen	Bedform, rock	Sandy drift, dark fine to medium sand passing over outcropping rocks. Resembles material from 1007 but no spherules observed.
1239	Silica Valley/Eileen Deen area	Unstructured	Dual-tone soil (dark and bright). The darker material is associated in part to dark fine to medium sand-size particles but smaller particles have similar albedo. Brighter material is associated with unresolved particles that form aggregates and clumps reaching centimeter size in places.
1244, 1246	Silica Valley/Eileen Deen	Unstructured	Very fine grained material with albedo ranging from very bright to very dark. Aggregates and large clumps are common and show material of various albedo. Fine sand-size particles present, overall angular.
1251, 1257	Silica Valley/Innocent Bystander	Clast, Bedform	Dark sandy drift material partly surrounding rock. Similar to 1232, 1007, and 1252.
1277	Silica Valley/Stealing 2nd	Bedform	Similar to previous but drift material represents the largest fraction of the soil.
1277	Silica Valley/Stealing 3rd	Bedform	Similar to previous but coarser sand reaching medium size is more abundant.
1291	Silica Valley/Stealing 3rd	Bedform	Medium sand dominating with finer sand component present. Albedo ranges from very bright to isolated very dark patches. Unresolved material is present, apparently underlying. Setting is consistent with local drifting sand passing over underlying soil.
1360	S. Promontory/Pumpkin Pie	Unstructured	Unresolved particles forming aggregates and soil that detaches in clumps with clean-cut fractures consistent with cohesiveness. Albedo ranges from dark gray to bright. Six distinct samples for the same sol all showing similar characteristics, some with isolated bright pebbles and aggregates of materials of different albedos and shapes.
1510	Winter Haven/Arthur C. Harmon	Unstructured	Typical characteristics of unstructured soils (013–015), dusty, no particles at MI resolution.
1863	W. Valley/John Wesley Powell	Unstructured	Disturbed soil (MB contact plate) - Very fine grained material below MI resolution. Form aggregates that can reach up to millimeter size. Gray to high albedo.
1922	Troy/Sackrider	Unstructured	Similar to previous but with more lighter aggregates, angular light-toned fragments and possibly isolated medium sand particles.
1925	Troy/Sackrider tweaked	Unstructured	Disturbed soil (MB contact plate) - comparable to previous with possibly very fine sand particles at limit of resolution. Aggregates of wide range of albedo. Isolated small (200 μm) spherule-like particles.
1927	Troy/Olive Branch1	Unstructured	Disturbed soil (MB contact plate) - Sandy, angular material ranging from fine to medium sand. Rounded sand component, with population on average smaller than previous. Soil also contains particles below MI resolution.
1929	Troy/Olive Branch2	Unstructured	Same as previous but with bright angular clasts and small fragments more abundant.
1934	Troy/Olive Branch3	Unstructured	Similar to previous but with lines and patches of very dark material.
1935	Troy/Olive Branch4	Unstructured	Similar to previous.
1936	Troy/Penina1	Unstructured	Disturbed soil (MB contact plate) - Resembles previous soil but with presence of rounded granules/spherules reaching millimeter size. Overall gray albedo with small bright angular fragments.

Table 4 *(continued)*

Sol	Feature/target name	Soil type	Soil type and description
1940	Troy/Penina2	Unstructured	Similar to previous.
1941	Troy/Penina3	Unstructured	Similar to previous.
1945	Troy/CyclopsA	Composite	Disturbed soil (RAT brush) - Sandy material (fine to medium size, subangular to subrounded grains) consistent with local drifts. Underlying very fine material below and at MI resolution. Average gray albedo with bright, angular fragments comparable to those observed in previous sols. Isolated angular pebble and granule; spherule-like particles are present (200–350 μm on average).
1946	Troy/Cyclops Eye2	Composite	Disturbed soil - Similar to previous, deeper brush footprint. The central mound created by the brush shows clear fractures, suggesting cohesiveness of material.
1947	Troy/Cyclops Eye3	Composite	Disturbed soil - Similar to previous with intersecting brush footprints resulting in the accumulation of fine to medium size, subangular to subrounded sand.
1963	Troy/Cyclops Eye3	Composite	Disturbed soil - Similar to previous but different area of the soil exposure. Brushing exposes a soil that shows a large fraction of grains below and at MI resolution, brighter than previous sols. More granule- to pebble-size, bright material is embedded. Very dark patches and small angular fragments similar to previous sols. On a different patch of the same soil (margin of brushed area) for the same sol (image 2M300632708), soil is similar to Sol 1947 with sandy fraction more abundant. Large, bright pebbles present, angular to subangular.
1965, 1966	Troy/Cyclops Eye3	Composite	Disturbed soil - Same as previous, deeper brushing, with sandy, gray rim and outside margins (same soil as Sol 1947); brighter, very fine material in the center of the brushed area. Rounded to subrounded pebbles exposed in the center. Bright material present in the inner wall of the depression made by the brush.
1967	Troy/Olive Branch5	Composite	Very dark to very bright grains. Presence of a dark gray rounded clast and a very rounded dark nodule. Sand-size material is mostly angular and ranges from very fine grained to medium size. Similar mixture of bright angular fragments and gray sand as observed in the previous sols.
1968	Troy/Olive	Composite	Fine, sandy material, similar to Sol 1967, with more dark gray, rounded pebbles. Albedo ranges from very dark to very bright. The finer component shows small linear fractures in places, suggesting cohesiveness.
1975	Troy/Olive Branch6	Composite	Disturbed soil (RAT brush) - Similar to Sol 1945.
1979	Troy/Olive Pit	Composite	Similar to Sol 1945 but with a large (~2 cm), smooth, pitted pebble of dark gray albedo.
1980	Troy/Polyphemus Eye	Composite	Sandy material with bright rock fragments from local outcrops. The sandy material presents similar characteristics as previous soils.

Note. MB = Mössbauer Spectrometer; MI = Microscopic Imager.

with ~100-μm grains being an important component (Sullivan et al., 2008). The size-frequency relationship between surface crust and the underlying materials suggests that the surface represents a minor lag component of the volumetrically more important underlying ≤300-μm material. Similar dark, poorly sorted ≤300-μm soil was observed in other places around the Columbia Hills (MI observations on Sols 158, 279, 314, 480, 481, 736, 747, 812, 822, 908, 913, 937, 1034, 1085, 1230, 1277, 1291, and 1360). This material was also encountered in several places earlier in the mission, while the rover was traversing the plains (MI observations on Sols 43, 73, and 74), and appears to be a potentially mobile component (when induration can be overcome), probably well mixed by winds and therefore unlikely to be derived primarily from local outcrops. This dark, mafic, ≤300-μm material has been developed by wind into prominent bedforms at the El Dorado ripple field. From orbit, the El Dorado ripple field is distinctive for maintaining persistently lower surface brightness compared with the rest of the Columbia Hills and surrounding plains, so it was hypothesized that winds might mobilize the ripples frequently enough to prevent dust from accumulating as thickly as elsewhere in the area. *Spirit* penetrated 8 m into the NE

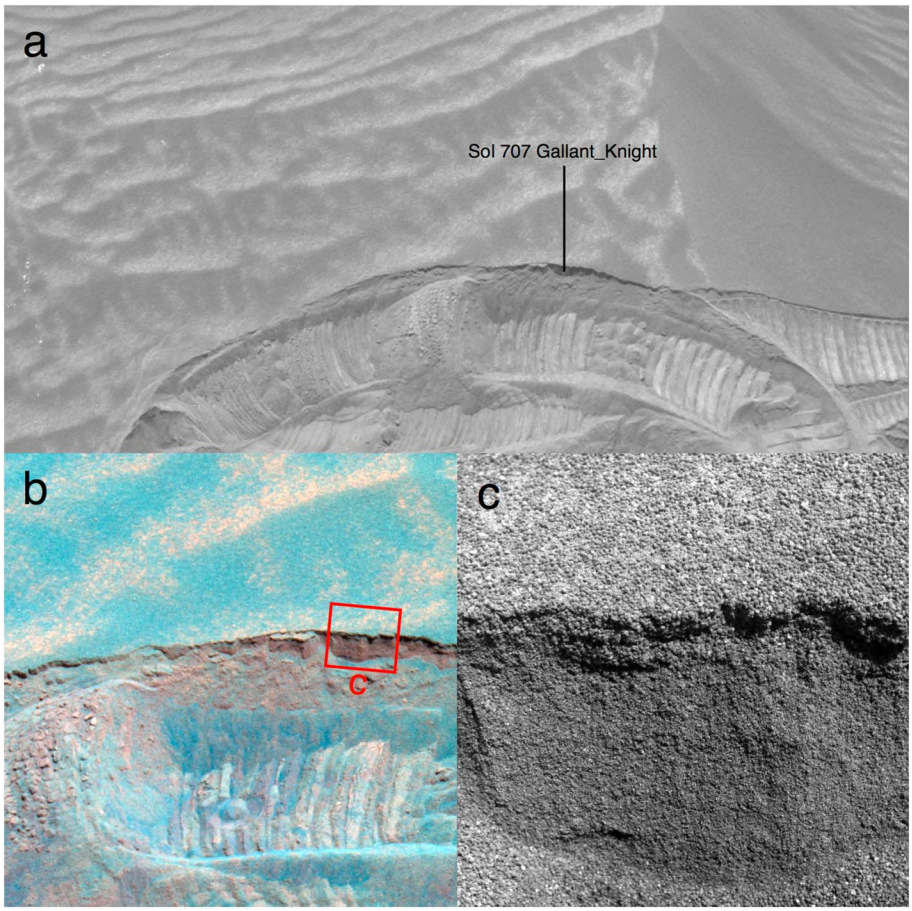

Figure 32. (a) Sol 706 Navcam view of wheel scuff bisecting crest of large ripple of dark, mafic sand at El Dorado feature. (b) Sol 711 Pancam enhanced-color view (L257) showing "roadcut" exposure created by wheel scuff. Color differences between surface and interior materials correlate with grain size observed by the Microscopic Imager. (c) Merge of radiometrically calibrated Microscopic Imager images (3 × 3 cm) of El Dorado target *Gallant_Knight* acquired on Sol 707 with illumination from upper right, revealing well-sorted 200- to 300-um grains at the surface and within the lightly cohesive 1-mm-thick surface crust that give way at greater depths to less sorted material with a higher fraction of finer, poorly resolved grains.

edge of El Dorado on Sol 706. Pancam views from this position showed the presence of some dust (as expected) but only in places more protected from winds (e.g., in troughs of secondary ripples). MI views at El Dorado (Figure 32) showed a very weak surface crust of 200- to 300-μm grains overlying volumetrically more important poorly sorted material ≤300 μm (Sullivan et al., 2008). Using Pancam color data as a guide, dust-free areas were targeted for these MI locations, and dust is not readily apparent in them. Later in the mission, during a strong wind event experienced between Sols 1260 and 1265, ripples of fine material were observed to migrate toward the rover. The material was determined subsequently by MI (Sols 1277 and 1291) to be ≤300 μm as encountered at many other locations previously, confirming the potential mobility of this material at El Dorado and distributed elsewhere around *Spirit*'s landing site (Sullivan et al., 2008).

5.2.2. Geochemical Soil Classification

APXS observations through Sol 1368 of the elemental chemistry of various soils were used by Ming et al. (2008) to geochemically classify soils as organized below. In addition, MI observed the following unclassified soils near Home Plate after Sol 1368: *Arthur C. Harmon*, *John Wesley Powell*, *Sackrider Tweaked*, *Olive Tree 1 and 2*, *Olive Branch* 1–6, *Penina* 1–4, *Cyclops*, *Cyclops Eye 2, 3, 5, and 6, Olive*, *Olive Pit*, *Polyphemus Eye*, *Sackrider*, *Polyphemus Eye3*, *Olive Leaf*, and *Thoosa*. These soils are poorly sorted in general and are typically rich in sulfur below a surface layer of eolian basaltic sand (Siebach et al., 2010). The angular grains in these soils and their poor sorting indicate that they have experienced only limited transport.

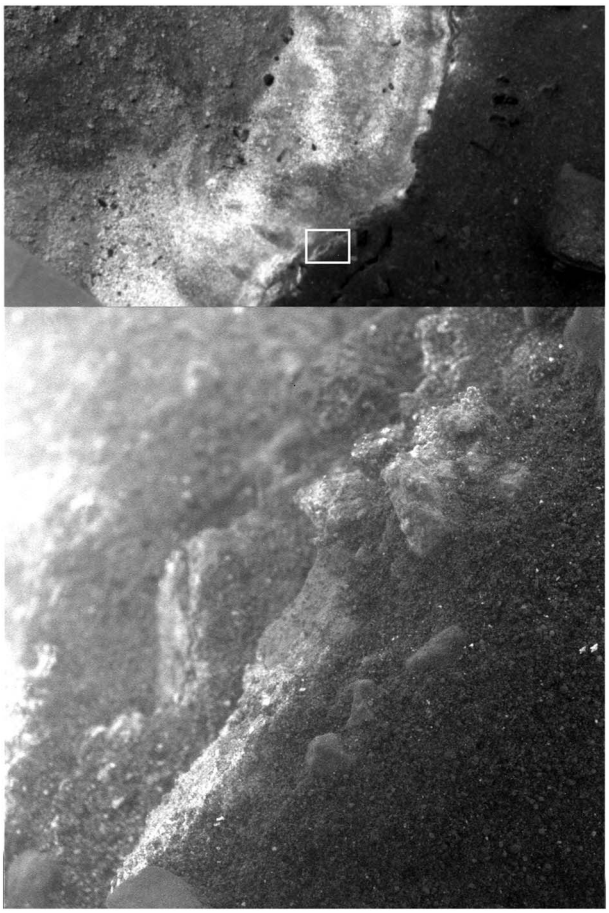

Figure 33. (top) Sol 1933 Pancam blue (R7) image 2P297975925ESFB1E5P2382R7M1 of the Troy feature, showing footprint of the Microscopic Imager image below in white. (bottom) Focal merge of Microscopic Imager images of Olive Tree 1 acquired on Sol 1927 when target was shadowed except at left edge. Area shown is 3 × 3-cm square.

The *Crumble* soil on Cumberland Ridge has a chemical composition that is different from the Gusev plain soils (Gellert et al., 2006); it was not included in the Ming et al. (2008) classification. The Sol 457 and 460 MI images of the Crumble soil APXS and Mössbauer target *Almonds* show that it is a mixture of locally derived lithic fragments and windblown particles. The larger lithic fragments are likely the cause of the difference in chemistry relative to other soils.

While *Spirit* was embedded in the sandy soil at "Troy" (Figure 1) from Sol 1871 until the end of the mission, the materials in the IDD workspace were studied in detail (Arvidson et al., 2010). MI images of the Troy sands show that the Cyclops Eye soils are better sorted than those at Sackrider and Penina. The RAT was used to repeatedly expose subsurface material at Cyclops Eye and Polyphemus Eye. MI images taken during this experiment show that particle properties vary with depth; specifically, the RAT exposed bright sand grains about 1 cm below the surface at Cyclops Eye that were not observed at Polyphemus Eye or Thoosa. However, MI images of Olive Tree, the wall of an area that was disturbed by the rover wheels, show centimeter-scale layers of poorly sorted, cemented sands that also contain bright grains (Figure 33). These and other *Spirit* observations suggest that sulfates have been mobilized by water and concentrated to form crusts, at least locally (Arvidson et al., 2010).

5.2.2.1. Laguna Soil Class

The *Laguna* class soils are the most common observed by *Spirit*, on both the Gusev plains and the Columbia Hills (Ming et al., 2008). This soil class was divided into subclasses by Morris et al. (2006) based on subtle chemical and mineralogical variations. Specifically, MAI (the ratio of Fe^{3+} to total iron in alteration products) and sulfur content were used to define the subclasses discussed below; the geochemical boundaries between them are not distinct (Ming et al., 2008). MI images of *The Boroughs* trench were discussed previously

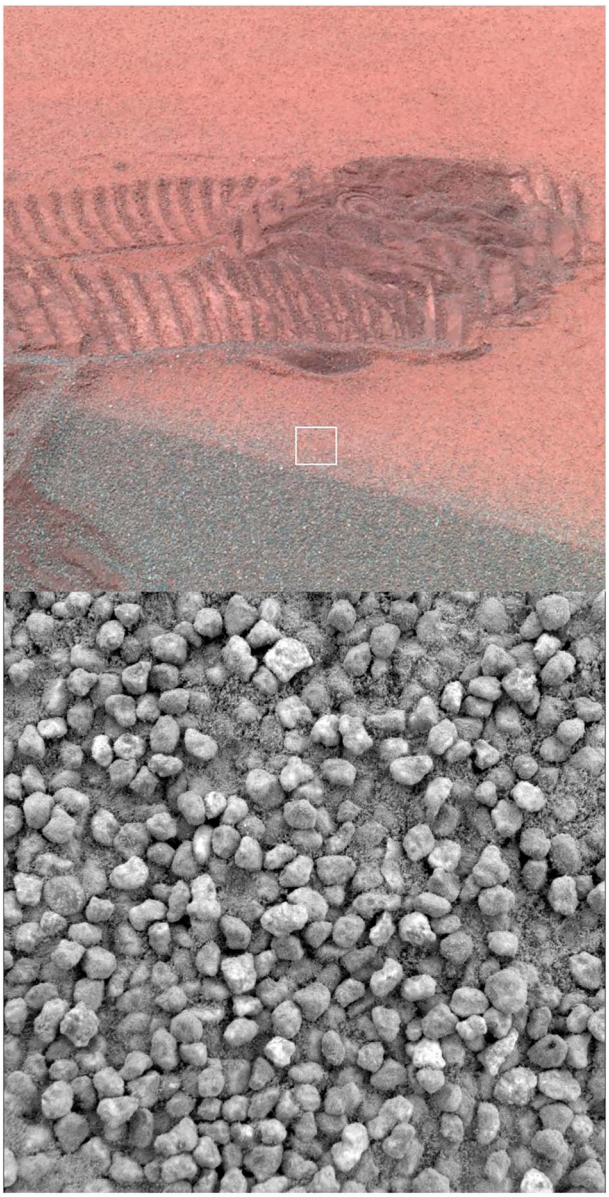

Figure 34. (top) Sol 612 enhanced-color Pancam image 2P180695038RSDAEMDP2589L2MZ of the *Cliffhanger* feature, showing approximate location of Microscopic Imager image below in white. (bottom) Radiometrically calibrated Microscopic Imager image 2M180252684IFFAEM9P2977M2F1 of the HangTwo target, taken on Sol 607 when target was fully shadowed. Note coarse sand grains on the surface and finer-grained material below.

(Herkenhoff et al., 2006), so the Boroughs subclass is not discussed here. However, new Laguna soil subclasses were discovered after Sol 450 and are discussed below.

The *Dubloon* subclass is named after the Dubloon APXS target, which was imaged by the MI on Sol 499. Images of Dubloon and *HangTwo* (acquired on Sols 607 and 612) show surfaces covered by subangular coarse sand grains with fine sand grains visible below (Figure 34). The coarse grains were evidently not transported far, consistent with their composition being similar to nearby Wishstone class rocks (Sullivan et al., 2008).

The *Panda* subclass soils at the *El Dorado* ripple field were observed by the MI on Sols 707 (Figure 32c), 709, and 710; other soils in this subclass were imaged before Sol 450. MI images of the undisturbed APXS target *Shadow* show well-rounded fine- to medium-grained sand that was likely emplaced recently by wind-driven saltation (Sullivan et al., 2008). Images of the APXS target *Edgar* on the floor of a wheel scuff show a mixture of

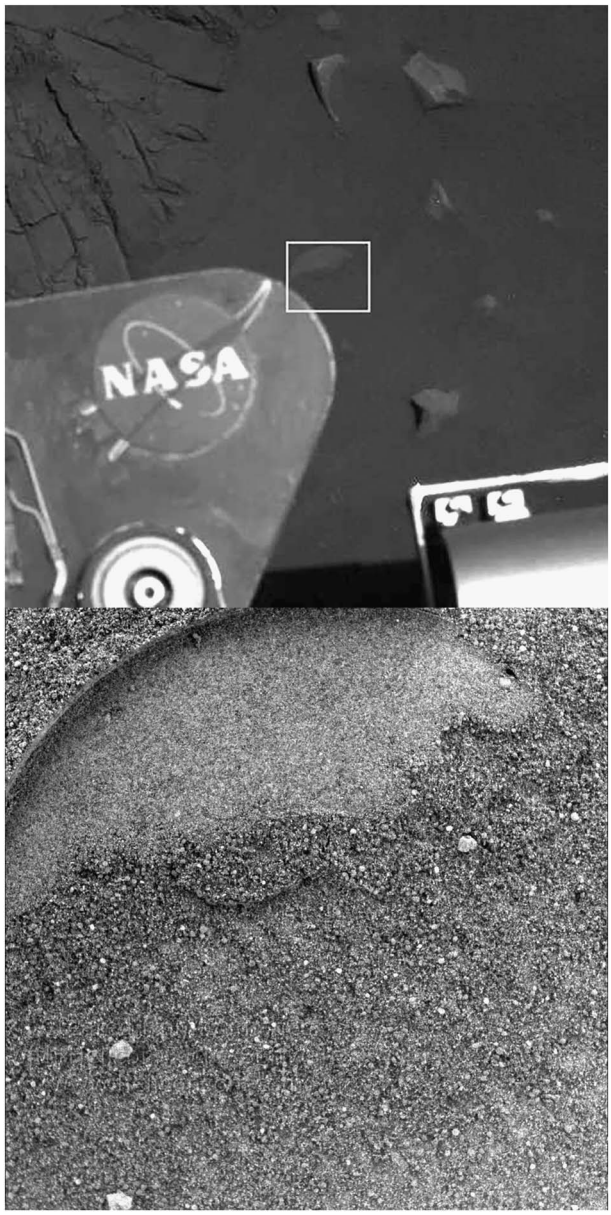

Figure 35. (top) Sol 480 Pancam blue (L7) image 2P168975351ESFAAACP2581L7M1 of Mössbauer contact plate imprint into Bell target, showing footprint of Microscopic Imager image below in white. Rover hardware partly obscures the surface. (bottom) Focal merge of Microscopic Imager images acquired on Sol 480 when the Bell target was fully shadowed. Area shown is 3 × 3-cm square.

0.2- to 0.3-mm surface grains and <0.1-mm grains from the subsurface. The lack of dust apparent in the MI images of the Panda soils is consistent with the composition measured by APXS (Ming et al., 2008).

The *Liberty* subclass soils include *Bell* (imaged by the MI on Sols 477 and 480, called *Liberty Bell 2* by Ming et al. [2008]), *Progress 1* (Sol 830), *Progress 2* (Sol 858), *Mawson* (Sols 812 and 1008), and *Bear Island* (Sol 1017). The undisturbed surfaces of these soils are dominated by fine, subangular to subrounded sand grains, with variable amounts of coarse sand. Molding of the soil by the Mössbauer contact plate indicates that some unresolved very fine sand and silt grains are present (Figure 35). Incremental brushing of the Progress target exposed more uniformly fine-grained material at a few millimeters depth, suggesting that the coarser grains are a surficial lag deposit. Mössbauer contact plate imprints into the Progress 2 brushed target are smooth, likely due to a significant fraction of very fine grained sand or silt.

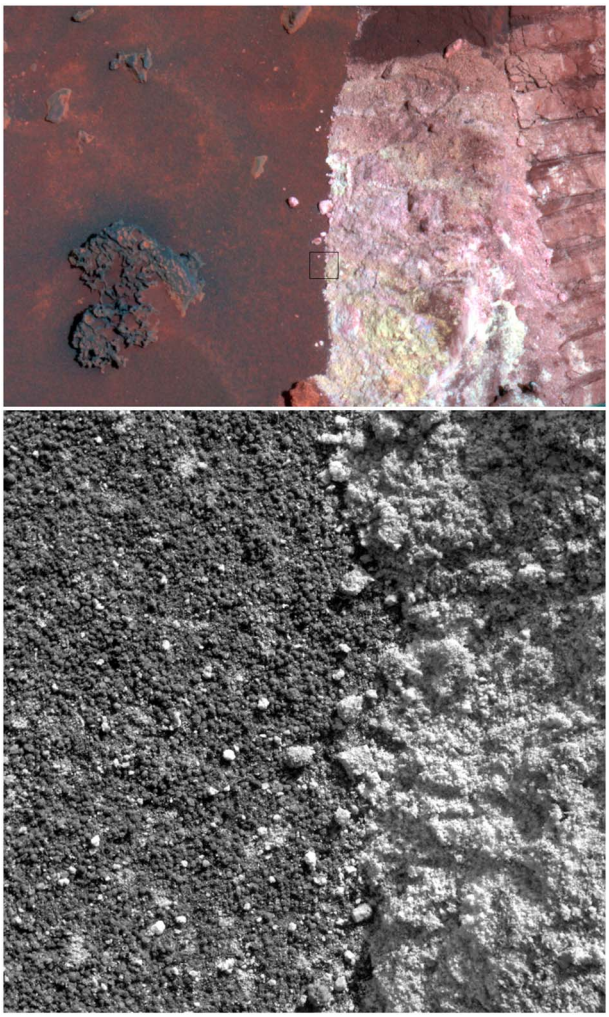

Figure 36. (top) Sol 723 Pancam enhanced-color image 2P190546975IOFAMFHP2542L257C2 of bright soil in wheel track at right and darker, undisturbed surface at left. Location of this Arad feature shown in Figure 1. Black box shows footprint of 3 × 3-cm Microscopic Imager image below. (bottom) Focal merge of radiometrically calibrated Microscopic Imager images of target *Zoar*, acquired on Sol 724 with illumination from upper right.

The *Gobi* subclass soils include Lambert (Sol 588) and Progress (Sol 822), and other targets that were observed before Sol 450. These soils are generally finer grained than the other Laguna class soils, consistent with the higher MAI and sulfur content (Ming et al., 2008). Curiously, the finer-grained Liberty subclass soils exposed by brushing of the Progress soil target have lower MAI and sulfur content than the more poorly sorted Gobi subclass surface.

5.2.2.2. Paso Robles Soil Class

The sulfur-rich *Paso Robles* soil class is named after the Paso Robles target on the northwest flank of Husband Hill (Herkenhoff et al., 2006; Ming et al., 2008). Similar but chemically unique soils were found at *Arad* (Sols 723–724), *Berkner Island* (Sol 1013), *Mount Darwin* (Sol 1099), and Troy (Siebach et al., 2010). These soils are typically composed of bright, poorly sorted, subangular grains (Figure 36), consistent with minimal transport of secondary sulfate minerals (Yen et al., 2008). Pancam spectra indicate that ferric sulfates are likely present in these soils (Johnson et al., 2007; Wang et al., 2008).

5.2.2.3. Gertrude Weise Soil Class

The *Gertrude Weise* feature on the east side of Home Plate includes MI targets *Kenosha Comets* and *Lefty Ganote*. APXS data indicate that these immature soils are very rich in silica, possibly the result of fumarolic leaching or precipitation from hydrothermal fluids. The MI images of Kenosha comets show a matrix-supported texture in some of the larger grains (Figure 37). Images of the nearby Lefty Ganote target show

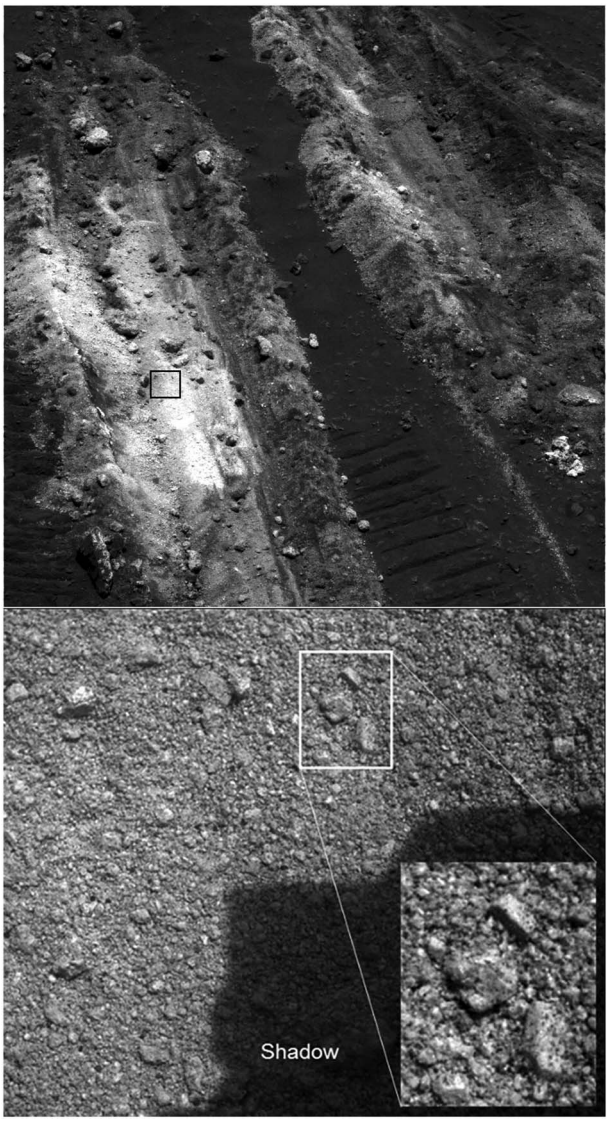

Figure 37. (top) Sol 1198 Pancam blue image 2P232715127EFFATB4P2539L7M1 of Gertrude Weise wheel track, with area shown below outlined in black. For context, see Figure 23a. (bottom) Part of Microscopic Imager image 2M231921836 of target Kenosha Comets, acquired on Sol 1189 with illumination from top. Full frame is ~3 cm across; inset shows 4.7 × 5.8-mm area. Note in inset that largest (very coarse sand) grains appear to contain dark grains in brighter matrix and wide range of clast sizes and shapes.

that darker, finer grains have been mixed into the soil by the rover wheel, consistent with the lower silica abundance measured by APXS (Ruff et al., 2011).

5.2.2.4. Eileen Dean Soil Class

The high-magnesium, magnetite-rich soils in this class were observed by the MI at *Eileen Dean* (Sols 1235, 1239, and 1244) and *Eileen Dean 2* (Sol 1246) on the east side of Home Plate. The Sol 1235 MI images are mostly out of focus, so MI images of Eileen Dean were acquired again on Sols 1239 and 1244. These targets are in a wheel track that exposes bright clasts or clods of a wide range of sizes, mixed with fine-grained dark soil (Figure 38).

5.2.3. Change Detection

Changes in the distribution of dark soil and coarser particles are clearly seen in MI images of Innocent Bystander taken on Sols 1251 and 1252, most likely caused by winds (Ruff et al., 2011). Motion of sand grains is clearly visible in images taken about 7 min apart (see supporting information).

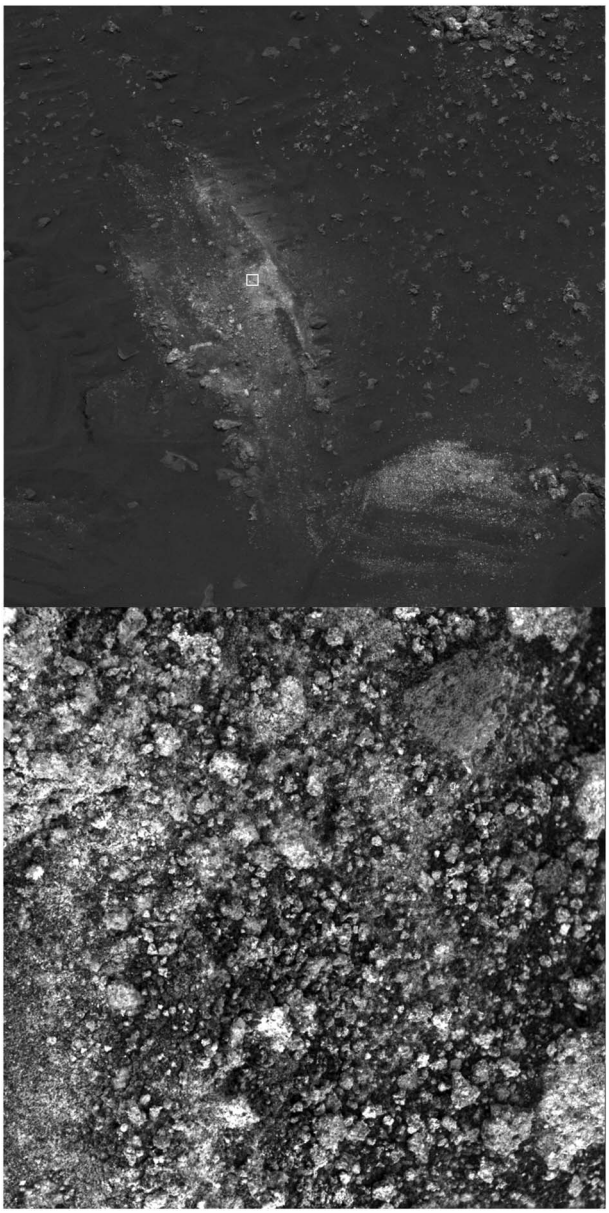

Figure 38. (top) Radiometrically calibrated blue (L7) Pancam image 2P237068703RSDAUAXP2574L7MZ of wheel tracks in the Silica Valley feature, acquired on Sol 1247, with approximate location of area shown below outlined in white. (bottom) Focal merge of Microscopic Imager images of target *Eileen Dean*, acquired on Sol 1244 when the target was fully shadowed. Area shown is 3 × 3-cm square.

The MI observed soil targets *Penina* and *Sackrider* repeatedly in an effort to understand the cause of changes in bright soils seen in images taken by other cameras. At both locations, a decrease in the abundance of fine (0.1–0.3 mm) sand grains was observed over timescales of a few weeks, leaving a lag of coarser, subangular grains (Siebach et al., 2010). These observations and associated multispectral changes were interpreted by Rice et al. (2011) as the result of wind mobilization of dust aggregates and fine sand grains; no evidence for mineralogic changes was found.

5.3. Rover Images

In addition to imaging of the Martian surface, the MI was used to image various parts of the *Spirit* rover that could be reached by the IDD.

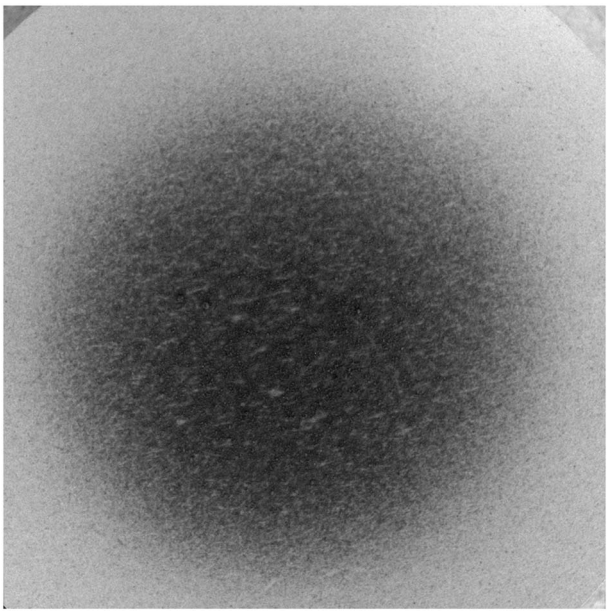

Figure 39. Radiometrically calibrated Microscopic Imager image 2M235561554 IFFAU00P2906-M2F1 of *Spirit*'s filter magnet, taken when the magnet was fully shadowed. Area shown in 3 × 3-cm square.

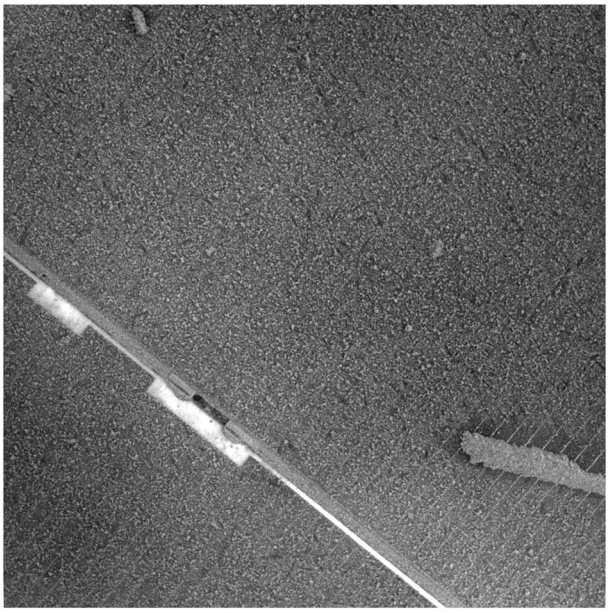

Figure 40. Radiometrically calibrated MI image 2M257129441IFFAY00P2936M2F2 of part of *Spirit*'s solar array, taken when target was fully shadowed. Area shown is 3 × 3-cm square. Note the ~8-mm long, 1.5-mm wide dust aggregate at lower right (Vaughan et al., 2010).

5.3.1. Magnets

The MI was used to image the filter and capture magnets on *Spirit* (Bertelsen et al., 2004), showing variations in the accumulation of dust and retention of magnetic grains. Images acquired on Sol 505 show that the strong wind event around Sol 419 removed all but the most strongly magnetic dark grains from the capture magnet (Vaughan et al., 2010). The rover was stationary during the second Mars winter of the mission, and MI images of the magnets taken on Sol 963 show that a thick dust layer had accumulated during the winter (Madsen et al., 2009). As dust continued to accumulate on the magnets, MI images taken on Sol 1006 show evidence that the dust had formed 0.2- to 0.4-mm agglomerates, and a Sol 1230 image of the filter magnet shows bright, narrow streaks that appear to have been formed by saltating sand grains (Figure 39). High winds during the 2007 global dust storm likely mobilized these dust agglomerates, as seen in the Sol 1355 MI image of the capture magnet. The Sol 1504 image of the capture magnet shows that dust accumulation continued after the dust storm abated. Then another strong wind event occurred, and the Sol 2017 image of the capture magnet shows that much of the bright dust had been removed, leaving behind darker, strongly magnetic fine sand grains (Vaughan et al., 2010).

5.3.2. Solar Panel

Changes in dust and sand accumulation were also evident in MI images of *Spirit*'s deck and solar panel. An MI image acquired on Sol 505 shows well rounded and sorted sand grains (0.15- to 0.25-mm diameter) next to the solar panel (Greeley et al., 2006). These grains are inferred to have been emplaced by strong winds around Sol 419, evidence for saltation at least to the 70-cm height of *Spirit*'s solar panel (Vaughan et al., 2010). Later images show that the sand grains were no longer present in the same location, having been moved to another location on the rover deck or removed completely. The images of the solar panel also show evidence for dust agglomeration, including an elongated feature at least 8-mm long in images acquired on Sols 1473 and 1506 (Figure 40).

5.3.3. Underbelly

After *Spirit* became embedded in the soils at Troy, imaging below the belly of the rover was desired in support of extrication planning. The MI is the only camera on the IDD, so was the only option for imaging the underbelly of the rover. Such images were acquired even though it was recognized that they would be well out of focus but were still useful in monitoring the progress of extrication activities and in planning future activities. Image processing improved the quality of the out-of-focus images, as shown in Figure 41. The last *Spirit* MI image taken during the mission, of the rover underbelly, was acquired on Sol 2113.

6. Summary and Conclusions

The 5,923 full-frame images returned by *Spirit*'s MI have provided key constraints in the interpretation of MER observations in Gusev crater. Specifically, millimeter-scale features and textures have informed the analysis of rocks and soils observed during the mission. Changes in MI performance were minor until the 2007 dust storm that contaminated the optics of the camera. Poststorm data were used to correct for

Figure 41. Mosaic of Microscopic Imager images of material beneath rover belly filtered and contrast enhanced by Joel Hagen to show detail.

changes in flat-field response due to the dust storm; images acquired after the storm have been reprocessed accordingly. MI data acquired before the dust storm can be calibrated to 1% relative (within each image) and 30% absolute radiometric accuracy. Images acquired after the dust storm are somewhat less accurately calibrated, and radiometric uncertainties are not well known. Raw and calibrated data products are available from the PDS and can be searched using the Analyst's Notebook.

In many cases, MI data have proven to be essential in constraining hypotheses for the origin and evolution of rocks and soils investigated by *Spirit*. Specifically, the observations of grain-supported and nodular textures with subangular to subrounded grains on Cumberland Ridge helped guide the interpretation of Watchtower class rocks as altered volcanic airfall deposits. Crumpler et al. (2011) used microscopic textures to interpret the provenance of Husband Hill rocks in terms of fallout and ejecta from impacts of various sizes into materials with diverse initial alteration states. Volcaniclastic material such as lapilli tuff may also be present. The smooth, slightly pitted appearance of Backstay and Irvine class rocks is consistent with crystallized volcanic rock. Elizabeth Mahon and Good Question class rocks include pitted textures that are remarkably similar to those observed in sinter deposits at an active hot spring in Chile (Ruff & Farmer, 2016). The microtextures of the volcaniclastic rocks at Home Plate and Algonquin class rocks are similar, suggesting that hydrovolcanic processes were important in the deposition of rocks at Home Plate and in the Columbia Hills (Yingst et al., 2007).

Of course, hand lens-scale images do not always provide diagnostic information. For example, observations of poorly sorted grains in some Algonquin class rocks have been used to interpret them as either immature sandstone (Crumpler et al., 2011) or volcanic tephra (Ruff et al., 2014). And while the texture of Comanche is consistent with carbonate precipitation, MI images cannot be used to determine whether the carbonate is present in the grains or in the cement matrix. MI observations of bimodal grain sizes and various shapes in Barnhill class rocks cannot distinguish between an impact versus volcaniclastic origin of Home Plate, but well-sorted grains in rocks on the west side of Home Plate provide evidence of eolian reworking (Lewis et al., 2008). The fine-scale laminae seen at Posey may have been formed by dilute pyroclastic density currents, but other hypotheses cannot be ruled out. Dark, rounded grains may represent accretionary lapilli or impact spherules (Yingst et al., 2007). When grains are too fine ($<$0.1 mm in size) to be resolved, as in Fuzzy Smith, MI images are not as useful in interpreting origin.

MI observations of soils in Gusev crater have been used to constrain their physical properties (Herkenhoff, Golombek, et al., 2008) and measure their size-frequency distribution (Cabrol et al., 2008, 2014; Greeley et al., 2008; Karunatillake et al., 2010, 2014; Yingst et al., 2008, 2010). Surficial sediment typically shows evidence of eolian modification, while subsurface soil grains are less well sorted and more angular, probably due to impact comminution (McGlynn et al., 2011). The observed size-frequency distributions of soil particles are primarily due to (1) recent eolian saltation and sorting of fine to medium sand grains, (2) limited transport of more angular, coarse sand grains, and (3) past impact-induced creep of well-rounded, coarse sand grains (Cabrol et al., 2014). After using *Spirit*'s wheels to expose the interior of a bedform at El Dorado, MI images showed evidence for a surface lag of well-sorted (200–300 μm) sand over a less sorted, finer-grained deposit at depth. These observations led to the interpretation of these bedforms as ordinary ripples, formed by saltation of $\leq$300 μm sand grains (Sullivan et al., 2008), as opposed to the coarse-grained ripples observed earlier in the mission (Herkenhoff et al., 2006), which are thought to be formed by saltation-driven impact creep.

Both sulfur- and silica-rich soils are relatively poorly sorted and are interpreted to be immature. MI observations of Kenosha Comets (nearly pure silica) show evidence for dark grains in a brighter matrix, consistent with precipitation of silica from hydrothermal fluids.

MI images of the magnets and solar panels on the top of the rover show that dust agglomerates can form quickly (Vaughan et al., 2010). Similar dust agglomerates were observed on the Martian surface (Herkenhoff, Golombek, et al., 2008) and are more easily lifted off the surface by winds than are individual dust particles. These results show that dust can be removed from the surface without saltation of larger grains (Sullivan et al., 2008).

While MI images of *Spirit*'s underbelly were useful in planning extrication of the rover, it was not possible to tilt the rover's solar panels toward the Sun, as had been done during previous Martian winters. Ultimately, the vehicle shut down due to low power levels in March 2010 after 2210 sols (over 6 Earth years) of productive operations–not bad for a mission designed to last only 90 sols on Mars!

Appendix A: Summary of *Spirit* MI observations

No. = Number of images in stack. CS = Dust cover state (C = closed, O = open). S/M = Stereo (S) or monoscopic (M) observation. Pancam Sequence = Best multispectral observation of same target.

Table A1

Sol	Starting Image_ID	Target	Feature	Target type	No.	CS	S/M	Relation to RAT/MB	Pancam sequence
2	2M126553157	NA	Spirit	Health Check	1	C	M	NA	None
13	2M127522385	Sky Flat	Sky	Sky	1	O	M	NA	None
13	2M127522505	Sky Flat	Sky	Sky	1	C	M	NA	None
13	2M127523552	FirstSoil1Final	First Soil	Soil	5	O	M	Pre-MB	p2269, Sol 012
15	2M127691206	FirstSoil1Final	First Soil	Soil	5	O	M	Post-MB	p2269, Sol 012
17	2M127876303	Prospect	Adirondack	Rock	7	O	M	Pre-Brush, Pre-MB	p2382, Sol 030
17	2M127876805	Prospect	Adirondack	Rock	1	C	M	Pre-Brush, Pre-MB	p2382, Sol 030
33	2M129296709	Prospect	Adirondack	Rock	7	C	M	Post-Brush, Pre-MB	p2943, Sol 033
33	2M129297197	Prospect	Adirondack	Rock	14	O	S	Post-Brush, Pre-MB	p2943, Sol 033
35	2M129468450	Prospect	Adirondack	Rock	10	O	S	Post-Grind, Pre-MB	p2578, Sol 035
35	2M129469022	Prospect	Adirondack	Rock	1	C	M	Post-Grind, Pre-MB	p2578, Sol 035
39	2M129819881	Sideslope2	Squiggle	Drift	1	C	M	NA	p2593, Sol 039
39	2M129820106	Sideslope2	Squiggle	Drift	10	O	S	NA	p2593, Sol 039
41	2M130001180	Crest	Arena	Drift	5	O	M	Pre-MB	p2953, Sol 041
41	2M130001510	Crest	Arena	Drift	1	C	M	Pre-MB	p2953, Sol 041
41	2M130001727	Trough	Arena	Drift	7	O	M	NA	p2399, Sol 040
41	2M130002290	Trough	Arena	Drift	1	C	M	NA	p2399, Sol 040
42	2M130089167	Lace	Mimi Shoe	Rock	10	O	S	Pre-MB	p2538, Sol 042
42	2M130089783	Lace	Mimi Shoe	Rock	1	C	M	Pre-MB	p2538, Sol 042
43	2M130169106	Mimi_Tracks2	Mimi Tracks	Soil	10	O	S	Post-MB	p2598, Sol 040
43	2M130169685	Mimi_Tracks2	Mimi Tracks	Soil	1	C	M	Post-MB	p2598, Sol 040
44	2M130267298	Soil1	Ramp Flats	Soil	5	O	M	Pre-MB	None
45	2M130356065	Halo_01	Angel Flats	Soil	1	C	M	Pre-MB	None
45	2M130356182	Halo_01	Angel Flats	Soil	5	O	M	Pre-MB	None
46	2M130463038	Trout 1	Grande Flats	Soil	14	O	S	Pre-MB	p2418, Sol 047
46	2M130463916	Trout 1	Grande Flats	Soil	1	C	M	Pre-MB	p2418, Sol 047
46	2M130464431	Sky Flat	Sky	Sky	1	O	M	NA	None
46	2M130464495	Sky Flat	Sky	Sky	1	C	M	NA	None
48	2M130618323	WallMIonly1	RoadCut	Trench	7	O	M	Pre-MB	p2418, Sol 047
48	2M130618766	WallMIonly1	RoadCut	Trench	1	C	M	Pre-MB	p2418, Sol 047
48	2M130618952	Below WallMIonly1	RoadCut	Trench	7	O	M	NA	p2418, Sol 047
48	2M130619416	Below WallMIonly1	RoadCut	Trench	1	C	M	NA	p2418, Sol 047
48	2M130620923	Floor3	RoadCut	Trench	7	O	M	Pre-MB	p2418, Sol 047
48	2M130621417	Floor3	RoadCut	Trench	1	C	M	Pre-MB	p2418, Sol 047
49	2M130707168	Floor3	RoadCut	Trench	1	C	M	Post-MB	p2418, Sol 047
49	2M130707421	Dividing Line	RoadCut	Trench	7	O	M	NA	P2418, Sol 047
49	2M130708373	Dividing Line	RoadCut	Trench	1	C	M	NA	p2418, Sol 047
49	2M130708543	MasonDixon	RoadCut	Trench	7	O	M	NA	p2418, Sol 047
49	2M130709093	Wall3	RoadCut	Trench	7	O	M	NA	p2418, Sol 047
50	2M130795909	WallMIonly1	RoadCut	Trench	3	O	M	Post-MB	p2420, Sol 050
50	2M130796193	MasonDixon	RoadCut	Trench	3	O	M	NA	p2418, Sol 047
51	2M130884803	Soil2	Split Rock Flats	Soil	5	O	M	NA	p2421, Sol 050

Table A1 *(continued)*

Sol	Starting Image_ID	Target	Feature	Target type	No.	CS	S/M	Relation to RAT/MB	Pancam sequence
51	2M130885122	Soil2	Split Rock Flats	Soil	1	C	M	NA	p2421, Sol 050
52	2M130974067	SugarT_1	Sugar	Drift	1	C	M	Pre-MB	p2425, Sol 051
52	2M130974187	SugarT_1	Sugar	Drift	5	O	M	Pre-MB	p2425, Sol 051
53	2M131077199	Filter Magnet	Spirit	Rover	3	O	M	NA	p2919, Sol 053
53	2M131077515	Filter Magnet	Spirit	Rover	1	C	M	NA	P2919, Sol 053
53	2M131077842	Capture Magnet	Spirit	Rover	3	O	M	NA	p2919, Sol 053
53	2M131078362	Capture Magnet	Spirit	Rover	1	C	M	NA	p2919, Sol 053
54	2M131150911	Ridge1	Wrinkle	Soil	5	O	M	Pre-MB	None
54	2M131151413	Ridge1	Wrinkle	Soil	1	C	M	Pre-MB	None
54	2M131155006	Ridge1	Wrinkle	Soil	3	O	M	Post-MB	None
54	2M131155257	Ridge1	Wrinkle	Soil	1	C	M	Post-MB	None
55	2M131242017	Heyworth_RAT	Humphrey	Rock	5	O	M	Pre-Brush	p2429, Sol 054
55	2M131242375	Heyworth_RAT	Humphrey	Rock	1	C	M	Pre-Brush	p2429, Sol 054
57	2M131420525	Heyworth_1	Humphrey	Rock	5	O	M	Post-Brush	p2597, Sol 060
57	2M131420828	Heyworth_1	Humphrey	Rock	1	C	M	Post-Brush	p2597, Sol 060
57	2M131421037	RightEar	Humphrey	Rock	5	O	M	Post-Brush, Pre-MB	p2597, Sol 060
57	2M131421417	RightEar	Humphrey	Rock	1	C	M	Post-Brush, Pre-MB	p2597, Sol 060
59	2M131597743	Heyworth_1	Humphrey	Rock	5	O	M	Post-Grind, Pre-MB	p2591, Sol 058
59	2M131598082	Heyworth_1	Humphrey	Rock	1	C	M	Post-Grind, Pre-MB	p2591, Sol 058
60	2M131690161	Heyworth_2	Humphrey	Rock	25	O	S	Post-Grind, Pre-MB	p2597, Sol 060
60	2M131691742	Heyworth_2	Humphrey	Rock	5	C	S	Post-Grind, Pre-MB	p2597, Sol 060
63	2M131952543	Nail4	Plank	Soil	5	O	M	Pre-MB	p2530, Sol 063
63	2M131952890	Nail4	Plank	Soil	1	C	M	Pre-MB	p2530, Sol 063
65	2M132132493	Soil1	SugarLoafFlats	Soil	3	O	M	Post-MB	p2534, Sol 065
65	2M132132777	Escarpment1	SugarLoafFlats	Soil	5	O	M	NA	p2534, Sol 065
65	2M132133132	Escarpment1	SugarLoafFlats	Soil	1	C	M	NA	p2534, Sol 065
68	2M132401584	Gobi1	Deserts	Soil	5	O	M	Pre-MB	None
70	2M132590791	Gobi1	Deserts	Soil	10	O	S	Post-MB	None
71	2M132663577	Window	Deserts	Soil	5	O	M	Post-MB	None
73	2M132840736	Polar	Bear Paw	Scuff	7	O	M	Pre-MB	p2352, Sol 072
73	2M132841379	Spectacle2	Bear Paw	Scuff	7	O	M	NA	p2557, Sol 073
73	2M132841868	Spectacle2	Bear Paw	Scuff	1	C	M	NA	p2557, Sol 073
73	2M132842058	Kodiak	Bear Paw	Scuff	7	O	M	NA	p2977, Sol 073
73	2M132842543	Kodiak	Bear Paw	Scuff	1	C	M	NA	p2977, Sol 073
73	2M132842726	Panda_new	Bear Paw	Scuff	7	O	M	Pre-MB	p2557, Sol 073
74	2M132934791	Polar	Bear Paw	Scuff	3	O	M	Post-MB	p2352, Sol 074
74	2M132935173	Panda_new	Bear Paw	Scuff	3	O	M	Post-MB	p2352, Sol 072
75	2M133017039	Soil2	Patio	Soil	5	O	M	NA	p2562, Sol 075
76	2M133104521	Appendix	Geoff	Dusty rock	6	O	S	Pre-MB	p2566, Sol 076
76	2M133113166	Appendix	Geoff	Dusty rock	4	O	S	Post-MB	p2566, Sol 076
77	2M133196972	Soil1	Mazatzal Flats	Soil apron	6	O	S	Pre-MB	p2568, Sol 076
77	2M133205985	Soil1	Mazatzal Flats	Soil apron	4	O	S	Post-MB	p2568, Sol 076
78	2M133285037	Arizona	Mazatzal	Rock	6	O	S	Pre-Brush	p2574, Sol 078
78	2M133285545	Illinois	Mazatzal	Rock	6	O	S	Pre-Brush	p2574, Sol 078
78	2M133286074	New York	Mazatzal	Rock	6	O	S	Pre-Brush, Pre-MB	p2574, Sol 078
79	2M133382710	Illinois_tweaked	Mazatzal	Rock	10	O	S	Post-Brush	p2588, Sol 081
79	2M133383410	Illinois_tweaked	Mazatzal	Rock	1	C	M	Post-Brush	p2588, Sol 081
79	2M133386122	New York	Mazatzal	Rock	10	O	S	Post-Brush	p2957, Sol 079
79	2M133386832	New York	Mazatzal	Rock	1	C	M	Post-Brush	p2957, Sol 079
80	2M133463169	Texas	Mazatzal	Rock	10	O	S	Pre-Brush	p2979, Sol 080
80	2M133463870	Texas	Mazatzal	Rock	1	C	M	Pre-Brush	p2979, Sol 080
82	2M133648272	New York	Mazatzal	Rock	25	O	S	Post-Grind, Pre-MB	p2559, Sol 082
82	2M133649889	New York	Mazatzal	Rock	5	C	S	Post-Grind, Pre-MB	p2559, Sol 082
82	2M133650507	Oregon	Mazatzal	Rock	5	O	M	Pre-MB	p2599, Sol 086
82	2M133650903	Oregon	Mazatzal	Rock	1	C	M	Pre-MB	p2599, Sol 086
84	2M133825381	PMA	PMA	Sun (Error)	37	C	M	NA	None
85	2M133914563	Brooklyn	Mazatzal	Rock	25	O	S	Post-Grind, Pre-MB	p2596, Sol 085
85	2M133916255	Brooklyn	Mazatzal	Rock	5	C	S	Post-Grind	p2596, Sol 085
85	2M133916997	Hawaii	Mazatzal	Rock	10	O	S	Pre-MB	p2596, Sol 085
85	2M133917351	Hawaii	Mazatzal	Rock	1	C	M	Pre-MB	p2596, Sol 085
89	2M134263041	Shredder	Snowboard	Rock	5	O	M	NA	p2956, Sol 089

Table A1 *(continued)*

Sol	Starting Image_ID	Target	Feature	Target type	No.	CS	S/M	Relation to RAT/MB	Pancam sequence
89	2M134263385	Shredder	Snowboard	Rock	1	C	M	NA	p2956, Sol 089
89	2M134263587	Rams	TCHS	Rock	5	O	M	NA	p2532, Sol 089
89	2M134263975	Rams	TCHS	Rock	1	C	M	NA	p2532, Sol 089
92	2M134534074	Filter Magnet	Spirit	Rover	3	O	M	NA	None
92	2M134534398	Capture Magnet	Spirit	Rover	3	O	M	Pre-MB	None
99	2M135152796	SoHo	Route66	Rock	10	O	S	Post-Brush, Pre-MB	p2544, Sol 100
99	2M135153170	SoHo	Route66	Rock	2	C	S	Post-Brush, Pre-MB	p2544, Sol 100
105	2M135687370	Flats1	Bitterroot flats	Soil	5	O	M	Post-MB	p2547, Sol 105
105	2M135687707	Flats1	Bitterroot flats	Soil	1	C	M	Post-MB	p2547, Sol 105
110	2M136126236	Soil1	Waffle Flats	Soil	6	O	S	Pre-MB	p2557, Sol 110
110	2M136131617	Soil1	Waffle Flats	Soil	3	O	M	Post-MB	p2557, Sol 110
113	2M136401275	Mayfly	Big Hole	Trench	3	O	M	Post-MB	p2404, Sol 116
114	2M136480330	Stonefly	Big Hole	Trench	5	O	M	Post-MB	p2404, Sol 116
114	2M136480799	Brassie	Big Hole	Trench	5	O	M	Post-MB	p2404, Sol 116
114	2M136501831	RS2	Big Hole	Trench	3	O	M	Post-MB	p2404, Sol 116
116	2M136662466	Stonefly	Big Hole	Trench	3	O	M	NA	p2404, Sol 116
122	2M137197561	Owens	Cutthroat	Soil	4	O	S	Post-MB	p2565, Sol 122
126	2M137552836	Leadfoot	TruckinFlats	Soil	3	O	M	Post-MB	p2573, Sol 126
135	2M138357379	HorseFlats	Hillyer	Soil	5	O	M	Post-MB	None
140	2M138789298	Williamsburg	The Boroughs	Trench	7	O	M	NA	p2446, Sol 142
140	2M138789734	Mills3	The Boroughs	Trench	7	O	M	Pre-MB	p2446, Sol 142
140	2M138790260	Hell's Kitchen	The Boroughs	Trench	7	O	M	Pre-MB	p2446, Sol 142
141	2M138878267	Mills3	The Boroughs	Trench	5	O	M	Pre-MB	p2446, Sol 142
141	2M138878638	Fordham	The Boroughs	Trench	7	O	S	Pre-MB	p2446, Sol 142
141	2M138879066	Kew Gardens	The Boroughs	Trench	7	O	S	Pre-MB	p2446, Sol 142
141	2M138892235	Hell's Kitchen	The Boroughs	Trench	3	O	M	Pre-MB	p2446, Sol 142
150	2M139687377	IDD Fault	Spirit	IDD Fault	9	C	M	NA	None
151	2M139771015	Joshua	Mojave NP	Rock	3	O	M	Post-MB	p2586, Sol 151
151	2M139771441	Filter Magnet	Spirit	Rover	3	O	M	NA	None
151	2M139771750	Capture Magnet	Spirit	Rover	3	O	M	NA	None
158	2M140400950	Dark4	Shredded	Soil	1	O	M	Post-MB	P2379, Sol 170
158	2M140401311	WhiteStripe	RedStripe	Rock	5	O	M	Post-MB	p2595, Sol 158
160	2M140565777	DantesPeak	EndOfTheRainbow	Rock	8	O	S	Post-MB	p2597, Sol 159
160	2M140566333	IDD Fault	Spirit	IDD Fault	8	O	S	NA	None
161	2M140653320	DantesPeak2	EndOfTheRainbow	Rock	8	O	S	Pre-MB	p2597, Sol 159
162	2M140752100	GoldKlumpen3	EndOfTheRainbow	Rock	7	O	M	Pre-MB	p2597, Sol 159
162	2M140752534	GoldKlumpen5	EndOfTheRainbow	Rock	7	O	M	Pre-MB	p2597, Sol 159
162	2M140752928	IDD Fault	Spirit	IDD Fault	27	O	M	NA	None
163	2M140840681	GoldKlumpen2	EndOfTheRainbow	Rock	7	O	M	Pre-MB	p2597, Sol 159
163	2M140841136	GoldKlumpen4	EndOfTheRainbow	Rock	7	O	M	Pre-MB	p2597, Sol 159
163	2M140841645	GoldKlumpen7	EndOfTheRainbow	Rock	6	O	S	Pre-MB	p2597, Sol 159
163	2M140842057	GoldKlumpen1	EndOfTheRainbow	Rock	7	O	M	Pre-MB	p2597, Sol 159
164	2M140929646	Goldregen1	EndOfTheRainbow	Rock	8	O	S	NA	p2597, Sol 159
164	2M140930263	Goldregen2	EndOfTheRainbow	Rock	8	O	S	NA	p2597, Sol 159
164	2M140930743	Goldfin1	EndOfTheRainbow	Rock, Soil	8	O	S	NA	p2597, Sol 159
166	2M141109887	GoldBar1	FortKnox	Soil	6	O	S	Post-MB	p2545, Sol 180
166	2M141110586	Goldstaub	FortKnox	Soil	8	O	S	NA	p2545, Sol 180
167	2M141188588	Jaws	Goldfinger	Soil	6	O	S	Pre-MB	None
170	2M141460632	Fool's Gold	PotOfGold	Rock	7	O	M	Pre-MB	p2597, Sol 159
171	2M141551134	None	PotOfGold	Rock	10	O	S	NA	p2597, Sol 159
171	2M141552228	None	PotOfGold	Rock	20	O	S	NA	p2597, Sol 159
172	2M141639773	None	PotOfGold	Rock	1	O	M	Pre-MB	p2597, Sol 159
172	2M141640241	None	PotOfGold	Rock	1	O	M	Pre-MB	p2597, Sol 159
175	2M141896115	Wheat4	Breadbox	Rock	5	O	M	Pre-MB	p2530, Sol 166
175	2M141896655	Wheat1_tweaked	Breadbox	Rock	7	O	M	Pre-MB	p2530, Sol 166
175	2M141897363	Wheat2_tweaked	Breadbox	Rock	7	O	M	Pre-MB	p2530, Sol 166
175	2M141898060	Wheat3_tweaked	Breadbox	Rock	7	O	M	Pre-MB	p2530, Sol 166
177	2M142077070	Pearl1_tweaked	String_Of_Pearls	Soil	7	O	M	Pre-MB	p2541, Sol 177
177	2M142077752	Pearl1_S	String_Of_Pearls	Soil	7	O	M	NA	p2541, Sol 177
181	2M142429231	Shortbread1	CookieCutter	Soil	14	O	S	Pre-MB	p2544, Sol 180
191	2M143325094	Jerry	Loofah	Rock	8	O	S	Post-MB	None

Table A1 *(continued)*

Sol	Starting Image_ID	Target	Feature	Target type	No.	CS	S/M	Relation to RAT/MB	Pancam sequence
193	2M143498652	Mammoth4	Wooly Patch	Rock	12	O	S	Pre-MB	p2556, Sol 200
194	2M143587462	Sabre	Wooly Patch	Rock	34	O	S	Pre-Grind, Pre-MB	p2556, Sol 200
196	2M143770387	Sabre	Wooly Patch	Rock	24	O	S	Post-Grind, Pre-MB	p2556, Sol 200
197	2M143858480	Sabre Mastodon	Wooly Patch	Rock	12	O	S	Pre-Grind	p2556, Sol 200
199	2M144039937	Mastodon_real	Wooly Patch	Rock	13	O	S	Post-Grind, Post-MB	p2556, Sol 200
212	2M145185472	Cochiti	Clovis	Rock	6	O	S	Pre-MB	p2563, Sol 217
212	2M145185974	Jemez	Clovis	Rock	6	O	S	Pre-MB	p2563, Sol 217
212	2M145186552	Plano_spot	Clovis	Rock	24	O	S	Pre-Brush	p2563, Sol 217
214	2M145364683	Plano_spot	Clovis	Rock	24	O	S	Post-Brush, Pre-MB	p2569, Sol 226
217	2M145630711	Plano_spot	Clovis	Rock	24	O	S	Post-Grind	p2569, Sol 226
225	2M146348689	Brushed Clovis	Clovis	Rock	6	O	S	Post-Brush	p2569, Sol 226
227	2M146517433	Kilarney Flats	Frio	Soil	8	O	S	NA	p2569, Sol 226
228	2M146608749	Tiny Tim	Ebenezer	Rock	6	O	S	NA	p2571, Sol 227
228	2M146609432	Scrooge	Ebenezer	Rock	6	O	S	NA	p2571, Sol 227
228	2M146610135	Cratchit_2	Ebenezer	Rock	24	O	S	Pre-MB	p2571, Sol 227
229	2M146698436	Marley_tweaked	Ebenezer	Rock	6	O	S	Pre-MB	p2571, Sol 227
229	2M146698969	Fezziwig_tweaked	Ebenezer	Rock	6	O	S	Pre-MB	p2571, Sol 227
230	2M146785410	Cratchit_2 (Ratchit_2)	Ebenezer	Rock	16	O	S	Post-Brush, Post-MB	p2571, Sol 227
232	2M146961183	Cratchit_2 (Ratchit_2)	Ebenezer	Rock	24	O	S	Post-Grind	p2580, Sol 236
235	2M147232906	Fritz	Ebenezer	Rock	1	O	M	Post-MB	p2580, Sol 236
240	2M147676636	GreenEyes	Tikal_Area	Soil	24	O	S	Post-MB	p2597, Sol 263
240	2M147680383	Capture Magnet	Spirit	Rover	3	O	M	NA	None
240	2M147680697	Filter Magnet	Spirit	Rover	3	O	M	Pre-MB	None
258	2M149273525	Filter Magnet	Spirit	Rover	2	O	M	Post-MB	None
258	2M149273739	Capture Magnet	Spirit	Rover	1	O	M	NA	None
258	2M149274486	GreenEyes	Conjunction Junction	Soil	24	O	S	Post-MB	p2597, Sol 263
259	2M149359510	Disturbance	Conjunction Junction	Soil	1	O	M	Post-MB	p2597, Sol 263
270	2M150337317	Best_Dwarf	Temples	Rock	6	O	S	Post-MB	p2537, Sol 271
270	2M150337853	Dwarf_Edge2	Temples	Rock edge	6	O	S	Post-MB	p2537, Sol 271
272	2M150518178	Mi_1	Tetl	Rock	32	O	S	Pre-MB	p2535, Sol 270
273	2M150604770	ThinLayer	Tetl	Rock	32	O	S	NA	p2535, Sol 270
276	2M150874294	Clump	Tetl	Rock	3	O	M	Post-MB	p2598, Sol 264
276	2M150874704	Squeeze	Tetl	Rock	12	O	S	Post-MB	p2535, Sol 270
276	2M150875892	Edge	Tetl	Rock	12	O	S	Post-MB	p2535, Sol 270
279	2M151139145	Coffee	TakeAbreak	Soil	16	O	S	Pre-MB	None
281	2M151316310	Coffee	TakeAbreak	Soil	3	O	M	Post-MB	None
283	2M151494434	Koolik_2	Uchben	Rock	24	O	S	Pre-MB	p2543, Sol 293
286	2M151759502	Koolik_2	Uchben	Rock	24	O	S	Post-Grind, Post-MB	p2543, Sol 293
291	2M152203285	Chiikbes	Uchben	Rock	24	O	S	Post-Brush, Post-MB	p2543, Sol 293
292	2M152294327	Fine	Uchben	Rock	12	O	S	Post-MB	P2415, Sol 278
297	2M152735759	Pickled	Lutefisk	Rock	24	O	S	NA	p2544, Sol 296
298	2M152823813	Flatfish	Lutefisk	Rock	6	O	S	Pre-Brush	p2546, Sol 297
298	2M152824173	Twins	Lutefisk	Rock	6	O	S	Pre-MB	p2546, Sol 297
298	2M152824576	Fish_eyes	Lutefisk	Rock	6	O	S	Pre-MB	p2546, Sol 297
298	2M152825154	RAT_Roe	Lutefisk	Rock	6	O	S	Pre-Brush, Post-MB	p2546, Sol 297
299	2M152912505	RAT_Roe	Lutefisk	Rock	12	O	S	Post-Brush, Post-MB	p2553, Sol 304
299	2M152915790	Ratfish	Lutefisk	Rock	12	O	S	Post-Brush	p2553, Sol 304
307	2M153619500	Capture Magnet	Spirit	Rover	3	O	M	Pre-MB	None
314	2M154240711	Tofurkey	Yams	Soil	16	O	S	Pre-MB	None
327	2M155394860	Tilted_Contact2	Spirit	Rover	12	O	M	NA	None
333	2M155927492	Chisel	Wishstone	Rock	6	O	M	Pre-Brush	p2440, Sol 332
333	2M155930269	Chisel	Wishstone	Rock	24	O	S	Post-Brush	p2565, Sol 334
334	2M156023978	Chisel	Wishstone	Rock	24	O	S	Post-Grind, Pre-MB	p2568, Sol 337
341	2M156637750	Ds1	Penny	Soil	5	O	M	Pre-MB	p2573, Sol 343
348	2M157259088	Dreaming	Wishing Well	Rock	24	O	S	Pre-MB	p2588, Sol 351
350	2M157436854	Tilted_Contact2	Spirit	Rover	12	O	M	NA	None
352	2M157612888	RAT_Target	Champagne	Rock	24	O	S	Pre-Brush, Post-MB	p2597, Sol 360
352	2M157614502	Reachable_Lip	Champagne	Rock	6	O	S	Post-Brush, Pre-MB	p2597, Sol 360
354	2M157792894	RAT_Target	Champagne	Rock	24	O	S	Post-Brush, Post-MB	p2597, Sol 360
358	2M158146856	RAT_Target	Champagne	Rock	24	O	S	Post-Grind, Post-MB	p2597, Sol 360
372	2M159392855	3x1_Tgt_2	Peace	Rock	18	O	S	Post-MB	p2543, Sol 381

Table A1 *(continued)*

Sol	Starting Image_ID	Target	Feature	Target type	No.	CS	S/M	Relation to RAT/MB	Pancam sequence
372	2M159394037	2x2_mosaic	Peace	Rock	24	O	S	Post-MB	p2543, Sol 381
373	2M159478497	Equality	Peace	Rock	5	O	M	Post-MB	p2543, Sol 381
373	2M159478927	Equality_3	Peace	Rock	5	O	M	Post-MB	p2543, Sol 381
373	2M159479393	RAT_Justice	Peace	Rock	20	O	S	Pre-Brush, Post-MB	p2543, Sol 381
374	2M159567193	RAT_Justice	Peace	Rock	3	O	M	Post-Brush, Post-MB	p2543, Sol 381
374	2M159572365	RAT_Justice	Peace	Rock	3	O	M	Post-Grind, Post-MB	p2543, Sol 381
376	2M159744609	RAT_Justice	Peace	Rock	16	O	S	Post-Grind, Post-MB	p2543, Sol 381
380	2M160099732	RAT_Justice	Peace	Rock	29	O	S	Post-Grind, Post-Mb	p2543, Sol 381
380	2M160101370	RAT_Tailings	Peace	Rock	5	O	M	Post-MB	p2543, Sol 381
380	2M160102005	Selma	Peace	Rock	15	O	M	NA	p2543, Sol 381
380	2M160105042	APXS_Target	Peace	Rock	5	O	M	NA	p2543, Sol 381
386	2M160631523	Jambalaya	Alligator	Rock	4	O	S	Post-Brush, Post-MB	p2546, Sol 386
399	2M161789203	Marengo	Pasadena	Soil	5	O	M	Post-MB	p2550, Sol 399
400	2M161877186	Paso Robles	Pasadena	Soil	24	O	S	Post-MB	p2551, Sol 400
415	2M163208054	Joker	Watchtower	Rock	5	O	M	Pre-Brush	p2562, Sol 409
415	2M163210479	Joker	Watchtower	Rock	20	O	S	Post-Brush	p2562, Sol 409
417	2M163384425	Joker	Watchtower	Rock	24	O	S	Post-Grind, Pre-MB	p2574, Sol 419
419	2M163562003	Sky Flat	Sky	Sky	1	C	M	NA	None
426	2M164185530	Big_clod	Paso_Robles2	Rock	7	O	M	NA	p2530, Sol 431
426	2M164186008	Bitty_clod	Paso_Robles2	Rock	7	O	M	NA	p2530, Sol 431
428	2M164353605	Paso_Dark_1	Paso_Robles2	Rock	24	O	S	Post-MB	p2530, Sol 431
428	2M164355316	Paso_Light_1	Paso_Robles2	Rock	24	O	S	Post-MB	p2530, Sol 431
429	2M164448226	Bens_Clod	Paso_Robles2	Rock	7	O	S	Pre-Brush	p2579, Sol 426
429	2M164449658	Bens_Clod	Paso_Robles2	Rock	7	O	S	Post-Brush	p2579, Sol 426
431	2M164620111	Solar array	Spirit	Rover	6	O	M	NA	None
431	2M164621116	Castoro	Paso_Robles2	Soil	5	O	M	NA	None
431	2M164630775	Paso_Dark_1	Paso_Robles2	Soil	4	O	M	Post-MB	p2530, Sol 431
457	2M166937496	Sierra	Crumble	Soil	20	O	S	Pre-MB	p2410, Sol 457
457	2M166939198	Scuff2	Crumble	Soil	20	O	S	Pre-MB	p2410, Sol 457
457	2M166940778	Almonds	Crumble	Soil	20	O	S	Pre-MB	p2410, Sol 457
460	2M167202107	Almonds	Crumble	Soil	12	O	M	Post-MB	p2410, Sol 457
460	2M167203086	Cashew	Crumble	Soil	12	O	M	NA	p2410, Sol 457
469	2M168000971	Keystone	Methuselah	Rock	96	O	S	Pre-Brush, Post-MB	p2561, sol 470
470	2M168092076	Keystone	Methuselah	Rock	48	O	S	Pre-Brush, Post-MB	p2561, sol 470
471	2M168179276	Haunch	Methuselah	Rock	24	O	S	Post-Brush, Post-MB	p2563, sol 471
475	2M168530875	RAT Pitt	Pennsylvania	Rock	48	O	S	Pre-Brush	p2573, sol 476
475	2M168536955	RAT Pitt	Pennsylvania	Rock	16	O	S	Post-Brush	p2573, Sol 476
475	2M168544780	Sky Flat	Sky	Sky	1	O	M	NA	None
475	2M168544844	Sky Flat	Sky	Sky	1	C	M	NA	None
477	2M168708170	Hoof	Jibsheet	soil	8	O	S	NA	p2581, Sol 480
477	2M168708599	Bell	Jibsheet	soil	8	O	S	Pre-MB	p2581, Sol 480
480	2M168974518	Bell	Jibsheet	soil	4	O	S	Post-MB	p2581, sol 480
481	2M169064514	Reef	Jibsheet	Rock	54	O	S	Pre-MB	p2574, Sol 478
484	2M169329632	Davis	Jibsheet	Rock	24	O	S	Pre-Brush, Post-MB	p2595, Sol 484
487	2M169595935	Davis	Jibsheet	Rock	24	O	S	Post-Brush, Post-MB	p2531, Sol 487
491	2M169951172	Paros	Larry's Lookout	Rock	24	O	S	Pre-MB	p2421, sol 489
494	2M170217317	Hitting	Larry's Lookout	Soil	7	O	S	NA	p2538, Sol 494
494	2M170217844	Wallstreet	Larry's Lookout	Soil	14	O	S	NA	p2538, Sol 494
495	2M170307254	Ahab	Pequod	Rock	22	O	S	Pre-Brush	p2550, Sol 503
496	2M170397159	Ahab	Pequod	Rock	24	O	S	Post-Brush	p2550, Sol 503
499	2M170661212	Doubloon	Pequod	Soil	4	O	S	Pre-MB	p2550, Sol 503
499	2M170661687	Moby Dick	Pequod	Rock	20	O	S	Pre-MB	p2549, Sol 503
503	2M171016875	Starbuck	Pequod	Rock	12	O	S	Post-MB	None
503	2M171017732	Nantucket	Pequod	Rock	12	O	S	Post-MB	p2549, Sol 503
505	2M171193987	Solar Panel	Spirit	Rover	6	O	M	NA	None
505	2M171194575	Filter Magnet	Spirit	Rover	1	O	M	NA	None
505	2M171194640	Capture Magnet	Spirit	Rover	1	O	M	NA	None
509	2M171549761	Scuppers	Backstay	Rock	24	O	S	Pre-Brush, Pre-MB	p2559, Sol 509
511	2M171727203	Scuppers	Backstay	Rock	24	O	S	Post-Brush, Post-MB	p2561, Sol 509
512	2M171813652	Scurvy	Backstay	Rock	3	O	M	NA	p2563, Sol 511
529	2M173326086	Franklin	Independence	Rock	24	O	S	Pre-MB	p2532, Sol 523

Table A1 *(continued)*

Sol	Starting Image_ID	Target	Feature	Target type	No.	CS	S/M	Relation to RAT/MB	Pancam sequence
532	2M173590812	Franklin	Independence	Rock	3	O	M	Post-MB	p2532, Sol 532
532	2M173592444	Chase	Independence	Rock	5	O	M	NA	p2532, Sol 532
532	2M173592932	Jefferson	Independence	Rock	8	O	S	NA	None
533	2M173680022	Livingston	Independence	Rock	3	O	M	Pre-Brush, Pre-MB	p2540, Sol 536
533	2M173682845	Livingston	Independence	Rock	32	O	S	Post-Brush, Pre-MB	p2540, Sol 536
538	2M174124601	Penn2	Independence	Rock	24	O	S	Pre-Brush	p2532, Sol 532
539	2M174213184	Penn2	Independence	Rock	24	O	S	Post-Brush	p2532, Sol 532
552	2M175366434	Discourse	Descartes	Rock	24	O	S	Pre-Brush	p2558, Sol 551
553	2M175457907	Discourse	Descartes	Rock	24	O	S	Post-Brush	p2558, Sol 551
556	2M175721388	Petitechou	Descartes	Rock	32	O	S	Post-MB	p2558, Sol 551
556	2M175724069	Moncheri	Descartes	Rock	8	O	S	Post-MB	p2558, Sol 551
557	2M175810309	Gallant	Bourgeoisie	Rock	32	O	S	Post-MB	p2565, Sol 554
557	2M175812594	Gentil	Bourgeoisie	Rock	32	O	S	Post-MB	p2565, Sol 554
557	2M175815253	Chic	Bourgeoisie	Rock	32	O	S	Pre-MB	p2565, Sol 554
560	2M176076484	Gentil Matrice	Bourgeoisie	Rock	32	O	S	Pre-Brush, Pre-MB	p2565, Sol 554
560	2M176081315	Gentil Matrice	Bourgeoisie	Rock	32	O	S	Post-Brush, Pre-MB	p2565, Sol 554
563	2M176344075	Rue Legendre	Haussmann	Rock	24	O	S	Post-MB	p2573, Sol 554
563	2M176345629	Sophie Germain	Haussmann	Rock	24	O	S	Post-MB	p2573, Sol 554
563	2M176347614	Rue Laplace	Haussmann	Rock	24	O	S	Post-MB	p2573, Sol 554
566	2M176609270	Gruyere	Assemblee	Rock	32	O	S	Pre-MB	p2541, Sol 572
571	2M177052969	Gruyere	Assemblee	Rock	6	O	S	Post-MB	p2541, Sol 572
588	2M178562035	Whymper	Lambert	Soil	24	O	S	Post-MB	p2561, Sol 589
588	2M178563557	Hermann Buhl	Lambert	Soil	8	O	S	NA	p2561, Sol 589
588	2M178564406	Couzy	Lambert	Soil	8	O	S	NA	p2561, Sol 589
594	2M179095020	Capture Magnet	Spirit	Rover	1	O	M	Pre-MB	None
597	2M179361095	Capture Magnet	Spirit	Rover	1	O	M	Post-MB	None
597	2M179361223	Filter Magnet	Spirit	Rover	1	O	M	NA	None
600	2M179627937	Shrewsbury_2	Irvine	Rock	24	O	S	Pre-MB	p2577, Sol 603
607	2M180251872	HangTwo	Cliffhanger	Ripple	16	O	S	Pre-MB	p2589, Sol 612
607	2M180252963	Tubular	Cliffhanger	Ripple	16	O	S	Pre-MB	p2589, Sol 612
607	2M180254014	LandsEnd	Cliffhanger	Ripple	16	O	S	Pre-MB	p2589, Sol 612
611	2M180617778	LandsEnd	Cliffhanger	Ripple	1	O	M	Post-MB	p2589, Sol 612
612	2M180692664	HangTwo	Cliffhanger	Ripple	1	O	M	Post-MB	p2589, Sol 612
615	2M180979312	CCT	Spirit	Rover	4	O	M	Post-MB	None
633	2M182556972	Namche Bazaar	Hillary	Rock	36	O	S	Post-MB	p2385, Sol 634
633	2M182562440	Khumjung	Hillary	Rock	36	O	S	Post-MB	p2385, Sol 634
634	2M182645859	Thame	Hillary	Rock	24	O	S	NA	p2385, Sol 634
646	2M183713930	Kestrel	Kansas	Rock	24	O	S	Pre-Brush, Pre-MB	None
646	2M183718124	Kestrel	Kansas	Rock	24	O	S	Post-Brush, Pre-MB	p2579, Sol 649
660	2M184954339	Thrasher	Larry's Bench	Rock	24	O	S	Pre-Brush, Pre-MB	p2535, Sol 664
660	2M184958148	Thrasher	Larry's Bench	Rock	24	O	S	Post-Brush, Pre-MB	p2535, Sol 664
672	2M186019847	Osceola	Seminole	Rock	12	O	S	Pre-brush, Pre-MB	p2551, Sol 678
675	2M186285684	Abiaka	Seminole	Rock	12	O	S	Post-brush, Pre-MB	p2552, Sol 678
683	2M186997776	IDD Stowed	Spirit	Rover	1	C	M	NA	None
687	2M187351752	Iroquet	Algonquin	Rock	20	O	M	Pre-Brush, Post-MB	p2575, sol 690
688	2M187442851	Iroquet	Algonquin	Rock	20	O	M	Post-Brush, Post-MB	p2575, sol 690
698	2M188328271	Horseback	Comanche Spur	Rock	23	O	M	Pre-Brush, Pre-MB	p2533, Sol 704
699	2M188421617	Horseback	Comanche Spur	Rock	19	O	M	Post-Brush, Post-MB	p2533, Sol 704
700	2M188508578	Palomino	Comanche Spur	Rock	22	O	M	Post-Brush, Post-MB	p2533, Sol 704
703	2M188772013	Fins_2	Comanche Spur	Rock	6	O	S	NA	p2533, Sol 704
703	2M188772610	Fins_3	Comanche Spur	Rock	6	O	S	NA	p2533, Sol 704
707	2M189123688	Gallant Knight	El Dorado	Soil	16	O	S	Pre-MB	p2536, Sol 711
707	2M189124700	Shadow	El Dorado	Soil	8	O	S	Pre-MB	p2535, Sol 711
709	2M189317806	Shadow	El Dorado	Soil	3	O	M	Post-MB	p2535, Sol 711
710	2M189392700	Edgar	El Dorado	Soil	8	O	S	NA	p2535, Sol 711
710	2M189393378	Edgar	El Dorado	Soil	3	O	M	NA	p2536, Sol 711
723	2M190547448	Samra	Arad	Soil	6	O	S	Pre-MB	p2542, Sol 723
724	2M190653092	Zoar	Arad	Soil	6	O	S	NA	p2542, Sol 723
724	2M190653630	Hula	Arad	Soil	6	O	S	NA	p2538, Sol 721
736	2M191701669	GongGong_GongZhou	BuzHou	Rock	28	O	S	Pre-MB	p2562, Sol 736
747	2M192678623	Pitcher	Barnhill	Rock	30	O	S	Post-MB	p2276, Sol 751

Table A1 *(continued)*

Sol	Starting Image_ID	Target	Feature	Target type	No.	CS	S/M	Relation to RAT/MB	Pancam sequence
747	2M192681863	Ace	Barnhill	Rock	5	O	S	Pre-MB	p2276, Sol 751
750	2M192955978	Pitcher	Barnhill	Rock	24	O	S	Post-MB	p2276, Sol 751
750	2M192958274	Fastball	Barnhill	Rock	6	O	S	Post-MB	p2267, Sol 751
753	2M193210136	Snout	Posey	Rock	21	O	S	NA	p2583, Sol 753
754	2M193315324	Posey Manager	Posey	Rock	6	O	S	Post-Brush, Post-MB	p2583, Sol 753
761	2M193920758	Monarchs	James Cool Papa Bell	Rock	18	O	S	Post-MB	p2589, Sol 764
761	2M193925245	Stars	James Cool Papa Bell	Rock	6	O	S	Post-Brush, Post-MB	p2589, Sol 764
763	2M194100579	Crawfords	James Cool Papa Bell	Rock	6	O	S	Post-Brush, Post-MB	p2589, Sol 764
770	2M194719265	FuzzySmith	Close Target Rock	Rock	24	O	S	Post-MB	p2595, Sol 772
809	2M198182275	Halley	Enderbyland	Rock	12	O	S	Pre-MB	p2409, Sol 820
812	2M198449160	Mawson	Enderbyland	Soil	30	O	S	Pre-MB	p2409, Sol 820
822	2M199337410	Progress	Enderbyland	Soil	32	O	S	Pre-Brush, Pre-MB	p2409, Sol 820
830	2M200051430	Progress 1	Enderbyland	Soil	24	O	S	Post-Brush, Post-MB	p2540, Sol 831
832	2M200225218	Halley Offset	Enderbyland	Rock	6	O	S	Pre-MB	p2409, Sol 820
842	2M201112998	Test Target	Enderbyland	Soil	20	O	S	NA	p2295, Sol 848
845	2M201382711	Progress	Enderbyland	Soil	21	O	S	Post-Brush, Post-MB	p2545, Sol 856
858	2M202533327	Progress 2	Enderbyland	Soil	20	O	S	Post-Brush, Post-MB	p2546, Sol 858
861	2M202799725	Brunt	Enderbyland	Soil	12	O	S	Pre-MB	p2409, Sol 820
870	2M203598631	Progress 3	Enderbyland	Soil	24	O	S	Post-Brush, Post-MB	p2548, Sol 867
876	2M204131583	Photon transfer	Camera Calibration	Sky	40	C	M	NA	None
880	2M204486381	Brunt	Enderbyland	Soil	3	O	M	Pre-MB	p2412, Sol 973
904	2M206616777	Halley Brunt Offset_1	Enderbyland	Soil	3	O	M	Post-MB	p2412, Sol 973
908	2M206971878	Palmer	Enderbyland	Ripple	16	O	S	NA	p2409, Sol 820
913	2M207415786	Palmer2	Enderbyland	Ripple	16	O	S	NA	p2409, Sol 820
915	2M207593243	Photon transfer	Camera Calibration	Sky	40	C	M	NA	None
921	2M208124099	Photon transfer	Camera Calibration	Sky	40	C	M	NA	None
930	2M208923438	Halley Brunt Offset_2	Enderbyland	Soil	3	O	M	NA	p2412, Sol 973
937	2M209544808	Palmer	Enderbyland	Ripple	3	O	M	NA	p2409, Sol 820
944	2M210166213	Brunt offset 3	Enderbyland	Soil	3	O	M	Post-MB	p2412, Sol 973
955	2M211144704	Capture Magnet	Spirit	Rover	3	O	M	NA	None
956	2M211233322	Filter Magnet	Spirit	Rover	3	O	M	NA	None
963	2M211854776	Filter Magnet	Spirit	Rover	2	O	M	NA	None
963	2M211854983	Capture Magnet	Spirit	Rover	2	O	M	NA	None
1006	2M215672597	Filter Magnet	Spirit	Rover	1	O	M	NA	None
1006	2M215672738	Capture Magnet	Spirit	Rover	1	O	M	NA	None
1006	2M215672885	Solar Panel	Spirit	Rover	6	O	M	NA	None
1007	2M215761168	Clast_1	Enderbyland	Rock	6	O	M	Post-MB	None
1007	2M215761684	Clast_3a	Enderbyland	Rock	24	O	M	Post-MB	None
1007	2M215763339	Clast_2	Enderbyland	Rock	6	O	M	Post-MB	None
1008	2M215849750	Mawson	Enderbyland	Soil	6	O	S	Post-MB	p2409, Sol 820
1008	2M215850098	Palmer	Enderbyland	Ripple	3	O	M	NA	p2409, Sol 820
1008	2M215850400	Clast_3b	Enderbyland	Rock	6	O	S	NA	None
1013	2M216294311	Berkner Island	Enderbyland	Soil	24	O	S	Pre-MB	p2590, Sol 1048
1017	2M216649220	Bear Island	Enderbyland	Soil	21	O	S	Pre-MB	p2588, Sol 1042
1027	2M217537254	King George Island	Enderbyland	Outcrop	24	O	S	Pre-Brush, Pre-MB	p2577, Sol 1024
1031	2M217894128	King George Island	Enderbyland	Outcrop	24	O	S	Post-Brush, Post-MB	p2577, Sol 1024
1034	2 M218159020	Clarence	Enderbyland	Soil	6	O	S	Post-MB	p2590, Sol 1048
1034	2M218159610	Deception	Enderbyland	Soil	6	O	S	Post-MB	p2590, Sol 1048
1035	2M218252949	King George Offset	Enderbyland	Outcrop	3	O	M	Post-Brush, Post-MB	P2577, Sol 1024
1053	2M219844942	Palma	Esperanza	Rock	26	O	S	Post-MB	None
1070	2 M221356003	Montalva	Troll	Outcrop	24	O	S	Post-Brush, Post-MB	p2534, Sol 1073
1080	2M222241654	Montalva Offset	Troll	Outcrop	1	O	M	Post-Brush, Post-MB	p2534, Sol 1073
1080	2M222242932	Riquelme 3	Troll	Outcrop	24	O	S	Post-MB	p2537, Sol 1080
1085	2M222685973	Contact	Troll	Outcrop	20	O	S	Post-MB	p2534, Sol 1073
1085	2M222687653	Londonderry	Troll	Soil	6	O	S	NA	p2534, Sol 1073
1099	2M223928381	Mount Darwin	Tyrone Environs	Soil	24	O	S	Post-MB	p2553, sol 1102
1101	2M224103525	Puenta Arenas	Tyrone Environs	Rock	6	O	S	NA	p2553, sol 1102
1125	2M226238944	Filter Magnet	Spirit	Rover	3	O	M	NA	None
1125	2M226239197	Capture Magnet	Spirit	Rover	3	O	M	NA	None
1128	2M226503507	Filter Magnet	Spirit	Rover	3	O	M	NA	None
1143	2M227835110	Torquas1	Torquas	Rock	24	O	M	Pre-Brush	p2576, sol 1141

Table A1 *(continued)*

Sol	Starting Image_ID	Target	Feature	Target type	No.	CS	S/M	Relation to RAT/MB	Pancam sequence
1143	2M227836455	Torquas2	Torquas	Rock	24	O	M	Post-Brush, Post-MB	p2576, sol 1141
1146	2M228100966	John Carter	Torquas	Rock	8	O	M	Post-MB	p2576, sol 1141
1157	2M229074713	Elizabeth Mahon	Clara Zaph	Rock	24	O	S	Post-MB	p2582, Sol 1160
1168	2M230054540	Belles	Madeline English	Outcrop	32	O	S	Post-MB	p2580, Sol 1156
1171	2M230320933	Peaches	Madeline English	Outcrop	16	O	S	Post-MB	p2580, Sol 1156
1172	2M230409483	Everett	Examine This	Outcrop	6	O	S	Post-MB	p2591, Sol 1177
1176	2M230764360	Slide	Examine This	Outcrop	24	O	S	Pre-Brush, Post-MB	p2596, Sol 1180
1176	2M230767711	Slide	Examine This	Outcrop	24	O	S	Post-Brush, Post-MB	p2596, Sol 1180
1179	2M231027709	Good Question	Examine This	Rock	8	O	S	Post-MB	p2599, Sol 1183
1187	2M231745634	Sky Flat	Sky	Sky	1	C	M	NA	None
1189	2M231920553	Kenosha Comets	Gertrude Weise	Soil	24	O	S	Post-MB	p2539, Sol 1198
1198	2M232718472	Lefty Ganote	Gertrude Weise	Soil	24	O	S	Post-MB	None
1205	2M233342451	Pesapallo	Fin Layer	Rock	24	O	S	Post-Brush, Post-MB	p2544, Sol 1210
1209	2M233695644	Superpesis	Fin Layer	Rock	24	O	S	Post-Brush, Post-MB	p2544, Sol 1210
1211	2M233873380	June Emerson	Fin Layer	Rock	22	O	S	Post-Brush, Post-MB	p2549, Sol 1215
1212	2M233960149	Dorothy Key	Fin Layer	Rock	24	O	S	Post-MB	p2549, Sol 1215
1212	2M233961777	Betty Foss	Fin Layer	Rock	24	O	S	Post-MB	p2549, Sol 1215
1216	2M234317065	Elizabeth Emery	Silica Valley	Rock	24	O	S	Post-Brush, Post-MB	p2561, Sol 1220
1217	2M234405894	Jane Stoll	Silica Valley	Rock	24	O	S	Post-Brush	p2561, Sol 1220
1218	2M234494375	Mildred Deegan	Silica Valley	Rock	24	O	S	Post-Brush	p2561, Sol 1220
1218	2M234496687	Betty Wagoner	Silica Valley	Rock	8	O	S	Post-Brush	p2560, Sol 1220
1219	2M234583089	Betty Wagoner Daughter	Silica Valley	Rock	30	O	S	Post-Brush	p2560, Sol 1220
1225	2M235114786	Nancy Warren	Silica Valley	Rock	24	O	S	Pre-MB	p2378, Sol 1234
1227	2M235292383	Nancy Warren	Silica Valley	Rock	24	O	S	Post-MB	p2378, Sol 1234
1230	2M235561554	Filter Magnet	Spirit	Rover	1	O	M	NA	None
1230	2M235561703	Capture_Magnet	Spirit	Rover	1	O	M	NA	None
1230	2M235561848	Solar Array	Spirit	Rover	4	O	M	NA	None
1230	2M235562408	Calibration Soil	Silica Valley	Soil	6	O	S	Post-MB	None
1232	2M235734206	Darlene Mickelsen	Silica Valley	Rock	24	O	S	NA	p2378, Sol 1234
1235	2M236008312	Eileen Dean	Silica Valley	Rock	7	O	S	Post-MB	None
1239	2M236357772	Filter Magnet	Spirit	Rover	1	O	M	NA	None
1239	2M236357977	Capture_Magnet	Spirit	Rover	1	O	M	NA	None
1239	2M236358181	Solar Array	Spirit	Rover	4	O	M	NA	None
1239	2M236358755	Eileen Dean	Silica Valley	Soil	16	O	S	Post-MB	p2574, Sol 1247
1244	2M236801950	Eileen Dean	Silica Valley	Soil	16	O	S	Post-MB	p2574, Sol 1247
1246	2M236978853	Eileen Dean2	Silica Valley	Soil	16	O	S	Post-MB	p2574, Sol 1247
1251	2M237422763	Innocent Bystander	Silica Valley	Rock	16	O	S	Pre-MB	p2581, Sol 1294
1252	2M237511015	Innocent Bystander	Silica Valley	Rock	6	O	S	Pre-MB	p2581, Sol 1294
1252	2M237511477	Innocent Bystander	Silica Valley	Rock	8	O	S	Pre-MB	p2581, Sol 1294
1253	2M237600056	MTES Shroud Closed	Spirit	Rover	1	O	M	NA	None
1253	2M237600110	MTES Shroud Closed	Spirit	Rover	1	C	M	NA	None
1253	2M237600277	MTES Shroud Open	Spirit	Rover	4	O	M	NA	None
1253	2M237601028	MTES Shroud Open	Spirit	Rover	4	O	M	NA	None
1253	2M237601780	MTES Shroud Open	Spirit	Rover	4	O	M	NA	None
1253	2M237602419	MTES Shroud Closed	Spirit	Rover	1	O	M	NA	None
1257	2M237957582	Bystander Offset2	Silica Valley	Rock	17	O	M	Pre-MB	p2581, Sol 1294
1277	2M239727457	Stealing Second	Silica Valley	Ripple	8	O	S	NA	p2581, Sol 1294
1277	2M239728168	Stealing Third	Silica Valley	Ripple	8	O	S	NA	p2581, Sol 1294
1277	2M239728968	Bystander Offset2	Silica Valley	Rock	1	O	M	Post-MB	p2581, Sol 1294
1280	2M239988487	Sky Flat	Sky	Sky	1	C	M	NA	None
1285	2M240438159	Sky Flat	Sky	Sky	1	C	M	NA	None
1286	2M240527029	Sky Flat	Sky	Sky	1	C	M	NA	None
1287	2M240609863	Sky Flat	Sky	Sky	2	C	M	NA	None
1288	2M240704485	Sky Flat	Sky	Sky	1	C	M	NA	None
1290	2M240884771	Sky Flat	Sky	Sky	4	C	M	NA	None
1290	2M240884928	Sky Flat	Sky	Sky	2	O	M	NA	None
1291	2M240975064	Norma Luker2	Silica Valley	Rock	6	O	S	NA	p2581, Sol 1294
1291	2M240975525	Stealing Third	Silica Valley	Ripple	12	O	S	NA	p2583 Sol 1295
1330	2M244435525	Texas Chili	Home Plate Site 3	Outcrop	30	O	S	Post-Brush	p2597, Sol 1332
1340	2M245323465	Humboldt Peak	Humboldt	Rock	6	O	S	Pre-Brush, Post-MB	p2531, Sol 1346
1355	2M246651970	Capture Magnet	Spirit	Rover	1	O	M	NA	None

Table A1 *(continued)*

Sol	Starting Image_ID	Target	Feature	Target type	No.	CS	S/M	Relation to RAT/MB	Pancam sequence
1358	2M246921251	Filter Magnet	Spirit	Rover	1	O	M	NA	None
1360	2M247099982	Pumpkin Pie	South Promontory	Soil	28	O	S	Post-MB	p2542, Sol 1362
1368	2M247814084	Pecan Pie	Home Plate Site 5	Rock	24	O	S	Post-Brush	p2547, Sol 1371
1409	2M251448107	Chanute	Home Plate Rim	Rock	24	O	S	Pre-Brush	p2433, Sol 1408
1431	2M253402619	Chanute	Home Plate Rim	Rock	24	O	S	Post-Brush, Post-MB	p2564, Sol 1431
1434	2M253668328	Chanute	Home Plate Rim	Rock	4	O	M	Post-Brush, Post-MB	p2564, Sol 1431
1452	2M255266342	Freeman	Home Plate Rim	Rock	24	O	S	Post-Brush, Post-MB	p2585, Sol 1496
1473	2M257129441	Solar Array	Spirit	Rover	4	O	M	NA	None
1473	2M257129925	Filter Magnet	Spirit	Rover	1	O	M	NA	None
1473	2M257130088	Capture Magnet	Spirit	Rover	1	O	M	NA	None
1486	2M258284660	Wendell Pruitt	Winter Haven	Rock	24	O	S	Post-Brush	p2585, Sol 1496
1504	2M259890492	Capture Magnet	Spirit	Rover	1	O	M	NA	None
1506	2M260060940	Solar Panel	Spirit	Rover	1	O	M	NA	None
1510	2M260415195	Arthur C. Harmon	Winter Haven	Soil	3	O	M	Pre-MB	p2585, Sol 1496
1518	2M261125314	Solar Panel	Spirit	Rover	2	O	M	NA	None
1796	2M285804897	Stapledon	Winter Haven	Rock	6	O	S	NA	p2537, Sol 1798
1863	2M291757231	John Wesley Powell	West Valley	Soil	8	O	S	NA	p2555, Sol 1866
1922	2M296987279	Undercarriage	Spirit	Rover	5	O	M	NA	None
1922	2M296987659	Sackrider Tweaked	Troy	Soil	6	O	S	Pre-MB	p2382, Sol 1933
1925	2M297264337	Undercarriage	Spirit	Rover	12	O	M	NA	None
1925	2M297265696	Sackrider Tweaked	Troy	Soil	6	O	S	NA	p2382, Sol 1933
1927	2 M297441797	Olive Tree 1	Troy	Soil	8	O	S	Post-MB	p2382, Sol 1933
1927	2M297442521	Olive Tree 2	Troy	Soil	8	O	S	Post-Brush, Post-MB	p2382, Sol 1933
1927	2M297443445	Olive Branch 1	Troy	Soil	8	O	S	Pre-Brush, Pre-MB	p2382, Sol 1933
1929	2M297616206	Olive Branch 2	Troy	Soil	8	O	S	Post-Brush, Pre-MB	p2382, Sol 1933
1934	2M298057547	Olive Branch 3	Troy	Soil	6	O	S	NA	p2382, Sol 1933
1935	2M298145856	Olive Branch 4	Troy	Soil	6	O	S	NA	p2382, Sol 1933
1936	2M298228753	Penina	Troy	Soil	7	O	S	Pre-MB	p2382, Sol 1933
1940	2M298596988	Penina2	Troy	Soil	6	O	S	NA	p2382, Sol 1933
1941	2 M298683977	Penina3	Troy	Soil	6	O	S	NA	p2382, Sol 1933
1945	2M299034554	Cyclops	Troy	Soil	4	O	S	NA	p2591, Sol 1952
1946	2M299120256	Cyclops Eye2	Troy	Soil	6	O	S	Post-MB	p2591, Sol 1952
1947	2M299208142	Cyclops Eye3	Troy	Soil	5	O	S	Post-MB	p2591, Sol 1952
1963	2M300631971	Cyclops Eye3	Troy	Soil	18	O	S	Post-Brush	p2533, Sol 1967
1966	2M300898198	Cyclops Eye3	Troy	Soil	21	O	S	Post-Grind	p2533, Sol 1967
1967	2M300989193	Olive Branch5	Troy	Soil	28	O	S	NA	p2547, Sol 1982
1968	2M301075861	Olive	Troy	Soil	29	O	S	NA	None
1975	2M301700943	Cyclops Eye5	Troy	Soil	23	O	S	Post-Brush, Post-MB	p2386, Sol 1977
1975	2M301703009	Olive Branch6	Troy	Soil	6	O	S	Post-MB	p2547, Sol 1982
1979	2M302055110	Olive Pit	Troy	Rock	24	O	S	Post-MB	p2546, Sol 1982
1980	2M302140621	Polyphemus Eye	Troy	Soil	6	O	S	Pre-Grind	None
1981	2M302233177	Polyphemus Eye	Troy	Soil	16	O	S	Post-Grind	p2546, Sol 1982
1982	2M302317675	Sackrider	Troy	Soil	32	O	S	NA	p2547, Sol 1982
1986	2M302672518	Penina2	Troy	Soil	12	O	S	Post-Brush, Pre-MB	p2547, Sol 1982
1990	2M303035203	Undercarriage	Spirit	Rover	3	O	M	NA	None
1990	2M303035671	Cyclops Eye6	Troy	Soil	32	O	S	Post-Brush	p2550, Sol 1990
1995	2M303472359	Polyphemus Eye3	Troy	Soil	32	O	S	Post-Grind, Pre-MB	p2553, Sol 1998
1997	2M303649255	Olive Leaf	Troy	Soil	32	O	S	Pre-MB	p2392, Sol 2019
2017	2M305424781	Capture Magnet	Spirit	Rover	1	O	M	NA	None
2024	2M306051245	UnderbellyReconPoint1	Troy	Rock	1	O	M	Post-MB	None
2024	2M306051539	UnderbellyReconPoint2	Troy	Rock	1	O	M	Post-MB	None
2024	2 M306051847	Penina4	Troy	Soil	8	O	S	NA	p2392, Sol 2019
2044	2M307824813	Undercarriage	Spirit	Rover	11	O	M	NA	None
2044	2M307825471	Stratius	Troy	Rock	6	O	S	Pre-MB	p2392, Sol 2019
2052	2M308532099	Thoosa	Troy	Soil	6	O	S	Post-MB	p2546, Sol 1982
2061	2M309332599	Undercarriage	Spirit	Rover	11	O	M	NA	None
2068	2M309949760	Undercarriage	Spirit	Rover	1	C	M	NA	None
2072	2M310306618	Undercarriage	Spirit	Rover	3	O	M	NA	None
2076	2 M310656087	Sky Flat	Sky	Sky	2	O	M	NA	None
2076	2M310656796	Undercarriage	Spirit	Rover	3	O	M	NA	None
2076	2M310662945	Undercarriage	Spirit	Rover	6	O	S	NA	None

Table A1 *(continued)*

Sol	Starting Image_ID	Target	Feature	Target type	No.	CS	S/M	Relation to RAT/MB	Pancam sequence
2081	2M311106183	Undercarriage	Spirit	Rover	3	O	M	NA	None
2088	2M311735152	Undercarriage	Spirit	Rover	3	O	M	NA	None
2090	2M311914075	Undercarriage	Spirit	Rover	3	O	M	NA	None
2092	2M312092807	Undercarriage	Spirit	Rover	3	O	M	NA	None
2095	2M312356262	Undercarriage	Spirit	Rover	3	O	M	NA	None
2099	2M312710915	Undercarriage	Spirit	Rover	3	O	M	NA	None
2104	2M313154622	Undercarriage	Spirit	Rover	3	O	M	NA	None
2109	2M313599180	Undercarriage	Spirit	Rover	3	O	M	NA	None
2113	2M313953857	Undercarriage	Spirit	Rover	7	O	M	NA	None
2117	2M314303813	Undercarriage	Spirit	Rover	8	O	M	NA	None
2118	2M314397410	Undercarriage	Spirit	Rover	5	O	M	NA	None
2120	2M314571352	Undercarriage	Spirit	Rover	5	O	M	NA	None
2122	2M314749944	Undercarriage	Spirit	Rover	5	O	M	NA	None
2130	2M315458293	Undercarriage	Spirit	Rover	5	O	M	NA	None
2132	2M315634819	Undercarriage	Spirit	Rover	5	O	M	NA	None
2138	2M316169425	Undercarriage	Spirit	Rover	5	O	M	NA	None
2140	2M316349630	Undercarriage	Spirit	Rover	5	O	M	NA	None
2145	2M316792369	Undercarriage	Spirit	Rover	1	C	M	NA	None
2147	2M316965460	Undercarriage	Spirit	Rover	8	O	M	NA	None
2151	2M317321466	Undercarriage	Spirit	Rover	3	O	M	NA	None
2174	2M319371677	Undercarriage	Spirit	Rover	5	O	M	NA	None

Acknowledgments

We thank the MER rover planners for their outstanding support of *Spirit* IDD operations. The MIPL MER team's expertise in image processing has greatly aided the MI investigation, specifically, Lisa Ly-Hollins processed Sol 475 Pancam and MI data in support of radiometric calibration. We also appreciate the support received from the MER team at the USGS in Flagstaff: Scott Akins, Jeff Anderson, Brent Archinal, Mark Bailen, Janet Barrett, Kris Becker, Tammy Becker, Debbie Cook, Robin Fergason, Donna Galuszka, Patty Garcia, Trent Hare, Annie Howington-Kraus, Chris Isbell, Co-author Brian Lipkowitz, David MacKinnon, Drew McDaniel, Ryan Raub, Co-author Mark Rosiek, Sheri Showers, Deborah Soltesz, Edwin Tenney, Jim Torson, Sean Varga, Robert Wallace, and Lynn Weller. Boris Semenov of JPL's Navigation and Ancillary Information Facility supported MI geometric processing by providing SPICE kernels in a timely fashion. The radiometrically calibrated MI data products used to support the analysis and conclusions reported above can be found on the Analyst's Notebook: https://an.rsl.wustl.edu/mera/merxbrowser/. This work was performed for the Jet Propulsion Laboratory, California Institute of Technology, sponsored by the National Aeronautics and Space Administration. The use of trade, product, or firm names in this paper does not imply endorsement by the U. S. Government.

References

Alexander, D., Mortensen, H., & Deen, R. (2003). Mars Exploration Rover Project Software Interface Specification (SIS) Camera Experiment Data Record (EDR) and Reduced Data Record (RDR) operations data products, JPL Document D-22846, Jet Propulsion Laboratory, Pasadena, CA.

Alexander, D. A., Deen, R. G., Andres, P. M., Zamani, P., Mortensen, H. B., Chen, A. C., et al. (2006). Processing of Mars Exploration Rover imagery for science and operations planning. *Journal of Geophysical Research*, *111*, E02S02. https://doi.org/10.1029/2005JE002462

Arvidson, R. E., Bell, J. F. III, Bellutta, P., Cabrol, N. A., Catalano, J. G., Cohen, J., et al. (2010). Spirit Mars Rover mission: Overview and selected results from the northern Home Plate Winter Haven to the side of Scamander crater. *Journal of Geophysical Research*, *115*, E00F03. https://doi.org/10.1029/2010JE003633

Arvidson, R. E., Ruff, S. W., Morris, R. V., Ming, D. W., Crumpler, L. S., Yen, A. S., et al. (2008). Spirit Mars Rover mission to the Columbia Hills, Gusev Crater: Mission overview and selected results from the Cumberland ridge to Home Plate. *Journal of Geophysical Research*, *113*, E12S33. https://doi.org/10.1029/2008JE003183

Bell, J. F. III, Joseph, J., Sohl-Dickstein, J. N., Arneson, H. M., Johnson, M. J., Lemmon, M. T., & Savransky, D. (2006). In-flight calibration and performance of the Mars Exploration Rover Panoramic Camera (Pancam) instruments. *Journal of Geophysical Research*, *111*, E02S03. https://doi.org/10.1029/2005JE002444

Bell, J. F. III, Squyres, S. W., Herkenhoff, K. E., Maki, J. N., Arneson, H. M., Brown, D., et al. (2003). The Mars exploration rover Athena Panoramic Camera (Pancam) investigation. *Journal of Geophysical Research*, *108*(E12), 8067. https://doi.org/10.1029/2003JE00207

Bell, J. F., III, Arneson, H., Brown, D., Clark, R., Collins, A., Elliott, T., et al. (2004). Pancam calibration report, JPL Internal Doc. MER 420-6-700 (D-19826), Jet Propulsion Laboratory, Pasadena, CA.

Bertelsen, P., Goetz, W., Madsen, M. B., Kinch, K. M., Hviid, S. F., Knudsen, J. M., et al. (2004). Magnetic properties experiments on the Mars exploration rover Spirit at Gusev crater. *Science*, *305*(5685), 827–829. https://doi.org/10.1126/science.1100112

Cabrol, N. A., Herkenhoff, K., Knoll, A. H., Farmer, J., Arvidson, R., Grin, E., et al. (2014). Sands at Gusev crater, Mars. *Journal of Geophysical Research: Planets*, *119*, 941–967. https://doi.org/10.1002/2013JE004535

Cabrol, N. A., Herkenhoff, K. E., Greeley, R., Grin, E. A., Schöder, C., d'Uston, C., et al. (2008). Soil sedimentology at Gusev crater from Columbia Memorial Station to Winter Haven. *Journal of Geophysical Research*, *113*, E06S05. https://doi.org/10.1029/2007JE002953

Clark, B. C. III, Arvidson, R. E., Gellert, R., Morris, R. V., Ming, D. W., Richter, L., et al. (2007). Evidence for montmorillonite or its compositional equivalent in Columbia Hills, Mars. *Journal of Geophysical Research*, *112*, E06S01. https://doi.org/10.1029/2006JE002756

Cole, S. B. (2015). Petrology, stratigraphy, and geologic history of Husband Hill, Gusev crater, Mars (Doctoral dissertation). Cornell University, Ithaca, New York.

Cole, S. B., Herkenhoff, K. E., Yingst, R. A., & Squyres, S. W. (2014). Similar microtextures in Watchtower and Comanche Class rocks at Gusev crater. Paper presented at 46th Lunar and Planetary Science Conference, the Woodlands, TX, Abstract 1652.

Crisp, J. A., Adler, M., Matijevic, J. R., Squyres, S. W., Arvidson, R. E., & Kass, D. M. (2003). Mars exploration rover mission. *Journal of Geophysical Research*, *108*(E12), 8061. https://doi.org/10.1029/2002JE002038

Crumpler, L. S., Arvidson, R. E., Squyres, S. W., McCoy, T., Yingst, A., Ruff, S., et al. (2011). Field reconnaissance geologic mapping of the Columbia Hills, Mars, based on Mars exploration rover Spirit and MRO HiRISE observations. *Journal of Geophysical Research*, *116*, E00F24. https://doi.org/10.1029/2010JE003749

Danielson, G. E., Kupferman, P. N., Johnson, T. V., & Soderblom, L. A. (1981). Radiometric performance of the Voyager cameras. *Journal of Geophysical Research*, *86*(A10), 8683–8689. https://doi.org/10.1029/JA086iA10p08683

Farrand, W. H., Bell, J. F. III, Johnson, J. R., Arvidson, R. E., Crumpler, L. S., Hurowitz, J. A., & Schröder, C. (2008). Rock spectral classes observed by the Spirit Rover's Pancam on the Gusev crater plains and in the Columbia Hills. *Journal of Geophysical Research*, *113*, E12S38. https://doi.org/10.1029/2008JE003237

Gellert, R., Rieder, R., Brückner, J., Clark, B., Dreibus, G., Klingelhöfer, G., et al. (2006). The Alpha Particle X-Ray Spectrometer (APXS): Results from Gusev crater and calibration report. *Journal of Geophysical Research*, *111*, E02S05. https://doi.org/10.1029/2005JE002555

Golombek, M. P., Grant, J. A., Parker, T. J., Kass, D. M., Crisp, J. A., Squyres, S. W., et al. (2003). Selection of the Mars exploration rover landing sites. *Journal of Geophysical Research*, *108*(E12), 8072. https://doi.org/10.1029/2003JE002074

Gorevan, S. P., Myrick, T., Davis, K., Chau, J. J., Bartlett, P., Mukherjee, S., et al. (2003). Rock Abrasion Tool: Mars Exploration Rover mission. *Journal of Geophysical Research*, *108*(E12), 8068. https://doi.org/10.1029/2003JE002061

Greeley, R., Arvidson, R. E., Barlett, P. W., Blaney, D., Cabrol, N. A., Christensen, P. R., et al. (2006). Gusev crater: Wind-related features and processes observed by the Mars exploration rover Spirit. *Journal of Geophysical Research*, *111*, E02S09. https://doi.org/10.1029/2005JE002491

Greeley, R., Waller, D. A., Cabrol, N. A., Landis, G. A., Lemmon, M. T., Neakrase, L. D. V., et al. (2010). Gusev crater, Mars: Observations of three dust devil seasons. *Journal of Geophysical Research*, *115*, E00F02. https://doi.org/10.1029/2010JE003608

Greeley, R., Whelley, P. L., Neakrase, L. D. V., Arvidson, R. E., Bridges, N. T., Cabrol, N. A., et al. (2008). Columbia Hill, Mars: Aeolian features seen from the ground and orbit. *Journal of Geophysical Research*, *113*, E06S06. https://doi.org/10.1029/2007JE002971

Hamilton, V. E., & Ruff, S. W. (2012). Distribution and characteristics of Adirondack-class basalt as observed by Mini-TES in Gusev crater, Mars and its possible volcanic source. *Icarus*, *218*, 917–949.

Hapke, B. (1993). *Theory of reflectance and emittance spectroscopy*. New York: Cambridge University Press. https://doi.org/10.1017/CBO9780511524998

Herkenhoff, K., Kirk, R., Rosiek, M., Soderblom, L., Sucharski, B., Torson, J., et al. (2004). Mars exploration Rover project Microscopic Imager calibration report, Rev. B, JPL D-19830, MER 420-6-704, Jet Propulsion Laboratory, Pasadena, CA.

Herkenhoff, K. E., Golombek, M. P., Guinness, E. A., Johnson, J. B., Kusack, A., Richter, L., et al. (2008). In-situ observations of the physical properties of the Martian surface. In J. F. Bell, III (Ed.), *The Martian surface: Composition, mineralogy, and physical properties* (pp. 451–467). New York: Cambridge University Press.

Herkenhoff, K. E., Grotzinger, J. P., Knoll, A. H., McLennan, S. M., Weitz, C. M., Yingst, R. A., et al. (2008). Surface processes recorded by rocks and soils on Meridiani Planum, Mars: Microscopic Imager observations during Opportunity's first three extended missions. *Journal of Geophysical Research*, *113*, E12S32. https://doi.org/10.1029/2008JE003100

Herkenhoff, K. E., Squyres, S. W., Anderson, R., Archinal, B. A., Arvidson, R. E., Barrett, J. M., et al. (2006). Overview of the Microscopic Imager investigation during Spirit's first 450 sols in Gusev crater. *Journal of Geophysical Research*, *111*, E02S04. https://doi.org/10.1029/2005JE002574

Herkenhoff, K. E., Squyres, S. W., Arvidson, R., Bass, D. S., Bell, J. F. III, Bertelsen, P., et al. (2004). Textures of the soils and rocks at Gusev crater from Spirit's Microscopic Imager. *Science*, *305*(5685), 824–826. https://doi.org/10.1126/science.3050824

Herkenhoff, K. E., Squyres, S. W., Bell, J. F. III, Maki, J. N., Arneson, H. M., Bertelsen, P., et al. (2003). Athena Microscopic Imager investigation. *Journal of Geophysical Research*, *108*(E12), 8065. https://doi.org/10.1029/2003JE002076

Hurowitz, J. A., McLennan, S. M., Tosca, N. J., Arvidson, R. E., Michalski, J. R., Ming, D. W., et al. (2006). In situ and experimental evidence for acidic weathering of rocks and soils on Mars. *Journal of Geophysical Research*, *111*, E02S19. https://doi.org/10.1029/2005JE002515

Iversen, J. D., & White, B. R. (1982). Saltation threshold on Earth, Mars and Venus. *Sedimentology*, *29*(1), 111–119. https://doi.org/10.1111/j.1365-3091.1982.tb01713.x

Johnson, J. R., Bell, J. F. III, Cloutis, E., Staid, M., Farrand, W. H., McCoy, T., et al. (2007). Mineralogic constraints on sulfur-rich soils from Pancam spectra at Gusev crater, Mars. *Geophysical Research Letters*, *34*, L13202. https://doi.org/10.1029/2007GL029894

Karunatillake, S., McLennan, S., & Herkenhoff, K. E. (2010). Regional and grain size influences on the geochemistry of soil at Gusev crater, Mars. *Journal of Geophysical Research*, *115*, E00F04. https://doi.org/10.1029/2010JE003637

Karunatillake, S., McLennan, S., Herkenhoff, K. E., Husch, J. M., Hardgrove, C., & Skok, J. R. (2014). A Martian case study of segmenting images automatically for granulometry and sedimentology. Part 2: Assessment. *Icarus*, *229*, 408–417. https://doi.org/10.1016/j.icarus.2013.09.021

Kiely, A., & Klimesh, M. (2003). The ICER progressive wavelet image compressor, IPN Progress Report (pp. 42–155). Pasadena, CA: Jet Propulsion Laboratory. Retrieved from http://ipnpr.jpl.nasa.gov/progress_report/42-660 155/155J.pdf

Klingelhöfer, G., Morris, R. V., Bernhardt, B., Rodionov, D., de Souza, P. A. Jr., Squyres, S. W., et al. (2003). The Athena MIMOS II Mössbauer spectrometer investigation. *Journal of Geophysical Research*, *108*(E12), 8069. https://doi.org/10.1029/2003JE002138

Le Bas, M. J. (1981). Carbonatite magmas. *Mineralogical Magazine*, *44*, 133–140.

Lewis, K. W., Aharonson, O., Grotzinger, J. P., Squyres, S. W., Bell, J. F. III, Crumpler, L. S., & Schmidt, M. E. (2008). Structure and stratigraphy of Home Plate from the Spirit Mars Exploration Rover. *Journal of Geophysical Research*, *113*, E12S36. https://doi.org/10.1029/2007JE003025

Madsen, M. B., Goetz, W., Bertelsen, P., Binau, C. S., Folkmann, F., Gunnlaugsson, H. P., et al. (2009). Overview of the magnetic properties experiments on the Mars exploration rovers. *Journal of Geophysical Research*, *114*, E06S90. https://doi.org/10.1029/2008JE003098

Maki, J. N., Bell, J. F. III, Herkenhoff, K. E., Squyres, S. W., Kiely, A., Klimesh, M., et al. (2003). The Mars exploration rover engineering cameras. *Journal of Geophysical Research*, *108*(E12), 5081. https://doi.org/10.1029/2003JE00

McCoy, T. J., Sims, M., Schmidt, M. E., Edwards, L., Tornabene, L. L., Crumpler, L. S., et al. (2008). Structure, stratigraphy, and origin of Husband Hill, Columbia Hills, Gusev crater, Mars. *Journal of Geophysical Research*, *113*, E06S03. https://doi.org/10.1029/2007JE003041

McGlynn, I. O., Fedo, C. M., & McSween, H. Y. Jr. (2011). Origin of basaltic soils at Gusev crater, Mars, by aeolian modification of impact-generated sediment. *Journal of Geophysical Research*, *116*, E00F22. https://doi.org/10.1029/2010JE003712

McSween, H. Y., Ruff, S. W., Morris, R. V., Bell, J. F. III, Herkenhoff, K., Gellert, R., et al. (2006). Alkaline volcanic rocks from the Columbia Hills, Gusev crater, Mars. *Journal of Geophysical Research*, *111*, E09S91. https://doi.org/10.1029/2006JE002698

McSween, H. Y., Ruff, S. W., Morris, R. V., Gellert, R., Klingelhöfer, G., Christensen, P. R., et al. (2008). Mineralogy of volcanic rocks in Gusev crater, Mars: Reconciling Mössbauer, APXS, and Mini-TES spectra. *Journal of Geophysical Research*, *113*, E06S04. https://doi.org/10.1029/2007JE002970

McSween, H. Y., Wyatt, M. B., Gellert, R., Bell, J. F. III, Morris, R. V., Herkenhoff, K. E., et al. (2006). Characterization and petrologic interpretation of olivine-rich basalts at Gusev crater, Mars. *Journal of Geophysical Research*, *111*, E02S10. https://doi.org/10.1029/2005JE002477

Ming, D. W., Gellert, R., Morris, R. V., Arvidson, R. E., Brückner, J., Clark, B. C., et al. (2008). Geochemical properties of rocks and soils in Gusev crater, Mars: Results of the Alpha Particle X-Ray spectrometer from Cumberland Ridge to Home Plate. *Journal of Geophysical Research*, *113*, E12S39. https://doi.org/10.1029/2008JE003195

Ming, D. W., Mittlefehldt, D. W., Morris, R. V., Golden, D. C., Gellert, R., Yen, A., et al. (2006). Geochemical and mineralogical indicators for aqueous processes in the Columbia Hills of Gusev crater, Mars. *Journal of Geophysical Research*, *111*, E02S12. https://doi.org/10.1029/2005JE002560

Morris, R. V., Klingelhöfer, G., Schröder, C., Fleischer, I., Ming, D. W., Yen, A. S., et al. (2008). Iron mineralogy and aqueous alteration from Husband Hill through Home Plate at Gusev crater, Mars: Results from the Mössbauer instrument on the Spirit Mars exploration rover. *Journal of Geophysical Research*, *113*, E12S42. https://doi.org/10.1029/2008JE003201

Morris, R. V., Klingelhöfer, G., Schröder, C., Rodionov, D. S., Yen, A., Ming, D. W., et al. (2006). Mössbauer mineralogy of rock, soil, and dust at Gusev crater, Mars: Spirit's journey through weakly altered olivine basalt on the plains and pervasively altered basalt in the Columbia Hills. *Journal of Geophysical Research*, *111*, E02S13. https://doi.org/10.1029/2005JE002584

Morris, R. V., Ruff, S., Gellert, R., Ming, D. W., Arvidson, R. E., Clark, B. C., et al. (2010). Identification of carbonate-rich outcrops on Mars by the Spirit rover. *Science*, *329*(5990), 421–424. https://doi.org/10.1126/science.1189667

Rice, M. S., Bell, J. F. III, Cloutis, E. A., Wray, J. J., Herkenhoff, K. E., Sullivan, R., et al. (2011). Temporal observations of bright soil exposures at Gusev crater, Mars. *Journal of Geophysical Research*, *116*, E00F14. https://doi.org/10.1029/2010JE003683

Ruff, S., Farmer, J., Calvin, W., Herkenhoff, K., Johnson, J., Morris, R., et al. (2011). Characteristics, distribution, origin, and significance of opaline silica observed by the Spirit rover in Gusev crater, Mars. *Journal of Geophysical Research*, *116*, E00F23. https://doi.org/10.1029/2010JE003767

Ruff, S. W., Christensen, P. R., Blaney, D. L., Farrand, W. H., Johnson, J. R., Michalski, J. R., et al. (2006). The rocks of Gusev crater as viewed by the Mini-TES instrument. *Journal of Geophysical Research*, *111*, E12S18. https://doi.org/10.1029/2006JE002747

Ruff, S. W., & Farmer, J. D. (2016). Silica deposits on Mars with features resembling hot spring biosignatures at El Tatio in Chile. *Nature Communications*, *7*(1). https://doi.org/10.1038/ncomms13554

Ruff, S. W., & Hamilton, V. E. (2017). Wishstone to Watchtower: Amorphous alteration of plagioclase-rich rocks in Gusev crater, Mars. *American Mineralogist*, *102*(2), 235–251. https://doi.org/10.2138/am-2017-5618

Ruff, S. W., Niles, P. B., Alfano, F., & Clarke, A. B. (2014). Evidence for a Noachian-aged ephemeral lake in Gusev crater, Mars. *Geology*, *42*(4), 359–362. https://doi.org/10.1130/G35508.1

Schmidt, M. E., Ruff, S. W., McCoy, T. J., Farrand, W. H., Johnson, J. R., Gellert, R., et al. (2008). Hydrothermal origin of halogens at Home Plate, Gusev crater. *Journal of Geophysical Research*, *113*, E06S12. https://doi.org/10.1029/2007JE003027

Siebach, K., Arvidson, R. E., Cabrol, N., & the Athena Science Team (2010). Recent Spirit results: Microscopic Imager analysis of particle properties in Scamander crater, west of Home Plate. Paper presented at 41st Lunar and Planetary Science Conference, The Woodlands, TX, Abstract 2548.

Soderblom, J. M., Bell, J. F. III, Johnson, J. R., Joseph, J., & Wolff, M. J. (2008). Mars Exploration Rover navigation camera in-flight calibration. *Journal of Geophysical Research*, *113*, E06S19. https://doi.org/10.1029/2007JE003003

Squyres, S. W., Aharonson, O., Clark, B. C., Cohen, B. A., Crumpler, L., de Souza, P. A., et al. (2007). Pyroclastic activity at Home Plate in Gusev crater, Mars. *Science*, *316*(5825), 738–742. https://doi.org/10.1126/science.1139045

Squyres, S. W., Arvidson, R. E., Baumgartner, E. T., Bell, J. F. III, Christensen, P. R., Gorevan, S., et al. (2003). The Mars exploration rover Athena investigation. *Journal of Geophysical Research*, *108*(E12), 8062. https://doi.org/10.1029/2003JE002121

Squyres, S. W., Arvidson, R. E., Bell, J. F. III, Brückner, J., Cabrol, N. A., Calvin, W., et al. (2004). The Spirit rover's Athena science investigations at Gusev crater, Mars. *Science*, *305*, 794.

Squyres, S. W., Arvidson, R. E., Blaney, D. L., Clark, B. C., Crumpler, L., Farrand, W. H., et al. (2006). Rocks of the Columbia Hills. *Journal of Geophysical Research*, *111*, E02S11. https://doi.org/10.1029/2005JE002562

Squyres, S. W., Arvidson, R. E., Ruff, S., Gellert, R., Morris, R. V., Ming, D. W., et al. (2008). Detection of silica-rich deposits on Mars. *Science*, *320*(5879), 1063–1067. https://doi.org/10.1126/science.1155429

Sullivan, R., Arvidson, R., Bell, J. F., Gellert, R., Golombek, M., Greeley, R., et al. (2008). Wind-driven particle mobility on Mars: Insights from MER observations at "El Dorado" and surroundings at Gusev crater. *Journal of Geophysical Research*, *113*, E06S07. https://doi.org/10.1029/2008JE003101

Vaughan, A. F., Johnson, J. R., Herkenhoff, K. E., Sullivan, R., Landis, G. A., Goetz, W., & Madsen, M. B. (2010). Pancam and Microscopic Imager observations of dust on the Spirit rover: Cleaning events, spectral properties, and aggregates. *Mars*, *5*, 129–145. https://doi.org/10.1555/mars.2010.0005

Wang, A., Bell, J. F., Li, R., Johnson, J. R., Farrand, W. H., Cloutis, E. A., et al. (2008). Light-toned salty soils and co-existing Si-rich species discovered by the Mars exploration rover Spirit in Columbia Hills. *Journal of Geophysical Research*, *113*, E12S40. https://doi.org/10.1029/2008JE003126

Yen, A. S., Morris, R. V., Clark, B. C., Gellert, R., Knudson, A. T., Squyres, S., et al. (2008). Hydrothermal processes at Gusev crater: An evaluation of "Paso Robles" class soils. *Journal of Geophysical Research*, *113*, E06S10. https://doi.org/10.1029/2007JE002978

Yingst, R. A., Crumpler, L., Farrand, W. H., Li, R., Cabrol, N. A., & Neakrase, L. D. (2008). Morphology and texture of particles along the Spirit rover traverse from sol 450 to sol 745. *Journal of Geophysical Research*, *113*, E12S41. https://doi.org/10.1029/2008JE003179

Yingst, R. A., Crumpler, L., Farrand, W. H., Li, R., & de Souza, P. (2010). Constraints on the geologic history of "Home Plate" materials provided by clast morphology and texture. *Journal of Geophysical Research*, *115*, E00F13. https://doi.org/10.1029/2010JE003668

Yingst, R. A., Schmidt, M. E., Herkenhoff, K. E., & Mittlefehldt, D. W. (2007). Linking Home Plate and Algonquin class rocks through microtextural analysis: Evidence for hydrovolcanism in the Inner Basin of Columbia Hills, Gusev crater. Paper presented at Seventh International Conference on Mars, Pasadena, CA, LPI Contribution No. 1353, Abstract 3296.